DOCTORAL THESIS

Construction of a Comprehensive Picture of Non-thermal Emissions from Various Types of Supernova Remnants

Author:
Haruo Yasuda

Supervisor:
Shiu-Hang Lee

A thesis submitted in fulfillment of the requirements for the degree of Doctor of Philosophy

in the

Department of Astronomy
Kyoto University

京都大学
KYOTO UNIVERSITY

December 23, 2021

Abstract

Supernova remnants (SNRs) are thought to be one of the major acceleration sites of galactic cosmic rays (CRs) and an important class of objects for high-energy astrophysics. SNRs produce multi-wavelength, non-thermal emission via accelerated particles at collisionless shocks generated by the interactions between the SN ejecta and the circumstellar medium (CSM). Non-thermal emission from SNRs is therefore an effective and promising tool for probing their surrounding CSM and, in turn, the stellar evolution and mass-loss mechanism(s) of massive stars. Although it is expected that the rich diversities observed in supernovae (SNe) and their CSM can result in distinct very high energy (VHE) electromagnetic signals in the SNR phase, there are only a handful of SNRs observed in both GeV and TeV γ-rays so far. A systematic understanding of the links among SN explosion mechanism(s), progenitor stars, and cosmic-ray acceleration is hence limited. In this thesis, we will try to obtain a fuller understanding of non-thermal emissions from SNRs by a self-consistent hydrodynamical simulation coupled with efficient CR acceleration.

First, we explore non-thermal emissions from Type Ia and core-collapse types of SNRs in various circumstellar environments up to 5,000 yr from SN explosion using hydrodynamical simulations coupled with efficient particle acceleration. We find that time evolution of emission characteristics in the VHE regime is mainly dictated by two factors: the number density of the target particles and the amplified magnetic field in the shocked medium. We also predict that the Cherenkov Telescope Array (CTA) will have sufficient sensitivity to detect VHE γ-rays from most young SNRs at distances $\sim$5.0 kpc. Future SNR observations with CTA will thus be promising for probing the CSM environment of SNe and hence their progenitor properties, including the mass-loss history of massive stars.

Next, we calculate the time evolution of broadband non-thermal emission from SNRs originating from Type II SNe embedded in a CSM environment linked to the mass-loss history of the progenitor up to 10,000 yr. Our results predict that Type II SNRs experience a prolonged period of weak radio and γ-ray emission if they run into a spatially extended bubble of low density and high temperature created by the stellar wind during main sequence. For a typical red supergiant progenitor evolved within an average interstellar medium (ISM), this "dark age" corresponds to a range of SNR ages spanning from $\sim$1000 to 5000 yr old. This result suggests that a majority of Type II

SNRs are too faint to be detected, which may help explain why the number of known Galactic SNRs is significantly less than what we expect from the SN rate in our Galaxy.

Finally, we calculate the time evolution of broadband non-thermal emissions from Type Ib/c SNRs whose CSM structures are derived from the mass-loss history of their progenitors up to 10,000 yr. Our results predict that Type Ib/c SNRs make a transition of brightness in radio and γ-ray bands from an undetectable dark for a certain period to a re-brightening phase. This transition originates from their inhomogeneous CSM structures in which the SNRs are embedded within a low-density wind cavity surrounded by a high-density wind shell and the ambient ISM. The "resurrection" in non-thermal luminosity happens at an age of $\sim$1,000 yrs old for a Wolf-Rayet star progenitor evolved within a typical ISM density. Combining with the results of Type II SNR evolution, this result sheds light on a comprehensive understanding of non-thermal emissions from SNRs with different SN progenitor types and ages, which is made possible for the first time by the incorporation of realistic mass-loss histories of the progenitors.

Contents

List of Figures

List of Tables

Chapter 1

Introduction

In this chapter, we will overview some basics regarding supernovae and supernova remnants including their evolution, morphology, particle acceleration and non-thermal emissions near the shock front. At the end, we will mention the motivation and provide a brief outline for the thesis.

1.1 Supernovae

One of most famous and energetic phenomena in the universe is Supernovae (SNe), the explosions of the stars at the final stage of their lives. SNe are historically classified by spectroscopic observations. The SNe with no hydrogen (H) absorption line in their spectra are called Type I supernovae, and those with the absorption line of H are Type II. For more detail, Type I SNe are subdivided in Type Ia with the strong Silicon (Si) absorption line, Type Ib with weak absorption line of Si and the absorption line of Helium (He), and Type Ic without both absorption lines of Si and He. Type II SNe have also subclass of Type IIP having the plateau phase in their light curve, and Type IIL with linearly decreasing light curves.

Type Ia SNe involve the explosion of Carbon-Oxygen (CO) white dwarfs (WDs) and the energy budget is a nuclear fusion of CO into iron-class elements. This explosion happens when the the mass of WDs exceeds the theoretical limit of the WD mass which is the so-called Chandrasekhar mass $\sim 1.4\ M_\odot$, where $M_\odot$ is the solar mass. The two ways are mainly proposed for the WDs to reach the Chandrasekhar mass. One is the single-degenerate (SD) scenario that the WD in a binary system acquires the mass from the companion star. The other is the double-degenerate (DD) scenario that the binary WDs spiral into each other due to an emission of the gravitational wave and finally merge. There is, however, no consensus which mechanism can explain the Type Ia SNe.

On the other hand, Type II/Ib/Ic SNe are collectively called as the core-collapse SNe (CCSNe), which are named after the explosion of massive stars with main-sequence masses $M \leq 8\ M_{\odot}$ and their explosion energy derived from the collapse of the stellar cores by self-gravity. It is known that there is left neutron stars (NS) and/or black holes after the collapse. Above classifications of CCSNe using spectroscopic observations also give us insights about their circumstellar environments and the natures of the progenitors. The detection of H absorption lines from Type II SNe indicates that the progenitors have H-rich envelopes and emit some of them into the surrounding environment in form of stellar wind. The progenitors of Type II SNe are hence supposed to be a red supergiant (RSG). Meanwhile, Type Ib/c SNe do not have absorption lines of H, so H envelopes of their progenitors are striped off for some reasons such as a strong stellar wind and/or a binary interaction. Combining with the detection of He lines from Type Ib SNe and the non-detection for Type Ic SNe, the progenitor of Type Ib SNe is thought to evolve to a He star and that of Type Ic is a CO star. These type of stars are called Wolf-Rayet (WR) stars generally. The classification of SN types are therefore important for the investigation of stellar evolution of massive stars and their unresolved explosion mechanism(s).

1.2 Supernova Remnants

All type of SNe explodes with high energy of $\sim 10^{51}$ erg and the ejecta supersonically expands into their ambient environment. The blast wave is hence formed and sweeps the interstellar medium (ISM) and/or the circumstellar medium (CSM). The swept gases are heated by the shock up to 10^{6-8} K and shine in radio and X-ray. These structures of the stellar ejecta of SNe and the shock-swept hot gases are called the supernova remnants (SNRs).

1.2.1 Evolutionary Phases

The evolution of SNRs have been widely investigated using numerical hydrodynamic simulations. Assuming they evolve within a uniform ISM, 1-dimensional simulations simulations have established the following standard picture of SNR evolution (e.g., Sedov, 1959; Chevalier, 1982b; Chevalier, 1982a; Sturner et al., 1997);

1. Ejecta-dominated phase: In this phase, the forward shock (FS) expands into the ambient media and sweeps up them. The FS creates the contact discontinuity (CD) between the ejecta gas and the swept gas. The dynamics of FS is, however, not affected so much by the swept gas because the swept mass is much less than the ejecta mass. The shock has hence a constant expansion velocity $v_{\rm ej}$ and this phase is called the ejecta-dominated phase or the free-expansion phase. The velocity can be roughly proportional to the root of the explosion energy $E_{\rm SN}$ and the inverse root of the ejecta mass $M_{\rm ej}$, such that $v_{\rm ej} \propto \sqrt{E_{\rm SN}/M_{\rm ej}}$. Considering a typical SNR with $M_{\rm ej} \sim 1.4\ M_\odot$ and $E_{\rm SN} \sim 10^{51}$ erg, it can be easily found that the shock has a high velocity of $\sim 10^4$ km s^{-1} and also a high mach number. The shock radius $R_{\rm sk}$ and velocity $V_{\rm sk}$ becomes $R_{\rm sk}(t) = v_{\rm ej}t$ and $V_{\rm sk}(t) = v_{\rm ej}$. This phase lasts for a few hundred years in a typical ISM density.

2. Sedov phase: When the swept mass becomes comparable to the ejecta mass, the FS is gradually affected by the swept gases and it will be no longer free-expansion. It is known that the shock self-similarly expands in this phase, so this phase is called the self-similar phase. When the adiabatic index of gas is 5/3, the dynamics of FS follows below equations (e.g., Sturner et al., 1997);

$$R_{\rm sk}(t) = 2.5 v_{\rm ej} t_{\rm sed} \left[\left(\frac{t}{t_{\rm sed}} \right)^{0.4} - 0.6 \right] \tag{1.1}$$

$$V_{\rm sk}(t) = v_{\rm ej} \left(\frac{t}{t_{\rm sed}} \right)^{-0.6}, \tag{1.2}$$

where $t_{\rm sed}$ is the transition time from the free-expansion phase to this phase. This timescale is determined by the balance of the swept mass and the ejecta mass, such as $t_{\rm sed} \equiv (M_{\rm ej}/4\pi\rho_0 v_{\rm ej})^{1/3}$ where ρ_0 is a mass density of the ambient gas. This self-similar solution ws firstly studied by Sedov (Sedov, 1959), so this phase is also referred as the Sedov phase. From the kinematic point of view, the shock adiabatically expands conserving the kinetic energy of SN explosion, and this phase is also called as the adiabatic phase or the energy-conservation phase. When enough time has passed and the FS velocity decreases with time, the reverse shock (RS) stands, moves towards the inner ejecta and heats up them. This phase lasts for 10^4 yrs when SNRs evolved within a typical ISM density.

3. Snowplow phase: When the shock has significantly decelerated to $\sim$ 100km s^{-1}, the shocked gas also cools to $\sim$ 10^6 K and the radiative cooling becomes efficiently. This is because this phase is also called radiative phase. The cooling makes the dense and cooled shell at an immediate downstream of the shock, and the interior gases heated by the RS pushes the shell just like a snowplow. The radiative shock evolves as follows;

$$R_{\rm sk}(t) = 2.5 v_{\rm ej} t_{\rm sed} \left[1.29 \left(\frac{t_{\rm rad}}{t_{\rm sed}} \right)^{0.4} \left\{ \left(\frac{t}{t_{\rm rad}} \right)^{0.31} - 0.225 \right\} - 0.6 \right] \quad (1.3)$$

$$V_{\rm sk}(t) = v_{\rm ej} \left(\frac{t_{\rm rad}}{t_{\rm sed}} \right)^{-0.6} \left(\frac{t}{t_{\rm rad}} \right)^{-0.69}, \quad (1.4)$$

where $t_{\rm rad} \equiv 2.7 \times 10^4 (E_{\rm SN}/10^{51}\ {\rm erg})^{0.24} (\rho_0/1.6 \times 10^{-24}\ {\rm g\ cm^{-3}})^{-0.52}$ yr is the transition time to this phase assumed the specific type of cooling rate. In this phase, the energy conservation is no longer kept and the shock is driven by the momentum conservation, which calls this phase the momentum-conservation phase.

4. Extinction phase: Finally, the shock decelerates to a velocity comparable to the turbulent velocity of the surrounding media $\sim$ 10 km s^{-1}. The SNR merges with the ambient medium and spreads heavy elements created by SN explosion into the interstellar space.

This evolutionary has successfully reproduced the dynamical properties of observed SNRs, but does not include many things such as a magnetic field, an inhomogeneity of the ambient environment, a back-reaction of particle acceleration, and so on. These matters affect the SNR evolution and make rich diversities as seen in their morphology.

1.2.2 Morphology

As mentioned above, SNRs have diversities originated from their progenitors, the circumstellar environments which they evolve within. We can see them as the observed morphology and they are classified into four types as follows;

1. Shell-type: This type of SNRs have a ring-like shape due to the projection effect of spherical shell and most of SNRs belong to this type. These have a limb-brightening structure in radio and X-ray bands. Radio

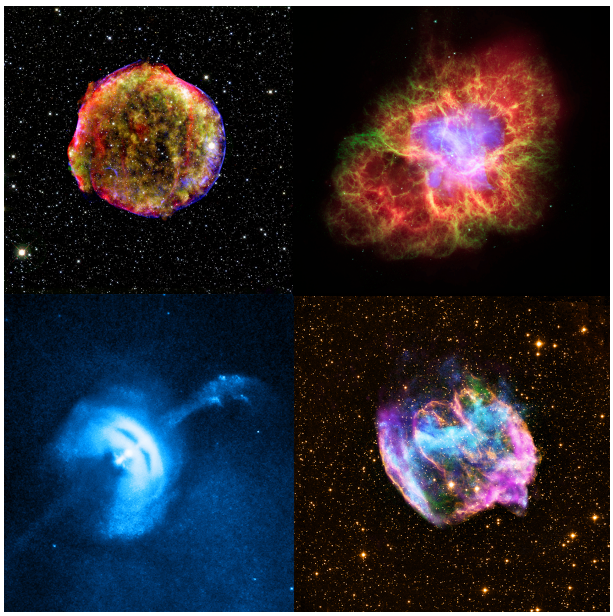

FIGURE 1.1: the composite image in multi-wavelength of various types of SNRs. Upper left: Shell-type SNR, Tycho's image. This image combines X-ray and infrared observations obtained with NASA's Chandra X-ray Observatory (blue, green and yellow) and Spitzer Space Telescope (red), respectively. Credit: X-ray: NASA/CXC/SAO, Infrared: NASA/JPL-Caltech; Optical: MPIA, Calar Alto, O.Krause et al. ; Upper right: Fill-centered type SNR, Crab Nebula's image. The Chandra X-ray image is shown in light blue, the Hubble Space Telescope optical images are in green and dark blue, and the Spitzer Space Telescope's infrared image is in red. Credit: X-ray: NASA/CXC/ASU/J.Hester et al.; Optical: NASA/ESA/ASU/J.Hester & A.Loll; Infrared: NASA/JPL-Caltech/Univ. Minn./R.Gehrz ; Lower left: Composite type SNR, Vela's image. X-ray from NASA's Chandra X-ray Observatory is drown in blue. Credit: NASA/CXC/Univ of Toronto/M.Durant et al ; Lower right: Mixed-Morphology type SNR, W49B's image. The image combines X-rays from NASA's Chandra X-ray Observatory in blue and green, radio data from the NSF's Very Large Array in pink, and infrared data from Caltech's Palomar Observatory in yellow. Credit: X-ray: NASA/CXC/MIT/L.Lopez et al.; Infrared: Palomar; Radio: NSF/NRAO/VLA

emission is produced by the synchrotron radiation by mildly relativistic electrons, and X-ray emission is dominated by thermal or non-thermal component. While thermal X-ray comes from the bremsstrahlung radiation of shock-heated gases and line emissions of heavy elements, the electrons accelerated to relativistic energy emit non-thermal X-ray through the synchrotron radiation. Well-known examples of shell-type

SNRs are Cassiopeia A, Kepler's SNR, Tycho's SNR, SN1006, and RX J1713.7-3946.

2. Fill-centered type: These SNRs have a center-filled morphology in radio and X-ray bands, but a shell structure could not be seen. Compact objects at the center of SNRs like pulsars and pulsar wind nebulae accelerate electrons (and positrons) and emit the synchrotron radiation. Thanks to the presence of the central compact objects (CCOs), the origin of these SNRs are confirmed as core-collapse SNe of massive stars. The examples of these remnants are DA 495, CTB 87, Dragonfly, Crab Nebula, and Geminga.

3. Composite type: This type SNRs have the same center-brightening structure in X-ray band as the fill-centered type, but also have shell-like structure in radio. The emission mechanisms are thought to be the same as the shell-type SNRs in radio and the fill-centered ones in X-ray. The composite type is the second most common type in all SNRs. There are many examples of composite type of SNRs such as Kes 79, γ-Cygni, Boomerang, Spaghetti Nebula, Vela SNR, and RCW89.

4. Mixed-morphology type: Mixed-morphology SNRs have a shell structure in radio by the synchrotron radiation and center-filled structure in X-ray like the composite type, but the X-ray is dominated by thermal X-ray and does not , hence, originate from the CCOs. This type is also called thermal composite type. All of this type of remnants are relatively old remnants and it is often observed that many of this type of SNRs interact with nearby atomic and/or molecular clouds. Recent studies reported recombining plasma have detected from this type SNRs and their generation mechanism is under discussion. The representative examples of mixed-morphology SNRs are W28, W44, W49B, and IC443.

Figure 1.1 shows the composite images of one of most famous SNRs in four types; Tycho's SNR in upper left, Crab Nebula in upper right, Vela in lower left, and W49B in lower right.

1.3 Cosmic Rays and Supernova Remnants

Baade and Zwicky (1934) first suggested that SNe may be the source of cosmic-rays (CRs). The energy density of CRs in the local galaxy is ~ 1 eV cm^{-3} and

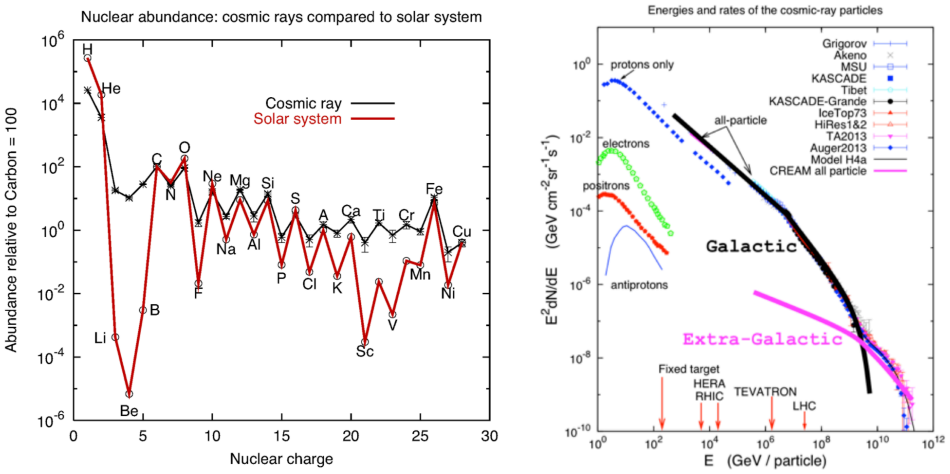

FIGURE 1.2: Left: The CR composition relative to the solar abundance, which are normalized with a carbon. Credit: https://w3.iihe.ac.be/~aguilar/PHYS-467/PA3.html
Right: The CR spectra for various nuclear species measured with ground-base and space experiments. Credit: https://masterclass.icecube.wisc.edu/en/analyses/cosmic-ray-energy-spectrum

hence, the CR injection rate into the galaxy become $\sim 10^{41}$ erg s^{-1} assuming the radius and height of the galaxy are ~ 10 kpc and ~ 100 pc, and the diffusion time of CRs is $\sim 10^6$ yr. On the other hand, the energy input rate from SNe is inferred to be $\sim 10^{42}$ erg s^{-1} assumed that a SN with the explosion energy 10^{51} erg happens in every 30 yrs. It is therefore believed that SNe could accelerate the CRs if 10% of kinetic energy converts into the CR energy in each SN. Indeed, non-thermal emissions produced by accelerated particles have been observed from several SNRs, which is an indirect evidence that SNRs is the in-situ acceleration site of CRs (see also Section 1.4). In this section, we will introduce the observation properties and the acceleration mechanisms of CRs.

1.3.1 Cosmic Rays in a nutshell

CRs are the charged particles accelerated to relativistic energy. The component is proton ($\sim$ 90%), helium ($\sim$ 9%), and others like electrons and heavy elements ($\sim$ 1%). In left panel of Figure 1.2, the CR composition is compared to the solar abundance. This tells us that H and He is relative shorter than the solar, and heavy nuclei is comparable or more abundant than solar abundances. The reasons of these features are still not well understood. The

overabundance of Lithium, Beryllium, Boron is thought to be caused by the spallation of heavier ions such as CO.

Right panel of Figure 1.2 shows the CR spectrum observed with ground-base and space experiments. It can be seen that CRs globally have the power-law spectrum spanning from 10^{10}-10^{20} eV. In detail, the power-law index γ takes three values for some energy ranges; (i) $\gamma = 2.7$ for $E = 10^{10} - 3 \times 10^{15}$ eV, (ii) $\gamma = 3.1$ for $E = 3 \times 10^{15} - 5 \times 10^{18}$ eV, and (iii) $\gamma = 2.7$ for $E = 5 \times 10^{18} - 5 \times 10^{19}$ eV. These transition energy of 3×10^{15} eV and 5×10^{18} eV are often referred as "knee" and "ankle" of CR spectrum. The particles with less than the knee energy is thought to originate from the objects in the galaxy, where the origin of particles with more than the ankle energy is thought to be the extra-galactic objects. These particles are therefore called the galactic cosmic rays (GCRs) and the extra-galactic cosmic rays (EGCRs), respectively. The sources of GCRs is believed to be SNRs but those of EGCRs are still under discussion, for example, active galactic nuclei, gamma-ray bursts, and so on. The spectrum of EGCRs breaks over 5×10^{19} eV. This cut-off has been thought to be affected by the Greisen-Zatsepin-Kuz'min (GZK) effect. The highest-energy protons interact with the photon field of cosmic microwave background (CMB) and lose their energy. The particles, hence, could not travel the intergalactic space so long. In this dissertation, we focus only the GCRs accelerated at SNRs, and will not mention about EGCRs.

1.3.2 Diffusive Shock Acceleration

Now, most widely accepted theory for the CR acceleration is called the diffusive shock acceleration (DSA) theory, which is also referred as the Fermi's 1st order acceleration (e.g., Bell, 1978a; Bell, 1978b; Blandford and Ostriker, 1978; Drury, 1983). The latter name is named after *Enrico Fermi*, who fist proposed that the charged particle gain the energy through the interaction with nearby magnetized materials (Fermi, 1949). Strictly speaking, this original theory is now referred as the Fermi's 2nd order acceleration because the energy gain is proportional to the square of particle velocity. Here, we introduce in order two acceleration mechanisms which are proposed by Bell (1978a) and Bell (1978b) and Blandford and Ostriker (1978) independently, but lead to the same results.

The basic concept of DSA is that the charged particles gain the kinetic energy when they happened to cross the shock front from upstream to downstream and return to upstream. If they experience this process repeatedly,

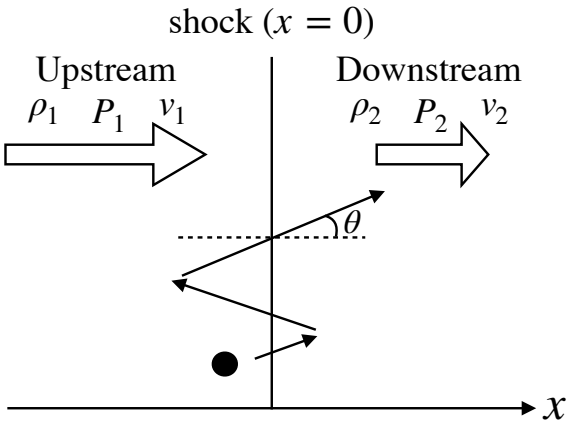

FIGURE 1.3: The schematic picture of 1-D geometry for the particle acceleration. In shock-rest frame, the plane parallel shock locates at $x = 0$ and the gas flows with a velocity v_1 from far upstream $x = -\infty$ and escapes to far downstream $x = +\infty$ with a velocity v_2. This figure also shows the image that the particles cross the shock front with an angle θ.

they will become to have the substantial energy. This statistical acceleration mechanism is firstly formulated by Bell (1978a) and Bell (1978b). Before introducing Bell's method, we briefly introduce the Rankin-Hugoniot relation at first, which is related to the background plasma and hydrodynamically links between the upstream and downstream of the shock.

Generally, the conservation laws of mass, momentum, and energy should be conserved even at back and forward of the shock. Considering the size of accelerated particles, the curvature of shock can be ignored and we can regard the shock as the plane-parallel shock. Because the dynamical time scale of the shock is much larger than the time scale of shock heating, we can also ignore the time variation of hydrodynamics. For simplicity, we consider a 1-D geometry and shock-rest frame as shown in Figure 1.3, but the magnetic field is not taken into account. All quantities in the upstream (downstream) are labeled with the subscript 1 (2). In these situations, the Euler equations can be re-written as below;

$$\rho_1 v_1 = \rho_2 v_2, \tag{1.5}$$

$$\rho_1 v_1^2 + P_1 = \rho_2 v_2^2 + P_2, \tag{1.6}$$

$$\left(\frac{1}{2}\rho_1 v_1^2 + \frac{\gamma}{\gamma - 1} P_1\right) v_1 = \left(\frac{1}{2}\rho_2 v_2^2 + \frac{\gamma}{\gamma - 1} P_2\right) v_2, \tag{1.7}$$

where γ is the specific heat ratio. By defining and substituting the compression ratio over the shock, $R \equiv \rho_2/\rho_1 = v_1/v_2$, and the Mach number of upstream $M_{s,1} = \sqrt{\rho_1 v_1^2/\gamma P_1}$ into above equations, we can obtain a equation,

$$\left\{(\gamma-1)M_{s,1}^2+2\right\}R^2 - 2(\gamma M_{s,1}^2+1)R + (\gamma+1)M_{s,1}^2 = 0. \tag{1.8}$$

There are two solutions of this equation. One trivial solution is $R = 1$, which corresponds to the situation the shock does not exist. The another, non-trivial solution is

$$R = \frac{(\gamma+1)M_{s,1}^2}{(\gamma-1)M_{s,1}^2+2}. \tag{1.9}$$

If we take the limit of strong shock $M_{s,1} \to \infty$, the compression ratio becomes $R \to (\gamma+1)/(\gamma-1) = 4$ in the case of monoatomic and non-relativistic gas $\gamma = 5/3$.

Under these conditions, the energy gain for a particle with the kinetic energy E and momentum p by crossing the shock is given as follows;

$$E' = \Gamma E(1 + \frac{\Delta v}{c}\cos\theta), \tag{1.10}$$

where Γ is the Lorentz factor of shock velocity, θ is the shock crossing angle to shock normal (see, Figure 1.3), and c is the light velocity. Since the SNR shock is non-relativistic shock, $\Gamma \sim 1$, when the particle cross the shock from the upstream to downstream, the velocity difference of plasma become $\Delta v = v_2 - v_1 < 1$ and the particle lose its energy. On the other hand, when returning from the downstream to the upstream, $\Delta v = v_1 - v_2 > 1$ and it gains the energy. So, the angle-averaged energy gain and loss becomes

$$\left\langle \frac{E'-E}{E} \right\rangle_{\text{gain}} = \frac{\int_0^{\pi/2}(\Delta v\cos\theta/c)2\pi\cos\theta\sin\theta d\theta}{\int_0^{\pi/2}2\pi\cos\theta\sin\theta d\theta} = \frac{2}{3}\frac{\Delta v}{c} = \frac{2}{3}\frac{v_1-v_2}{c}, \tag{1.11}$$

and $\langle E'-E/E\rangle_{\text{loss}} = 2\Delta v/3c = -2(v_2-v_1)/3c$. Therefore, the net energy gain through the process becomes

$$\left\langle \frac{\Delta E}{E} \right\rangle_{\text{net}} = \left\langle \frac{\Delta E}{E} \right\rangle_{\text{gain}} - \left\langle \frac{\Delta E}{E} \right\rangle_{\text{loss}} = \frac{4}{3}\frac{v_1-v_2}{c} = \frac{4}{3}\frac{v_1}{c}\left(1-\frac{1}{R}\right). \tag{1.12}$$

Assuming that the particle with initial energy E_0 experience this process by M times, its energy will increase to

$$E_M = E_0 \left\{ 1 + \frac{4}{3}\frac{v_1}{c}\left(1 - \frac{1}{R}\right) \right\}^M . \tag{1.13}$$

Next, we consider the probability of a particle to escape from this process. Because the particles co-move with the flow, some of them are advected to downstream and never return to upstream. The escape probability is determined by the ratio between the flux of the particle advected to the downstream, $F_{\rm adv}$, and that of the particle returning from the downstream to the upstream, $F_{\rm ret}$,

$$P_{\rm esc} = \frac{F_{\rm adv}}{F_{\rm ret}} = \frac{n(p)v_2}{n(p)c/4} = \frac{4v_1}{cR}, \tag{1.14}$$

where $n(p)$ is the differential number density of the particles with momentum p. The probability of a particle to complete M cycle is, hence,

$$P(\geq M) \sim (1 - P_{\rm esc})^M = \left(1 - \frac{4v_1}{cR}\right)^M . \tag{1.15}$$

Finally, combining two results of equation (1.13) and (1.15), we can obtain the differential energy distribution $n(E)$ as follows;

$$n(E) \propto \frac{dP(\geq M)}{dE} \propto \frac{-3}{(R-1)E_0}\left(\frac{E}{E_0}\right)^{-(R+2)/(R-1)} . \tag{1.16}$$

This formalism can naturally reproduce the power-law distribution and under the strong shock limit, the power-law index becomes -2.

Blandford and Ostriker (1978) formulated this acceleration mechanism with the another approach, which solves a diffusion-convection equation in one-dimensional and shock-rest frame as below;

$$\frac{p}{3}\frac{du(x)}{dx}\frac{\partial f(x,p)}{\partial p} = \frac{\partial}{\partial x}\left\{ u(x)f(x,p) - \kappa(x,p)\frac{\partial f(x,p)}{\partial x} \right\}, \tag{1.17}$$

where $f(x,p)$ is the phase-space distribution function of CR assumed to be stationary and isotropic in momentum space, $\kappa(x,p)$ is the diffusion coefficient, and $u(x)$ is the flow velocity at position x. We consider to integrate this equation from $x = -\infty$ to $x = \infty$. Under the conditions of $f(x < 0, p) = f_1(p)$, $f(x \geq 0, p) = f_2(p)$, $u(x < 0) = u_1$, and $u(x \geq 0) = u_2$ (see also

Figure 1.3), we can get the differential equation about $f_2(p)$,

$$p\frac{df_2(p)}{dp} = -\alpha f_2(p) + \alpha f_1(p), \tag{1.18}$$

where $\alpha = 3R/(R-1)$ and $du(x)/dx = -(u_1 - u_2)\delta(x)$ are used. The analytical solution of this equation is

$$f_2(p) = \alpha p^{-\alpha} \int^p q^{\alpha-1} f_1(q) dq + C p^{-\alpha}, \tag{1.19}$$

where C is the integration constant. To avoid the divergence toward $p \to 0$, we set $C = 0$. When the particles with a mono-energetic momentum are assumed to be injected from the upstream, in that $f_1(p) \propto \delta(p - p_{\rm inj})$, we can again get the power-law distribution $f_2(p) \propto p^{-\alpha}$ and this can be re-written in energy space,

$$n_2(E) = 4\pi p^2 f_2(p) \frac{dp}{dE} \propto E^{-\alpha+2} = E^{-(R+2)/(R-1)}. \tag{1.20}$$

This is the same result as Equation (1.16). This approach can be applied more broadly because we can choose $f_1(p)$ arbitrarily. One is most interesting cases is when $f_1(p)$ has the power-law form, $f_1(p) \propto p^{-\beta} (\beta \neq \alpha)$. One can easily find $f_2(p)$ also become the power-law form with the same index, $f_2(p) \propto p^{-\beta}$. These two cases corresponds to the "injection" and "re-acceleration" cases, respectively, as mentioned in next subsection in detail. We note that these formalisms impose several assumptions. For example, the gas flow velocity and CR distribution function takes the same values in the upstream and the downstream, respectively. These treatment is called a test-particle (TP) approximation and is valid only when the accelerated particles do not affect the background plasma. Once high-energy particles are produced through above processes, the pressure of accelerated particles have a substantial fraction against that of gas fluid, and the hydrodynamical structure needs to be modified. This modification includes non-linear processes and the DSA theory including these modifications is called the non-linear DSA (NLDSA) theory.

1.3.3 Non-Linear Diffusive Shock Acceleration

Here, we introduce the formalism of NLDSA following a series of previous works (Blasi, 2004; Caprioli et al., 2009; Caprioli, Amato, and Blasi, 2010). We again consider to solve the one-dimensional diffusion-convection equation

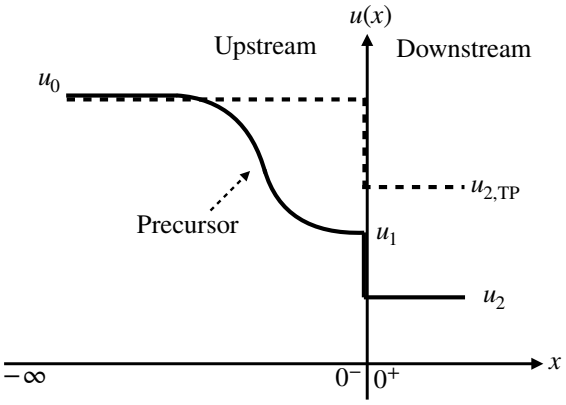

FIGURE 1.4: The schematic picture of 1-D geometry for NLDSA. Solid line shows the gas flow velocity depending on the spatial coordinate x in shock-rest frame. u_0, u_1 and u_2 are the flow velocity at far upstream ($x = -\infty$), immediately upstream of shock ($x = 0^-$), and immediately downstream of shock ($x = 0^+$), respectively. Dashed line shows the gas flow velocity in shock-rest frame and TP case, with the velocity of upstream u_0 and the one of downstream $u_{2,\mathrm{TP}}$.

assumed to be isotropic in momentum space and stationary,

$$u(x)\frac{\partial f(x,p)}{\partial x} = \frac{\partial}{\partial x}\left[D(x,p)\frac{\partial f(x,p)}{\partial x}\right] + \frac{p}{3}\frac{du(x)}{dx}\frac{\partial f(x,p)}{\partial p} + Q(x,p), \quad (1.21)$$

where $D(x,p)$ is the spatial diffusion coefficient at any position x and momentum p, and $Q(x,p)$ is the injection rate of particles with the momentum p from the position x. Hereafter, we label the various quantities in far upstream ($x = -\infty$), immediately upstream ($x = 0^-$), and immediately downstream ($x = 0^+$) with the subscript 0, 1, and 2 (see Figure 1.4).

First, we integrate equation (1.21) in all of upstream region from $x = -\infty$ to $x = 0^-$, assuming the injection starts from the immediately upstream of the shock, $Q(x,p) = Q_{\mathrm{inj}}(p)\delta(x)$,

$$\begin{aligned}&\left[D(x,p)\frac{\partial f(x,p)}{\partial x}\right]_1 - \left[D(x,p)\frac{\partial f(x,p)}{\partial x}\right]_0 + \int_{-\infty}^{0^-}\frac{p}{3}\frac{du(x)}{dx}\frac{\partial f(x,p)}{\partial p}dx \\ = \;& u_1 f_{\mathrm{sk}}(p) - u_0 f_\infty(p) - \int_{-\infty}^{0^-}\frac{du(x)}{dx}f(x,p)dx, \end{aligned} \quad (1.22)$$

where $f_\infty(p) \equiv f(x = -\infty, p)$ and $f_{\mathrm{sk}}(p) \equiv f(x = 0, p)$ are the CR distribution function at far upstream and at shock, respectively. When it is assumed that the spatial dependence of the distribution function can be ignored at far upstream, we can set the second term of left-hand side in the above equation

is zero.

Next, we also integrate equation (1.21) at the shock from $x = 0^+$ to $x = 0^-$ to take the particle injection into account and we can obtain the following equation,

$$\left[D(x,p)\frac{\partial f(x,p)}{\partial x}\right]_2 - \left[D(x,p)\frac{\partial f(x,p)}{\partial x}\right]_1 + \frac{p}{3}(u_2 - u_1)\frac{df_{\rm sk}(p)}{dp} = -Q_{\rm inj}(p). \tag{1.23}$$

We also assume that we can ignore the spatial dependence of CR distribution function in downstream, we can set the first term of left-hand side in the above equation is zero. Combining equations (1.22) and (1.23) with these assumptions, we can obtain

$$\begin{aligned} &\int_{-\infty}^{0^-}\frac{du(x)}{dx}f(x,p)dx + \int_{-\infty}^{0^-}\frac{p}{3}\frac{du(x)}{dx}\frac{\partial f(x,p)}{\partial p}dx \\ =\ &\frac{p}{3}(u_1 - u_2)\frac{df_{\rm sk}(p)}{dp} + u_1 f_{\rm sk}(p) - u_0 f_\infty(p) - Q_{\rm inj}(p). \end{aligned} \tag{1.24}$$

Here, we define a new quantity as

$$u_p(p) \equiv u_1 - \frac{1}{f_{\rm sk}(p)}\int_{-\infty}^{0^-}\frac{du(x)}{dx}f(x,p)dx. \tag{1.25}$$

the accelerated particles produce the back-pressure against background plasma as mentioned above, and modify the hydrodynamical structure in upstream, which is known as a precursor. The flow velocity which the particle feel, hence, differs from the gas velocity u_0, and this quantity can be interpreted as the "effective" fluid velocity that the particles with momentum p experience in the upstream. By using this quantity, the equation (1.24) can be re-written as below,

$$p\frac{df_{\rm sk}(p)}{dp} = -\frac{3}{u_p(p) - u_2}\left[\left\{u_p(p) + \frac{p}{3}\frac{du_p(p)}{dp}\right\}f_{\rm sk}(p) - u_0 f_\infty(p) - Q_{\rm inj}(p)\right]. \tag{1.26}$$

The solution of this equation can be written in the implicit form as below,

$$\begin{aligned} f_{\rm sk}(p) \ =\ &\int_0^p \frac{dp_1}{p_1}\frac{3}{u_p(p_1) - u_2}\{Q_{\rm inj}(p_1) + u_0 f_\infty(p_1)\} \\ &\times \exp\left[-\int_{p_1}^p \frac{dp_2}{p_2}\frac{3}{u_p(p_2) - u_2}\left\{u_p(p_2) + \frac{p_2}{3}\frac{du_p(p_2)}{dp_2}\right\}\right] \end{aligned} \tag{1.27}$$

We can interpret this solution as the sum of two terms; (i) the injection term that describes how many the (supra-)thermal particles with the injection rate

$Q_{\rm inj}(p)$ convert to the high-energy particles through the DSA process, and (ii) the re-acceleration terms that any pre-existing particles $f_\infty(p)$ such as the galactic CRs is also re-accelerated through the same process.

As the injection model, we adopt so-called "thermal-leakage" model proposed by Blasi (2004) and Blasi, Gabici, and Vannoni (2005), which assumes that some fraction of the supra-thermal particles start to accelerate. When the particles with the injection momentum $p_{\rm inj}$ are mono-chromatically injected in this model, the injection rate can be written as below,

$$Q_{\rm inj} = \eta \frac{n_1 u_1}{4\pi p_{\rm inj}^2} \delta(p - p_{\rm inj}), \tag{1.28}$$

where η is the ratio of accelerating particles and thermal particles. We, here, define two quantities; (i) the compression ratio between far upstream and downstream, $R_{\rm tot} \equiv u_0/u_2$, and (ii) the one at sub-shock, $R_{\rm sub} \equiv u_1/u_2$. These compression ratio takes the same value $R_{\rm sub} = R_{\rm tot} = R_{\rm tot,TP}$ in the TP case because there is no spatial dependence on the fluid velocity in the TP case, i.e. $u_0 = u_1$ (see Figure 1.4). Substituting equation (1.28) and these values in equation (1.27), we can get the general form of equation (1.27) as below,

$$\begin{aligned} f_{\rm sk}(p) &= \frac{3R_{\rm sub}}{R_{\rm tot}U(p) - 1} \frac{\eta n_1}{4\pi p_{\rm inj}^3} \exp\left[- \int_{p_{\rm inj}}^{p} \frac{dp_1}{p_1} \frac{3R_{\rm tot}U(p_1)}{R_{\rm tot}U(p_1) - 1} \right] \\ &\quad + \frac{3R_{\rm tot}}{R_{\rm tot}U(p) - 1} \int^{p} \frac{dp_2}{p_2} f_\infty(p_2) \exp\left[- \int_{p_2}^{p} \frac{dp_3}{p_3} \frac{3R_{\rm tot}U(p_3)}{R_{\rm tot}U(p_3) - 1} \right], \end{aligned} \tag{1.29}$$

where $U(p) = u_p(p)/u_0$ is the dimensionless velocity. Finally, we can obtain the overall CR distribution function as below (e.g., Malkov+2000),

$$f(x,p) = f_{\rm sk}(p) \exp\left[- \frac{q(p)}{3D(x,p)} \int_x^0 dx' u(x') \right], \tag{1.30}$$

where $q(p) = -d\ln f_{\rm sk}(p)/d\ln p$ is the slope of the distribution function.

1.3.4 Magnetic Field Amplification

The back-reaction of CR acceleration affects not only the hydrodynamics but also the magnetic field. The instability induced by the streaming of CRs could generate the magnetic field and this phenomenon is called the magnetic field amplification (MFA). This streaming instability results from two types of the particle-wave interaction; (i) the resonant type that the CR stream resonantly

excites the Alfvén wave whose wavelength matches with the gyro-radius of accelerated particles (Bell, 1978a), and (ii) the non-resonant type that the wavelength of generated Alfvén wave is not resonant to the gyro-radius of CRs (Bell, 2004). Amato and Blasi (2009) showed that in the context of SNRs, the non-resonant type is dominant in their early phase and the resonant type become prominent in later phase because of the difference of the velocity dependence. We, therefore, briefly introduce the MFA through the resonant type of streaming instability.

The stationary transport equation for the growth of magnetic field turbulence can be written as below,

$$\frac{\partial F_w(x,k)}{\partial x} = u(x)\frac{\partial P_w(x,k)}{\partial x} + \{\sigma(x,k) - \Gamma(x,k)\}P_w(x,k), \tag{1.31}$$

where $F_w(s,k)$ is the magnetic energy flux of the waves with wavenumber k, $P_w(x,k)$ is the magnetic pressure of the waves, and $\sigma(x,k)$ and $\Gamma(x,k)$ are the growing rate and damping rate of magnetic energy respectively. Because we now consider the resonant type of instability, the growth rate is determined by the resonant scattering between the accelerated CRs and the self-generated turbulence, and is expressed as followed,

$$\sigma(x,k) = \frac{4\pi}{3}\frac{v_A(x)}{P_w(x,k)}\left[p^4 v(p)\frac{\partial f(x,p)}{\partial x}\right]_{p=\bar{p}(k)}, \tag{1.32}$$

where $v_A(x) = B/\sqrt{4\pi\rho(x)}$ is the Alfvén speed, $v(p)$ is the velocity of the particle with momentum p, and $\bar{p}(k) = eB/km_{\rm p}c$ is the resonant momentum. Assuming the damping rate is negligibly small compared to the growth rate, we integrate this equation in k-space and can obtain the following equation,

$$\frac{dF_w(x)}{dx} = u(x)\frac{dP_W(x)}{dx} + v_A(x)\frac{dP_{\rm CR}(x)}{dx}, \tag{1.33}$$

where $P_{\rm CR} = (4\pi/3)\int p^3 v(p) f(x,p) dp$ is the CR pressure. We furthermore assume $u(x) \gg v_A(x)$, so that $F_w(x) \approx 3u(x)P_w(x)$. Substituting this in above equation, we get

$$2u(x)\frac{dP_W(x)}{dx} = -3P_w(x)\frac{du(x)}{dx} + v_A(x)\frac{dP_{\rm CR}(x)}{dx}. \tag{1.34}$$

The momentum conservation in the upstream region is

$$\rho_0 u_0^2 + P_0 + P_{\rm CR,0} + \frac{B_0^2}{8\pi} = \rho_0 u_0 u(x) + P(x) + P_{\rm CR}(x) + \frac{B(x)^2}{8\pi}, \tag{1.35}$$

but when the gas pressure and the magnetic pressure is much smaller than the kinetic term and the CR pressure, we approximate the above equation, $P_{\rm CR}(x) \approx \rho_0 u_0^2 - \rho_0 u_0 u(x)$. The solution of equation (1.34), hence, is

$$P_w(x) = \frac{\rho_0 u_0^2}{4M_{A,0}} \frac{1 - U(x)^2}{U(x)^{3/2}}, \tag{1.36}$$

where $U(x) = u(x)/u_0$ is the normalized velocity and $M_{A,0} = v_{A,0}/u_0$ is the Alfvén Mach number in far upstream. In case that the damping rate could not be neglected and is proportional to the growth rate, $\Gamma(x,k) = f_{\rm damp}\sigma(x,k)$, the solution needs to multiply by the factor of $1 - f_{\rm damp}$ to P_w. Finally, we can obtain the amplified magnetic field as follows,

$$B(x) = \sqrt{B_0^2 + 8\pi(1 - f_{\rm damp})P_w} = \sqrt{B_0^2 + \frac{8\pi(1 - f_{\rm damp})\rho_0 u_0^2}{4M_{A,0}} \frac{1 - U(x)^2}{U(x)^{3/2}}}. \tag{1.37}$$

Indeed, the estimated magnetic field at the downstream of shock is an order of 100μG whereas the averaged one in the galactic plane is $\sim \mu$G. It is, hence, important for us to take the effect of MFA into account, but there is under discussion what mechanism(s) work for MFA.

1.4 Non-thermal Emissions from SNRs

SNRs are generally bright in multiwavelength and the emissions are divided into thermal and non-thermal emission. The ions and electrons which constitute SNRs are thermalized up to $\sim 10^{6-8}$ K by the FS or RS as mentioned in section 1.2, and emit X-ray continuum through bremsstrahlung. This process is often called the thermal bremsstrahlung. On the other hand, the particles accelerated at SNR shock interact with their surrounding media and produce non-thermal emission, which is named after the power-law distribution of CRs (not Maxwellian). The emission mechanisms of non-thermal emission include γ-ray radiation by π^0 decay through the proton-proton interaction (π^0 decay), synchrotron radiation, Inverse Compton scattering (IC), and non-thermal bremsstrahlung. The first one is labeled as 'hadronic' and the latters are categorized in 'leptonic' because these emissions are originated from hadron (proton, helium, and heavy ions) and lepton (electron and positron), respectively.

Non-thermal emissions has been observed from many SNRs. Koyama et al. (1995) first detected non-thermal X-ray from the young SNR, SN1006 with

X-ray detector *ASCA*. This has been thought to be the production of CR electrons accelerated to ~ 100 TeV through synchrotron radiation, and is the first and indirect evidence of electron acceleration. Recently, the smoking-gun evidence for the proton acceleration has been first detected from the middle-aged SNRs, IC443 and W44, through the discovery of the low-energy cutoff of π^0 decay with *Fermi*-LAT (Ackermann et al., 2013). Thus, it is very important to observe the broadband spectrum from radio to TeV γ-ray for the elucidation of the particle acceleration mechanisms. Here, we briefly introduce each of the emissions and the details can be found in some textbook like Rybicki and Lightman (1986).

1.4.1 Synchrotron radiation

Synchrotron radiation is the radiation from accelerated electrons who are gyrating in the amplified magnetic field near the SNR shock. The radiation widely spans from radio to hard X-ray, and the radio emission comes mainly from mildly relativistic electrons and X-ray is produced by ultra-relativistic electrons. The power per unit frequency ν emitted by single electron with the Lorentz factor γ of the perpendicular and parallel component to the particle motion is, respectively,

$$P_{\perp}(\nu,\gamma) = \frac{\sqrt{3}e^3 B\sin\alpha}{2m_e c^2}\left[F\left(\frac{\nu}{\nu_c}\right) + G\left(\frac{\nu}{\nu_c}\right)\right], \tag{1.38}$$

$$P_{||}(\nu,\gamma) = \frac{\sqrt{3}e^3 B\sin\alpha}{2m_e c^2}\left[F\left(\frac{\nu}{\nu_c}\right) - G\left(\frac{\nu}{\nu_c}\right)\right], \tag{1.39}$$

where $F(x)$ and $G(x)$ is the dimensionless function defined as

$$F(x) = x\int_x^{\infty} K_{\frac{5}{3}}(y)dy,\ G(x) = xK_{\frac{5}{3}}(x), \tag{1.40}$$

with the n-th order of second kind Bessel function K_n. α is the pitch angle between the particle velocity and magnetic field, and ν_c is the critical frequency defined as

$$\nu_c = \frac{3\pi\gamma^2 eB\sin\alpha}{m_e c}. \tag{1.41}$$

Therefore, The total power becomes

$$P_{\rm tot}(\nu,\gamma) = P_{\perp}(\nu,\gamma) + P_{||}(\nu,\gamma) = \frac{\sqrt{3}e^3 B\sin\alpha}{m_e c^2}F\left(\frac{\nu}{\nu_c}\right). \tag{1.42}$$

If the electrons have a power-law distribution:

$$N_{\rm e}(\gamma)d\gamma = K\gamma^{-q}d\gamma, \tag{1.43}$$

the Synchrotron emissivity $\epsilon_{\rm syn}$ can be obtained by integrating the combination of equation (1.42) and (1.43) over all the Lorentz factors,

$$\begin{aligned}\epsilon_{\rm syn}(\nu) &= \int_0^\infty P_{\rm tot}(\nu,\gamma)N_{\rm e}(\gamma)d\gamma \\ &= \frac{\sqrt{3}e^3KB\sin\alpha}{m_{\rm e}c^2(q+1)}\Gamma\left(\frac{3q+19}{12}\right)\Gamma\left(\frac{3q-1}{12}\right)\left(\frac{2\pi m_{\rm e}c}{3eB\sin\alpha}\nu\right)^{-(q+1)/2}\end{aligned} \tag{1.44}$$

where $\Gamma(x)$ is the gamma function.

The energy-loss rate of electrons due to the Synchrotron radiation is given by

$$\dot{E}_{\rm syn}(\gamma_e) = -\frac{4}{3}c\sigma_{\rm T}\gamma_e^2\beta_e^2\left(\frac{B^2}{8\pi}\right), \tag{1.45}$$

where $\sigma_{\rm T}$ is the Thomson cross section.

The linear polarization of Synchrotron radiation is sometimes detected from SNRs. The polarization degree for the single particle with energy γ is

$$\Pi(\nu,\gamma) = \frac{P_\perp(\nu,\gamma) - P_{||}(\nu,\gamma)}{P_{\rm tot}(\nu,\gamma)} = \frac{G(\nu/\nu_c)}{F(\nu/\nu_c)}. \tag{1.46}$$

Considering the power-law distribution of non-thermal particles, i.e., equation (1.43), the total polarization degree becomes

$$\Pi = \int_0^\infty \Pi(\nu,\gamma)N_{\rm e}(\gamma)d\gamma = \frac{q+1}{q+7/3}. \tag{1.47}$$

If the power-law index q is 2, the index and the degree of Synchrotron emission takes -1.5 and $\sim$ 70%, respectively. This negative power-law index is often used to identify radio-loud sources as SNRs. On the other hand, this high polarization degree are seldom observed because of depolarization of dense gases around SNRs.

1.4.2 Inverse Compton Scattering

Relativistic electrons can scatter low-energy photons of background fields such as the cosmic microwave background radiation (CMB), the infrared, optical, and UV fields radiated from the hot stars. The scattered photons gain the energy from the electrons and are observed as very high energy radiation.

This process can be described accurately when the energy of soft photons is substantially less than the rest mass energy of electrons, i.e. the Thomson limit. Beyond this limit, a quantum mechanical correction is needed for the cross-section and is called the Klein-Nishina effect. The Compton scattering emissivity using the full Klein-Nishina cross-section for relativistic electrons scattering an isotropic photon field component with energy distribution $n_j(E_t)$ (e.g., Jones, 1968; Blumenthal and Gould, 1970) is given by:

$$\epsilon_{\mathrm{IC},j}(E_\gamma) = \int_0^\infty dE_t n_j(E_t) \int_{\gamma_{e,\mathrm{th}}}^\infty d\gamma_e N_e(\gamma_e) \sigma_{\mathrm{KN}}(E_t, \gamma_e; E_\gamma), \tag{1.48}$$

where

$$\sigma_{\mathrm{KN}}(E_t, \gamma_e; E_\gamma) = \frac{2e^4\beta c}{m_e c^2 \gamma_e^2 E_t} \left[2q \ln q + (1+2q)(1-q) + \frac{\Gamma^2 q^2 (1-q)}{2(1+\Gamma q)} \right], \tag{1.49}$$

$$q = \frac{E_\gamma}{\Gamma(\gamma_e m_e c^2 - E_\gamma)}, \tag{1.50}$$

$$\Gamma = \frac{4E_t \gamma_e}{m_e c^2}; \tag{1.51}$$

E_t is the target photon energy, and $\gamma_{e,\mathrm{th}}$ is the threshold energy of electron which can scatter the target photon with the energy E_t up to the energy E_γ, given by

$$\gamma_{e,\mathrm{th}} = \frac{1}{2m_e c^2} \left[E_\gamma + \sqrt{E_\gamma^2 + \frac{E_\gamma (m_e c^2)^2}{E_t}} \right]. \tag{1.52}$$

The target photon field $n_j(E_t)$ can be approximately represented using the blackbody distribution as

$$n_j(E_t) = \frac{15 U_j}{(\pi k_{\mathrm{B}} T_j)^4} \frac{E_t^2}{\exp\left(E_t / k_{\mathrm{B}} T_j\right) - 1}, \tag{1.53}$$

where U_j and T_j is the energy density and temperature of photon field j. For example, $U_j = 0.25$ eVcm^{-3} and $T_j = 2.7$ K are taken for CMB. The total emissivity can be obtained by summing up all seed photon fields.

The energy loss rate is given by

$$\dot{E}_{\mathrm{IC}}(\gamma_e) = -\frac{4}{3} c \sigma_{\mathrm{T}} \gamma_e^2 \beta_e^2 \sum_j U_j \kappa(\gamma_e, T_j), \tag{1.54}$$

where

$$\kappa(\gamma_e, T_j) = \frac{\sigma_c(\gamma_e, T_j)}{\sigma_{\rm T}(1 + \gamma_e k_{\rm B} T_j/(m_e c^2))} \tag{1.55}$$

is the correction factor between the Thomson regime and the Klein-Nishina regime, and $\sigma_{\rm c}$ is the cross-section of the Compton scattering.

1.4.3 Bremsstrahlung

Bremsstrahlung, which is often called the free-free emission, is produced when the charged particles encounter with other charged particles and are accelerated due to the Coulomb force. When the emitters (electrons or positrons) have the Maxwellian distribution, the emission is also called *thermal bremsstrahlung*, whereas *non-thermal bremsstrahlung* is originated from the non-thermal distribution of the emitters. The power per unit frequency emitted by a single electron with the velocity v is given by

$$\frac{d^2\sigma}{d\nu dv} = \frac{16\pi e^6}{3\sqrt{3}c^3 m^2 v} Z_i^2 n_i n_e g_{\rm ff}(\nu, v), \tag{1.56}$$

where $g_{\rm ff}(\nu, v) = \sqrt{3}/\pi \ln(b_{\rm max}/b_{\rm min})$ is the gaunt factor, and $b_{\rm min}$ and $b_{\rm max}$ are a minimum and maximum of the impact factor. Here, we assume the electron population has the Maxwellian distribution,

$$f(v)d^3v = 4\pi v^2 \left(\frac{m_e}{2\pi k_{\rm B} T_e}\right)^{3/2} \exp\left(-\frac{m_e v^2}{2k_{\rm B} T_e}\right) dv. \tag{1.57}$$

The total emissivity can be obtained by integrating the combination of equation (1.56), (1.57) and all ion species i,

$$\begin{aligned} \epsilon_{\rm ff}(\nu, T_e) &= \sum_i \int_{v_{\rm min}}^{\infty} \frac{d^2\sigma}{d\nu dv} f(v) d^3v \\ &= \frac{32\pi e^6}{3m_e c^3} \left(\frac{2\pi}{3k_{\rm B} m_e}\right) \exp\left(-\frac{h\nu}{k_{\rm B} T_e}\right) \sum_i Z_i^2 n_i n_e \bar{g}_{\rm ff}(\nu, Z_i), \end{aligned} \tag{1.58}$$

where $\bar{g}_{\rm ff}(\nu, Z_i)$ is the velocity-averaged gaunt factor and is the value of the order of 1. As well, the emissivity of non-thermal bremsstrahlung can be written as

$$\epsilon_{NT}(E_\gamma) = 4\pi n_p \int N_e(\gamma_e) \left[\Delta_p \left(\frac{d^2\sigma}{d\gamma_e dE_\gamma}\right)_{e-p} + \Delta_e \left(\frac{d^2\sigma}{d\gamma_e dE_\gamma}\right)_{e-e}\right] d\gamma_e, \tag{1.59}$$

where $(d^2\sigma/d\gamma_e dE_\gamma)_{e-p,e}$ are the differential cross-section of electron-proton and electron-electron scattering, and $\Delta_{p,e}$ are the correction factor for the number density of proton and electron due to the presence of heavy ions, respectively. The formulae of the cross-sections above are quite complicated and beyond the scope of this dissertation. You can refer to Koch and Motz (1959) and Haug (1975) about them for instance.

The energy-loss rate of non-thermal bremsstrahlung for a fully-ionized medium can be obtained by Ginzburg and Syrovatskii (1964) and Blumenthal and Gould (1970),

$$\dot{E}_{\rm brems}(\gamma_e) = -\left(\frac{8e^6 n_p \eta_{\rm He}}{m_e c^2 \hbar}\right)(\ln\gamma_e + 0.36)(\gamma_e + 1), \tag{1.60}$$

where $\eta_{\rm He}$ is an enhancement factor due to the presence of Helium.

1.4.4 Pion decay

High-energy protons (and heavy ions) could inelastically collide with their surrounding gas and produce pions. These mesons are short-lived and finally decay into secondary particles such as photons, electrons, positrons, and so on. Especially, the neutral pions decay into two photons and if the cosmic-ray proton has a substantial energy above the rest-mass energy of pion, $m_{\pi^0}c^2$, the created photons also have sufficient energy. The photon energy $E_{\rm ph}$ is known to be almost one-tenth of the CR proton energy E_p, that is $E_{\rm ph} \sim 100$ TeV$(E_p/1$ PeV$)$. The detection of γ-ray through π^0 decay is ,hence, very important because this is only a direct evidence of the acceleration of CR proton for now (Ackermann et al., 2013).

The emissivity of π^0 decay γ-ray emission is

$$\epsilon_{NT}(E_\gamma) = 4\pi n_H \int \frac{d\sigma}{dE_\gamma}(T_p, E_\gamma) N_p(T_p) dT_p, \tag{1.61}$$

where N_p is the CR proton spectrum with the kinetic energy T_p, and n_H is the density of the target proton. To obtain the photon production rate $d\sigma/dE_\gamma$, it is needed to consider the complicated channels of various production and decay events. Here, we briefly introduce that some previous works parametrically obtain the production rate based on experimental data and well-reproduce the results of Monte-Carlo simulation (Kamae et al., 2006; Kafexhiu et al., 2014).

1.5 Motivation and Overview of the Thesis

In this dissertation, we will present a series of studies in an effort to develop a deeper understanding of the connections among SN explosion, the remnant of it, cosmic-ray acceleration. To achieve this purpose, we will study the broadband non-thermal emissions from Galactic SNRs. We will employ a computational method and compare the observation data from the Very Large Array telescope, the *Fermi* Large Area Telescope, and ground-based Cherenkov telescope array to investigate these important aspects.

This thesis is composed of three topics discussed in Chapter 2, 3 and 4 respectively. Chapter 2 presents a simulation platform we have developed to predict broadband spectra and morphology of non-thermal emission from young shell-type SNRs, with hydrodynamical simulation coupled to NLDSA particle acceleration calculation. In chapter 3 and chapter 4, we adapt our simulation model to Type II and Type Ib/c SNRs embedded in a CSM environment linked to the mass-loss history of the progenitor, respectively. Summary of this thesis work and a discussion on future prospect will be found in Chapter 5.

Chapter 2

Time Evolution of Broadband Nonthermal Emission from Supernova Remnants in Different Circumstellar Environments

Part of this chapter was published as Yasuda & Lee 2019, ApJ, 876, 27.

2.1 Scope of this chapter

SNRs are commonly detected in multi-wavelength observations and some have been found to shine in a broad range of frequencies from radio all the way to TeV γ-rays. In general, they emit broadband non-thermal electromagnetic radiation due to their interactions with the interstellar matter (ISM) or circumstellar medium (CSM). The radio and non-thermal X-rays are believed to be produced by relativistic electrons through synchrotron radiation. The γ-rays can originate from both relativistic electrons through inverse Compton scattering (IC) and bremsstrahlung, as well as by relativistic protons through the π^0-decay channel from proton-proton inelastic scatterings, which are usually regarded as the *leptonic* and *hadronic* processes, respectively.

Fig. 2.1 shows the spectral energy distribution (SED) of SNRs which have been observed so far in the GeV to TeV energy range. The upper panel shows the overall SED from radio to 1 PeV, and the lower panel shows the γ-ray SED from 10 MeV to 1 PeV. In most cases, the radio and non-thermal X-ray spectrum can be satisfactorily reproduced by a synchrotron origin regardless of SNR age, but the differences in the observed γ-ray spectra among these SNRs are remarkable.

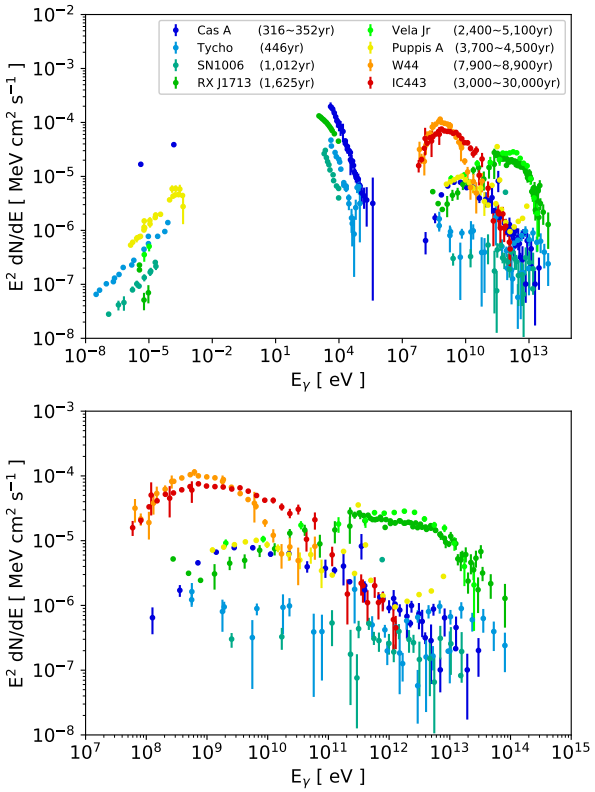

FIGURE 2.1: Upper panel: multi-wavelength SED of the SNRs whose γ-ray flux is detected. The color of data points almost represents the SNR age, the redder the color become, the older the age of SNRs become. Lower panel: the same plot as the upper panel, but energy range is from 10 MeV to 1 PeV.

Whether the γ-rays are produced by either *hadronic* or *leptonic* (or both) channel has a large implication on the particle acceleration mechanism, such as the injection efficiencies of the supra-thermal particles, the maximum energy of the accelerated particles, and the overall acceleration efficiency. These aspects can vary significantly among different individual SNRs depending on their ambient environment, age, and progenitor system which need to be fully understood in a consistent picture in order to examine the SNR population as a dominant source of Galactic CRs. However, the model interpretation is still often found to be controversial and remains to be a subject for discussion.

A general picture has been proposed by recent works (e.g., Yuan, Liu, and Bi, 2012) that the observed properties of the γ-ray emission from SNRs are mainly determined by the gas density in the their surrounding environments, i.e., the dominant component of the γ-ray flux is IC if the SN occurred in a relatively tenuous medium, while the π^0-decay component dominates in a denser medium such as a molecular cloud.These results, however, are

usually based on phenomenological fitting of the observed photon SED from individual SNRs using simple one-zone models. From the theoretical point of view, previous works (e.g., Fang and Zhang, 2008; Tang, Reynolds, and Ressler, 2016; Gaggero et al., 2018) also follow the long-term time-evolution of broadband emission, but assumptions and simplifications like one-zone hydrodynamical model and simple power-law CR spectrum are usually employed in these calculations. Currently, there are few studies that follow the long-term time evolution of the broadband emission together with the hydrodynamical evolution of the SNRs coupled to a self-consistent treatment of DSA at the shocks. Here, using a multi-zone hydrodynamical simulation coupled with an efficient particle acceleration, we generate a grid of evolutionary models of SNRs interacting with various kinds of ISM/CSM environments up to a few 1000 yrs over an observation-based parameter space. Our results are analyzed to explore general trends in the characteristics of the time-evolving SED that can be used in the future as a probe of the structure of the surrounding environment. Based on our results, we also predict the observability of typical young core-collapse and Type Ia SNRs by the upcoming ground-based VHE γ-ray observatory Cherenkov Telescope Array (CTA) .

In section 2.2, we introduce our numerical method for the evolutionary model of SNRs and the range of models adopted for the ambient environment. Section 2.3 describes our results and interpretations from the calculation, including the time-evolution of the SNR dynamics and the multi-wavelength spectra, and comparison to the currently available observational data. Concluding remarks and summary can be found in Section 2.4.

2.2 Method

2.2.1 Simulation code and included physics

We develop a hydrodynamical code to investigate the effect of CSM interaction on the long-term evolution of non-thermal radiations from SNRs. The code performs 1-D spherically symmetric hydro simulations on a Lagrangian mesh based on the VH-1 code (e.g., Blondin and Ellison, 2001) coupled with a semi-analytic non-linear DSA (NLDSA) calculation (see, e.g., Blasi, 2004; Caprioli, Amato, and Blasi, 2010; Caprioli et al., 2010) similar to the framework first introduced in the *CR-hydro-NEI* code (see, e.g., Lee, Ellison, and Nagataki, 2012a). The time-evolution of the SNR is numerically calculated through a Lagrangian hydrodynamics simulation starting from a self-similar

model for the SN ejecta as initial condition. The expansion of the SNR into whatever ambient environment adopted in a model is then followed by the hydro simulation, from which the shock dynamics is traced in real-time as an input for a NLDSA calculation. The NLDSA part provides a solution for the accelerated CR which feedbacks to the hydrodynamics through an effective gamma approach, i.e., a modified equation-of- state in the shocked medium (Blondin and Ellison, 2001), as well as the occurrence of a shock precursor.

NLDSA is sensitive to the shock velocity and the gas density and the magnetic field strength in the upstream environment, so we improve their code to calculate the DSA process and its hydrodynamical feedbacks at the shock every time the shock sweeps up gas in a new (unshocked) grid. This is particularly important in the case of a structured ambient medium such as a confined CSM due to an episodic mass loss from a massive star (see, Section 2.3.4).

In the NLDSA calculation, we obtain the phase-space distribution function $f(x,p)$ of the accelerated protons by solving the following diffusion-convection equation written in the shock-rest frame (e.g., Caprioli, Amato, and Blasi, 2010; Caprioli et al., 2010; Lee, Ellison, and Nagataki, 2012a), assuming a steady-state [1] distribution isotropic in momentum space,

$$[u(x)-v_A(x)]\frac{\partial f(x,p)}{\partial x}-Q(x,p)= \\ \frac{\partial}{\partial x}\left[D(x,p)\frac{\partial f(x,p)}{\partial x}\right]+\frac{p}{3}\frac{d[u(x)-v_A(x)]}{dx}\frac{\partial f(x,p)}{\partial p}, \tag{2.1}$$

where $D(x,p), u(x), v_A(x)$ are the spatial diffusion coefficient, gas velocity and Alfvén speed in the shock-rest frame at each position x. Hereafter, we label each quantity with a subscript '0', '1', and '2' denoting values at far upstream ($x=-\infty$), immediately upstream ($x=0^-$), and immediately downstream ($x=0^+$) from the shock, respectively. We assume a Bohm diffusion for the accelerating particles in this work, such that $D(x,p)=pc^2/3eB(x)$, where $B(x)$ is the local magnetic field strength at position x. The magnetic field is self-consistently calculated with magnetic field amplification (MFA) due to self-generated turbulence through resonant CR streaming instability

[1] We consider that it is reasonable to use the steady-state approximation as long as the dynamical time-scale of the SNR is longer than the DSA acceleration time-scale $t_{\rm acc}$. Known young SNRs are found to accelerate protons up to a maximum momentum $\sim$100 TeV/c or below, so that $t_{\rm acc}\sim D/u^2\sim 1(p/100\ {\rm TeV/c})(B/100\ \mu{\rm G})^{-1}(u/3000\ {\rm km/s})^{-2}$ yr, where D, u, p, B are the diffusion coefficient, the shock velocity, the particle momentum, and the amplified magnetic field. We find that the above condition can be satisfied within the scope of our models.

(e.g., Bell, 1978a; Caprioli et al., 2009). Following Blasi, 2004 and Blasi, Gabici, and Vannoni, 2005, we adopt the 'thermal-leakage' injection model for the DSA injection rate $Q(x,p)$ such that

$$Q(x,p) = \eta \frac{n_1 u_1}{4\pi p_{\rm inj}^2} \delta(x)\delta(p - p_{\rm inj}), \tag{2.2}$$

where $\eta = \{4/(3\sqrt{\pi})\}(S_{\rm sub}-1)\chi_{\rm inj}^3 e^{-\chi_{\rm inj}^2}$ and $S_{\rm sub} = (u_1 - v_{A,1})/(u_2 + v_{A,2})$ is the effective compression ratio that the streaming particles experience at the sub-shock position ($x = 0$). $p_{\rm inj} \equiv \chi_{\rm inj}\sqrt{2 m_{\rm p} k_{\rm b} T_{\rm p}}$ is the DSA injection momentum, where $m_{\rm p} = 1.6 \times 10^{-24}$ g is the mass of the proton, $T_{\rm p}$ is the proton temperature, and $\chi_{\rm inj}$ is a free parameter constrained by observations. By solving eq. (2.1), The distribution function at the shock position with a cutoff at a maximum momentum $p_{\rm max}$ can be written in implicit form as below,

$$\begin{aligned} f_1(p) = \quad & f(x=0,p) \\ = \quad & \frac{3S_{\rm tot}}{S_{\rm tot}U(p) - 1} \times \\ & \left[\frac{\eta n_0}{4\pi p_{\rm inj}^3} \exp\left(-\int_{p_{\rm inj}}^{p} \frac{dp'}{p'} \frac{3S_{\rm tot}U(p')}{S_{\rm tot}U(p') - 1}\right)\right] \times \\ & \exp\left\{-\left(\frac{p}{p_{\rm max}}\right)^{\alpha}\right\}, \end{aligned} \tag{2.3}$$

where $S_{\rm tot} = (u_0 - v_{A,0})/(u_2 + v_{A,2})$ is the effective total compression ratio of the CR-modified shock. The explicit expressions of $u(x)$, $v_A(x)$, $U(p)$ can be found in Lee, Ellison, and Nagataki (2012a) and reference therein. The parameter α describes the rollover shape near the high-energy cutoff which serves as a parametrization of the poorly understood escape process of the accelerated particles.

As for the electrons whose gyroradii are much smaller at thermal energies, the injection mechanism and efficiency relative to their proton and ion counterparts at strong collisionless shocks are still not fully understood, although a few first-principle kinetic simulations have shed new light onto this topic recently (see, e.g., Matsumoto et al., 2017, and reference therein). In this work, we constrain the electron-to-proton number ratio ($K_{\rm ep}$) at relativistic momenta below the cutoff by currently available data from multi-wavelength observations. Current observations of young γ-ray emitting SNRs have constrained $K_{\rm ep}$ to a range of a few 10^{-4} to $\sim 10^{-2}$ (e.g., H. E. S. S.

Collaboration et al., 2018). In this work, we adopt a $K_{\rm ep}$ by performing calibrations against data from prototypical Type Ia and core-collapse (CC) SNRs (see Section 2.3.1).

The maximum momentum of the accelerated protons is constrained by a number of physical conditions as described below, and its value is taken to be the minimum of the momenta obtained by applying these conditions, i.e., $p_{\rm max,p} = \min\{p_{\rm max,age}, p_{\rm max,feb}\}$, which changes with time as the shock propagates and evolves. The condition for $p_{\rm max,age}$ (*age-limited*) comes from the comparison of the SNR age $t_{\rm age}$ with the DSA acceleration time-scale $t_{\rm acc}$. An approximate expression for $t_{\rm acc}$ can be written as

$$t_{\rm acc} \approx \frac{3}{u_0 - u_2} \int_{p_{\rm inj}}^{p_{\rm max}} \frac{dp}{p} \left(\frac{D_0(p)}{u_0} + \frac{D_2(p)}{u_2} \right), \tag{2.4}$$

where $D_0(p)$ ($D_2(p)$) is the diffusion coefficient at far upstream (immediate downstream) from the shock.

The condition for $p_{\rm max,feb}$ (*escape-limited*) comes from the spatial confinement of the accelerating particles, i.e., a comparison of the particle diffusion length $L_{\rm diff}$ with a free-escape-boundary (FEB) set at a distance $L_{\rm feb}$ upstream from the sub-shock. Here $L_{\rm feb} = f_{\rm feb} R_{\rm sk}$ where $f_{\rm feb}$ is typically taken between 0.1 and 0.2 motivated by currently available models of SNR observations (e.g., Caprioli, Blasi, and Amato, 2009; Lee, Ellison, and Nagataki, 2012a). We fix $f_{\rm feb}$ at 0.1 in this study [2]. $L_{\rm diff}$ can be obtained by the following expression,

$$L_{\rm diff} = \left\langle \frac{D(x, p_{\rm max})}{u(x)} \right\rangle = \int_{-L_{\rm feb}}^{0} \frac{dx}{L_{\rm feb}} \frac{D_0(x, p_{\rm max})}{u(x)}. \tag{2.5}$$

For electrons, $p_{\rm max,e}$ is further restricted by the efficient energy loss due to radiation (*loss-limited*), that is $p_{\rm max,e} = \min\{p_{\rm max,age}, p_{\rm max,feb}, p_{\rm max,loss}\}$. The condition for $p_{\rm max,loss}$ (*loss-limited*) derives from the comparison of the acceleration time-scale $t_{\rm acc}$ with the time-scale of energy losses from non-thermal emission $t_{\rm loss}$. Typically, synchrotron radiation and IC dominate the energy loss of relativistic electrons, hence we can obtain $t_{\rm loss}$ as follows,

$$t_{\rm loss} = \frac{3 m_{\rm e} c^2}{4 c \sigma_{\rm T} U_{\rm B,2} \gamma} \left(1 + \sum_{i=1}^{N_{\rm p}} \frac{W_i \gamma_{k,i}^2}{U_{\rm B,2} (\gamma^2 + \gamma_{k,i}^2)} \right)^{-1}, \tag{2.6}$$

where $U_{\rm B,2} = {B_2}^2/8\pi$ is magnetic field energy density in downstream and

[2] In our models, $p_{\rm max}$ is typically constrained by *age-limited* for a $t_{\rm age} \leq 100$ yr, and then becomes *escape-limited* afterwards. The exact timing of the transition depends on the ambient medium in which the SN ejecta expands into in the early phase (see Fig. 2.5 and 2.7).

σ_T, γ are the Thompson cross section and electron Lorentz factor respectively. N_p is the number of components of external photon fields and $\gamma_{k,i} = 0.53 m_e c^2 / k_b T_i$ is the critical Lorentz factor. W_i, T_i are the energy density and effective temperature of the i-th component of the seed photon fields. In this study, we only consider the cosmic microwave background radiation (CMB) as the target photons for simplicity, so $W_i = 0.26$ eV cm^{-3} and $T_i = 2.7$ K.

After the particles are accelerated at the shock, they advect with the gas flow in the downstream region assuming an effective trapping by the strong, amplified magnetic turbulence. During the advection, they lose energy in the meantime through non-thermal emission due to interactions with the shocked ISM/CSM, and the adiabatic expansion of the SNR. Following Sturner et al., 1997, the radiation loss mechanisms include synchrotron radiation, bremsstrahlung, IC for electrons, and an addition of pion productions for protons. Coulomb loss is not included in this work but can be important for sub-GeV γ-ray emission.

Using the calculated proton and electron spectra in each position at any given age, we can then calculate the broadband non-thermal emission spectra. Our code includes synchrotron, IC, thermal and non-thermal bremsstrahlung and π^0-decay emission by the accelerated particles, taking also into account the additional contributions from secondary electrons and positrons on the synchrotron, IC and non-thermal bremsstrahlung components. We apply eq. (D1)-(D7) in Aharonian, Kelner, and Prosekin, 2010 to calculate the volume emissivities for synchrotron radiation, eq. (29)-(33) in Sturner et al., 1997 for IC, eq. (26)-(28) in Sturner et al., 1997 for non-thermal electron-proton bremsstrahlung, eq. (A1)-(A7) in Baring et al., 1999 for non-thermal electron-electron bremsstrahlung, and the parametrized model presented in Kamae et al., 2006 for the π^0-decay γ-ray emission. The code also computes the thermal bremsstrahlung emission using eq. (5.14) in Rybicki and Lightman, 1986. For this component, we assumed that the shocked gases are fully ionized after shock heating so that the electron number density is $n_e(x) = (1 + f_{He}) \times \rho(x)/\mu m_p$, where $\mu = 1.4$ is the mean molecular weight assuming the number fraction of helium f_{He} is 10% of hydrogen in the ambient medium.

The shock-heated proton and electron temperatures are assumed to be proportional to the mass number for a collisionless shock, and they are further evolved in the downstream due to adiabatic cooling/heating and equilibration through Coulomb collisions (i.e. eq. 5-31 in Spitzer, 1965). We also include free-free absorption and synchrotron self-absorption with eq.

(5.18) and (6.50) in Rybicki and Lightman, 1986 which are important in the radio band. The treatment of secondary electron/positron production through $\pi^{+/-}$ decay and subsequent photon emission follows the method described in Lee et al., 2015.

After the SNR has entered the radiative phase, the shock slows down to an extent that DSA is expected to be inefficient relative to the younger stages (see, however, Lee et al. (2015) and reference therein for a discussion on GeV-bright middle-aged SNRs). We do not treat the physics involved in radiative shocks in this work, and the simulations are terminated before the SNR becomes radiative. For all cases, we run the models up to an age of 5000 yr which is still within the Sedov-Taylor phase. We also do not consider the acceleration of heavy ions and possible DSA at the reverse shock in this study. These aspects will be discussed in future works.

2.2.2 Models for the surrounding environment

In this study, we look at two classes of simple but representative models for the ambient medium around a SNR. In Model A and its variants, we consider a uniform ISM-like environment which is usually expected for a Type Ia SNR (with exceptions),

$$\rho(r) = \mu m_{\rm p} n_{\rm ISM}, \tag{2.7}$$

$$B(r) = B_0, \tag{2.8}$$

where $n_{\rm ISM}$, B_0 are the ISM proton number density and magnetic field. We use an exponential profile for the SN ejecta in these models (Dwarkadas and Chevalier, 1998).

Model B and its variants adopt a power-law spatial distribution for the density in the ambient gas, which mimics the CSM created by a non-episodic isotropic stellar wind from a massive star prior to core-collapse supernova (CCSN) (Ellison et al., 2012, and references therein),

$$\rho(r) = \frac{\dot{M}}{4\pi V_{\rm w}} r^{-2}, \tag{2.9}$$

$$B(r) = \frac{(\sigma_{\rm w} V_{\rm w} \dot{M})^{1/2}}{r}, \tag{2.10}$$

where $\dot{M}$, $V_{\rm w}$, $\sigma_{\rm w}$ are the mass loss rate, wind velocity and the ratio between the magnetic field energy density and the wind kinetic energy density, i.e., $\sigma_{\rm w} \equiv P_{\rm B}/E_{\rm kin,w} = (B^2/8\pi)/(\rho V_{\rm w}^2/2)$. We use a flat core with power-law

envelope profile for the ejecta in these CCSN-like models (Truelove and McKee, 1999). In both classes of models, we assume that the gas velocity and temperature of the unshocked material are constant in space.

In Model C, we investigate the case of a non-steady mass loss history from a massive star in which a dense shell (or confined CSM) surrounding the ejecta is created due to mass ejection from the stellar envelope during the course of a few hundred years before the CC onset. The CSM is represented by a simple combination of two wind profiles where the one in the inner region having a higher density, as below,

$$\rho(r) = \begin{cases} \frac{\dot{M}}{4\pi V_{\rm w}} r^{-2} & (R_{\rm tr} < r) \\ \frac{\dot{M}_2}{4\pi V_{\rm w,2} R_{\rm tr}^2} \left(\frac{r}{R_{\rm tr}}\right)^{-n_{\rm pl,2}} & (r \leq R_{\rm tr}), \end{cases} \tag{2.11}$$

where $\dot{M}_2, V_{\rm w,2}, n_{\rm pl,2}$ are the mass loss rate, velocity and power-law index of the wind profile from an enhanced mass loss, and $R_{\rm tr}$ is the transition radius between the normal wind and the confined CSM region. As typical values, we consider an episode that an enhanced mass loss ejection with $V_{w,2} \sim 1000$ km/s occurred during the last ~ 1000 yr before explosion, and $R_{\rm tr} \sim 1.0$ pc.

2.3 Results and Discussion

2.3.1 Calibration models

To cross-check the robustness of the code and its capability of reproducing observations, we first consider two models, A0 and B0, with parameters chosen to match the multi-wavelength observation data of the Ia SNR Tycho and the CC SNR RX J1713.7-3946 (hereafter RX J1713) based on the multi-wavelength emission model from previous hydro simulations presented in Slane et al. (2014) and Lee, Ellison, and Nagataki (2012a), respectively. Models A and B and their variants will then be generated based on these observationally calibrated models by varying the ambient environment.

Tycho is identified to be the remnant produced by the historical supernova SN1572 which is classified as a Type Ia from its light-echo spectrum, chemical abundance pattern inferred from the X-ray spectrum and so on. Although it has been suggested that the ambient density around Tycho has an azimuthal gradient (Williams et al., 2013), we here assume a uniform ambient medium for simplicity. Fig. 2.2 shows the hydrodynamical and

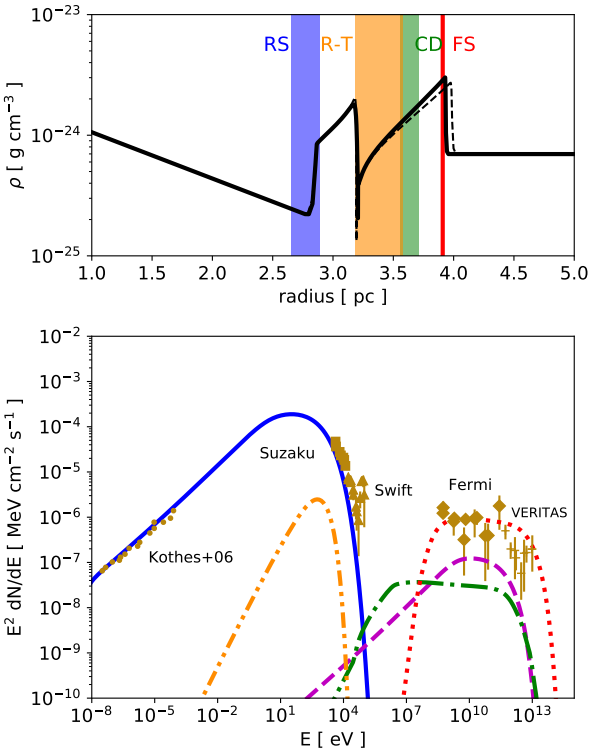

FIGURE 2.2: Upper panel: the solid line shows the calculated density distribution from Model A0 at an age of 446 yr. The color bands show the observed ranges of FS (red), CD (green) and RS (blue) radii of Tycho's SNR taken from Warren et al., 2005. The orange band indicates the extent of expected R-T mixing (Wang and Chevalier, 2001). The dashed line is the results from an identical model but without including CR feedback. Lower panel: the corresponding calculated non-thermal SED decomposed into its individual emission components, including synchrotron (blue solid), thermal bremsstrahlung (orange dash-dot-dotted), non-thermal bremsstrahlung (green dash-dotted), IC (magenta dashed) and π^0-decay (red dotted). The data points show the currently available observed fluxes - radio observations (Kothes et al., 2006, dotted), X-ray observations by *Suzaku* (Giordano et al., 2012, and references therein, square) and *Swift/BAT* (Troja et al., 2014, triangle), and γ-ray observations by *Fermi*-LAT (Giordano et al., 2012; Archambault et al., 2017, rhombus) and *VERITAS* (Acciari et al., 2011; Archambault et al., 2017, cross).

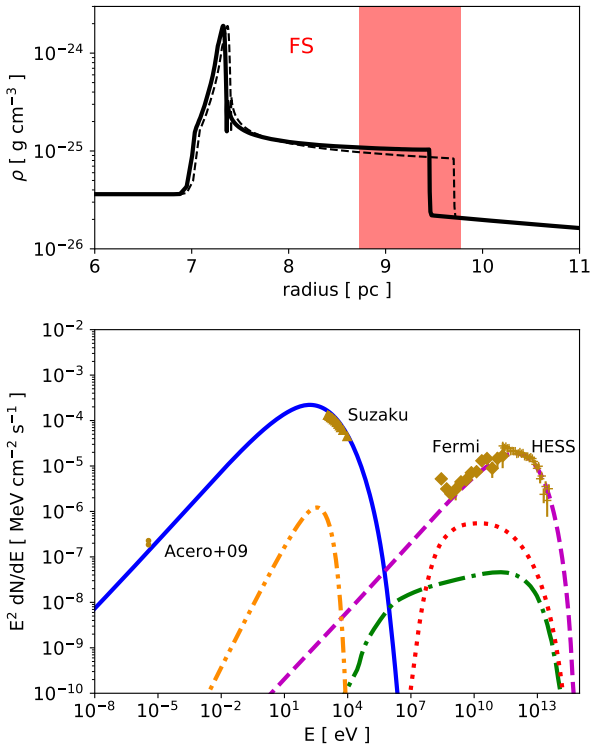

FIGURE 2.3: Results from Model B0. The format is the same as Figure 2.2. A normalization factor $f_{\rm norm} = 0.7$ has been applied to all calculated emission components to match the observed flux. Data points in lower panel: radio observations (Acero et al., 2009, dotted), X-ray observation by *Suzaku* (Lazendic et al., 2004, triangle) , γ-ray observation by *Fermi*-LAT (Aharonian et al., 2007; Aharonian et al., 2011; H. E. S. S. Collaboration et al., 2018, diamond) and H.E.S.S. (H. E. S. S. Collaboration et al., 2018, cross).

spectral results from our best-fit calibration model. The upper panel of Figure 2.2 shows the radial profile of the total mass density of the plasma (i.e., shocked/unshocked ISM and ejecta) at the current SNR age, $t_{\rm age} = 446$ yr. The solid line is the result from Model A0, and the thin dashed line is the result when particle acceleration is not included but otherwise identical to Model A0. The red, blue and green bands are the radii of the forward shock (FS), reverse shock (RS), and contact discontinuity (CD) inferred from observation (Warren et al., 2005). We can see that our simulation can reproduce the FS and RS positions [3], but not the case for the CD. If particle acceleration is efficient (i.e. small $\gamma_{\rm eff}$), however, it has been reported that Rayleigh-Taylor (R-T) instability can develop between the FS and CD (e.g., Blondin and Ellison, 2001; Warren and Blondin, 2013) and the CD position can possibly extend outward significantly (also see discussions in Slane et al., 2014). Our calculation can hence be considered to be in good agreement with observations on dynamics. The calculated SED at the same age is plotted in the lower panel. The observed fluxes are overlaid in the same plot. The agreement is found to be reasonable and reproduces the result of Slane et al. (2014) in their Model A. It can be seen that Tycho has a soft GeV-to-TeV spectrum from *Fermi* and *VERITAS* data, which can be explained by a π^0-decay origin with a softer than E^{-2} underlying proton spectrum, but the mechanism of spectral softening of the accelerated protons relative to the canonical E^{-2} prediction of DSA at a strong shock is not yet well understood.

RX J1713 is believed to be the product of SN393 which has been classified as a CCSN, and the SNR has been well detected in multi-wavelength observations. The origin of the bright γ-ray emission from RX J1713 is still being intensively discussed as mentioned above. Fukui et al., 2012 reported that the azimuthal distributions of H I and H_2 gases are consistent with the morphology of the observed TeV γ-rays, suggesting a hadronic origin. The gas distribution exhibits a low-density cavity surrounded by a dense shell, which has been suggested to be the result of the stellar wind of the progenitor prior to SN explosion inside a dense gas cloud. One the other hand, the observed hard γ-ray spectrum and the absence of optical signatures of the shock interacting with dense gas support a leptonic origin. In Model B0, we adopt a simple power-law $\rho \propto r^{-2}$ CSM model without considering the possibility

[3] As mentioned in Section 2, we only consider DSA at the FS in this work as a smoking-gun evidence of efficient DSA at the RS in SNRs is still absent. We can see in the upper panel of Fig. 2 the difference between the solid line and the dashed line which shows the results with and without feedbacks from an efficient DSA at the FS, respectively. DSA at the RS can be included in the code relatively easily when such evidence will surface in the future.

of shock-cloud interaction, which is similar to the best-fit model for RX J1713 presented in Lee, Ellison, and Nagataki (2012a). The results are summarized in Fig. 2.3, which shows the time snapshots of gas density profile and emission SED at $t_{\rm age}$ = 1625 yr. The FS position observed by *Fermi*-LAT (Acero et al., 2016) is shown by the red shaded region in the upper panel, which is consistent with the model. The CD and RS locations for this remnant are not well constrained due to the very faint X-ray emission from the ejecta. The radio and non-thermal X-ray spectra can be well-reproduced by the model, and the hard observed γ-ray spectrum is well-reproduced by an IC origin. The results are found to be consistent with the model by Lee, Ellison, and Nagataki (2012a).

Our result that the γ-ray emission is dominated by the IC component can be understood by considering the spatial distribution of the ambient gas density and magnetic field. The global magnetic field B_0 is as low as $\sim 6.6 \times 10^{-2} (\sigma_{\rm w}/0.004)^{1/2} (\dot{M}/7.5 \times 10^{-6}\, M_\odot/{\rm yr})^{1/2} (V_{\rm w}/20\,{\rm km/s})^{1/2} (r/9.5\,{\rm pc})^{-1}\ \mu$G at $t_{\rm age}$ = 1625 yr, so the amplified magnetic field B_2 is also moderate as $\sim$ 6.4 μG at the same time. This amplified but relatively low B-field behind the shock leads to an inefficient synchrotron loss such that the electrons can be accelerated to momenta capable of powering the observed γ-rays through the IC mechanism. Meanwhile, the ambient gas density also decreases rapidly as the SNR expands into the wind, so that the π^0 decay component is effectively suppressed.

We also note that we applied a flux normalization factor, $f_{\rm norm} = 0.7$, for all calculated emissions to match the observations mainly for two reasons; the distance of the SNR and a volume filling factor. We assume 1.0 kpc as the distance of RX J1713 in this work, which involves uncertainty. While our models assume spherically symmetry, many SNRs like RX J1713 are not a perfect spherical shell in gamma-rays (see, e.g., Fig.1(a) in Fukui et al., 2012). In other words, a prefactor < 1 has to be applied to our spectral SED to account for this volume filling factor. These uncertainties can be interpreted as the possible origins of $f_{\rm norm}$ in our models.

Based on our calibrated models A0 and B0 for an Ia and a CC SNR respectively, we now parametrically study the time evolution of broadband non-thermal SED from SNRs interacting with different ambient environments. We note that we have chosen an ejecta mass of $M_{\rm ej} = 3.0\ M_\odot$ to calibrate with RX J1713 in Model B0, but the ejecta mass can vary for different CC SN progenitors and SN types (e.g., Nicholl et al., 2015). Therefore, for Model B with a power-law CSM environment, we will survey over two ejecta models

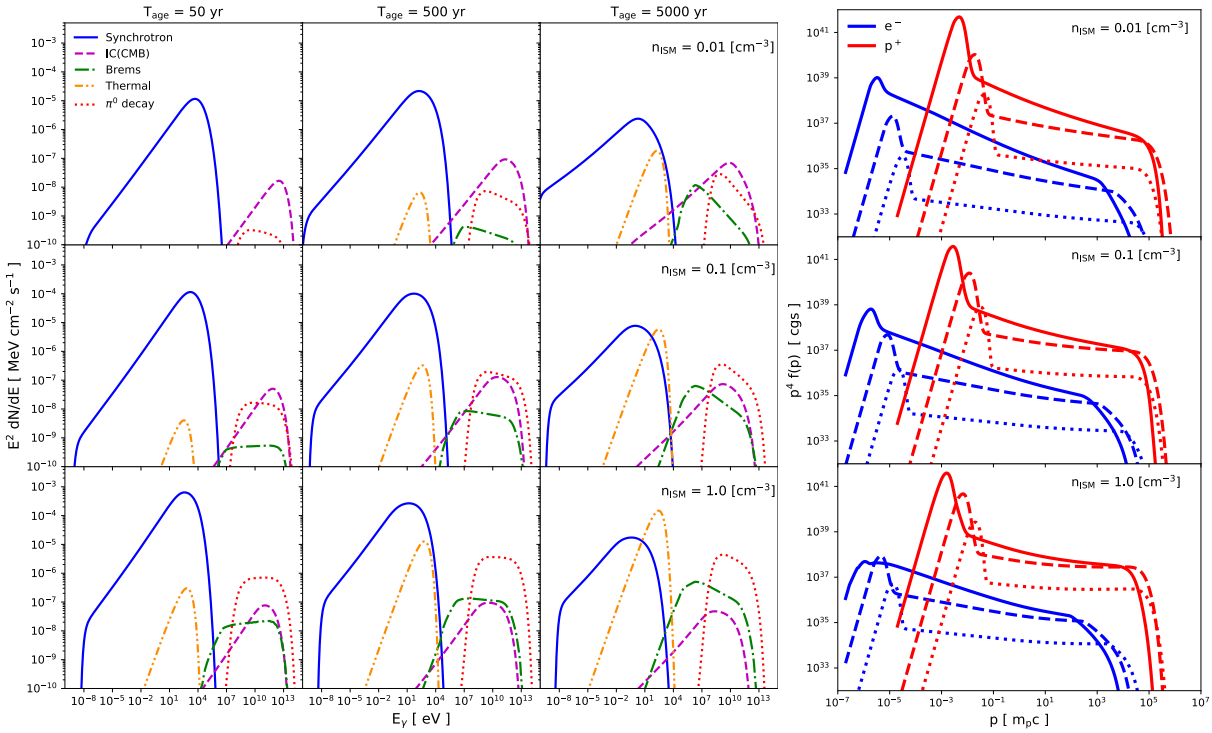

FIGURE 2.4: Left panel: time evolution of volume-integrated broadband SED from Type Ia SNR models with different ISM densities. Here $t_{\rm age}$ = 50, 500, 5000 yr moving from left to right panels, and $n_{\rm ISM}$ = 0.01, 0.1, 1.0 cm^{-3} from top to bottom which correspond to Model A1, A2 and A3 respectively. The line formats are identical to the lower panel of Fig. 2.2 and Fig. 2.3. Right panel: time evolution of volume-integrated proton (red) and electron (blue) distribution functions with different ISM densities. Here $n_{\rm ISM}$ = 0.01, 0.1, 1.0 cm^{-3} moving from top to bottom, and the dotted, dashed and solid lines correspond to $t_{\rm age}$ = 50, 500 and 5000 yr, respectively.

with $M_{\rm ej} = 3.0, 10.0\ M_\odot$ respectively. Other parameters are kept identical to Model A0 and B0 unless otherwise specified. The model parameters are summarized in Table 2.2.

2.3.2 Ia SNR models with a uniform ISM-like ambient medium

The left panel of Fig. 2.4 shows the time evolution of the broadband SED from our Type Ia SNR models A1, A2 and A3 for three different ISM densities, and the right panel shows the corresponding evolution of the underlying CR distribution functions. Fig. 2.5 shows the time-evolution of important hydrodynamical and DSA outputs. In the GeV to TeV energy range, as time evolves, the flux of non-thermal bremsstrahlung (green dash-dotted line) and

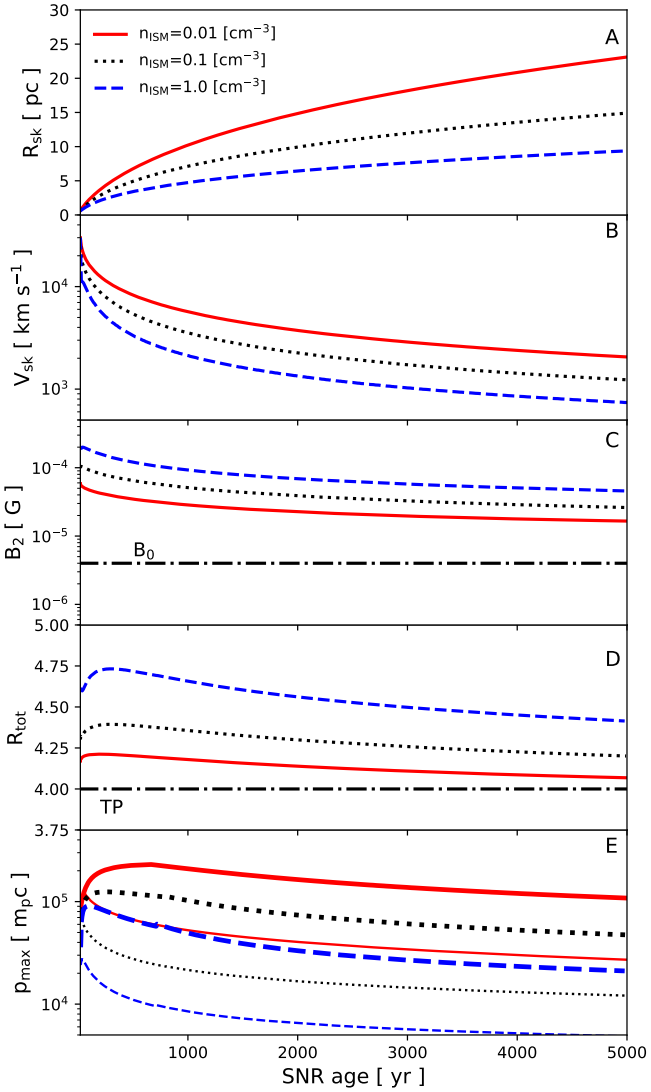

FIGURE 2.5: Time evolution of hydro and DSA outputs from our Type Ia models A1, A2 and A3 in three different ISM densities. Panel A shows the forward shock radius $R_{\rm sk}$, panel B shows the forward shock velocity $V_{\rm sk}$, panel C shows the magnetic field strength immediately downstream from the forward shock, panel D shows the total shock compression ratio, and panel E shows the maximum momentum $p_{\rm max}$ of accelerated protons (thick lines) and electron (thin lines). In all panels, the red solid, black dotted and blue dashed lines correspond to the cases of $n_{\rm ISM} = 0.01,\ 0.1,\ 1.0$ cm^{-3}, respectively. The dash-dotted line shows the value of the ambient magnetic field $B_0 = 4.0$ μG in panel C and the expected compression ratio from a test-particle (TP) approximation $R_{\rm tot} = 4$ in panel D.

π^0-decay (red dotted line) are found to be increasing monotonically, but there is not much accompanied brightening in the IC component (magenta dashed line). This difference in the evolution is mainly caused by the energy loss of the accelerated particles. The intensities of non-thermal bremsstrahlung, π^0-decay, and IC are proportional to the fluxes of the accelerated particles multiplied by the number density of their respective interaction targets, i.e., ISM gas for non-thermal bremsstrahlung and π^0-decay, and CMB photons for IC. However, the high-energy flux of the accelerated electrons is highly suppressed by a fast energy loss due to synchrotron radiation. The synchrotron loss time-scale, $t_{\rm syn} = 3m_{\rm e}c^2/4c\sigma_{\rm T}U_{\rm B}\gamma \sim 130(E_{\rm e}/10\ {\rm TeV})^{-1}(B/100\ \mu{\rm G})^{-2}$ yr is comparable to the SNR age with the post-shock magnetic field $\sim 100\ \mu$G being highly amplified in the shock precursor relative to the unshocked magnetic field $B_0 = 4.0\ \mu$G due to an efficient CR acceleration (see, panel C and E of Fig. 2.5). On the other hand, although the proton spectrum also suffers from energy-loss from p-p inelastic scatterings, even in the denser case of $n_{\rm ISM} = 1.0\ {\rm cm}^{-3}$, the energy loss time-scale $t_{\rm pp} = 1/\sigma_{\rm pp}v_{\rm p}n_{\rm SNR} \sim 3\times10^7 R_{\rm tot}^{-1}(n_{\rm ISM}/1{\rm cm}^3)^{-1}$ yr is still much longer than the SNR age, so the effect is not significant on the protons. As a result, the peak of the IC spectrum shifts to lower energy in the early phase due to the fast synchrotron loss, and the peak flux does not vary much as the SNR ages.

From the trend of flux evolution, we can see an interesting *leptonic*-to-*hadronic* transition in the moderately dense ISM case $n_{\rm ISM} = 0.1\ {\rm cm}^{-3}$ at a few 100 yr. The middle panels in Fig. 2.4 shows that the dominant flux of TeV range is IC at $t_{\rm age} = 50$ yr, while π^0 flux becomes comparable to IC at $t_{\rm age} = 500$ yr, and finally π^0 surpasses IC at $t_{\rm age} = 5000$ yr. On the other hand, in the thin and dense ISM cases, the transition does not happen within a few 1000 yr. This behavior is mainly dictated by the gas density interacting with the shock (see the uppermost and lowermost panels in Fig. 2.4).

We also see a systematic steepening of the γ-ray spectra with age in all models, which reflects the steeping of the proton spectrum from eq. (2.3). This effect comes from the deceleration of the FS with time due to an asymptote from free-expansion phase to Sedov phase. As a result, v_A which is high due to the amplified B-field becomes non-negligible compared to the gas velocities in the later phase, and the effective compression ratio S_{tot} is suppressed. The γ-ray spectrum hence becomes steeper with time because the spectral index of the particle distribution function is roughly proportional to $3S_{\rm tot}/(S_{\rm tot}-1)$ (Caprioli et al., 2009). The steepening is even more prominent in the thin ISM case since $v_A \propto \rho^{-1/2}$ is larger in these models.

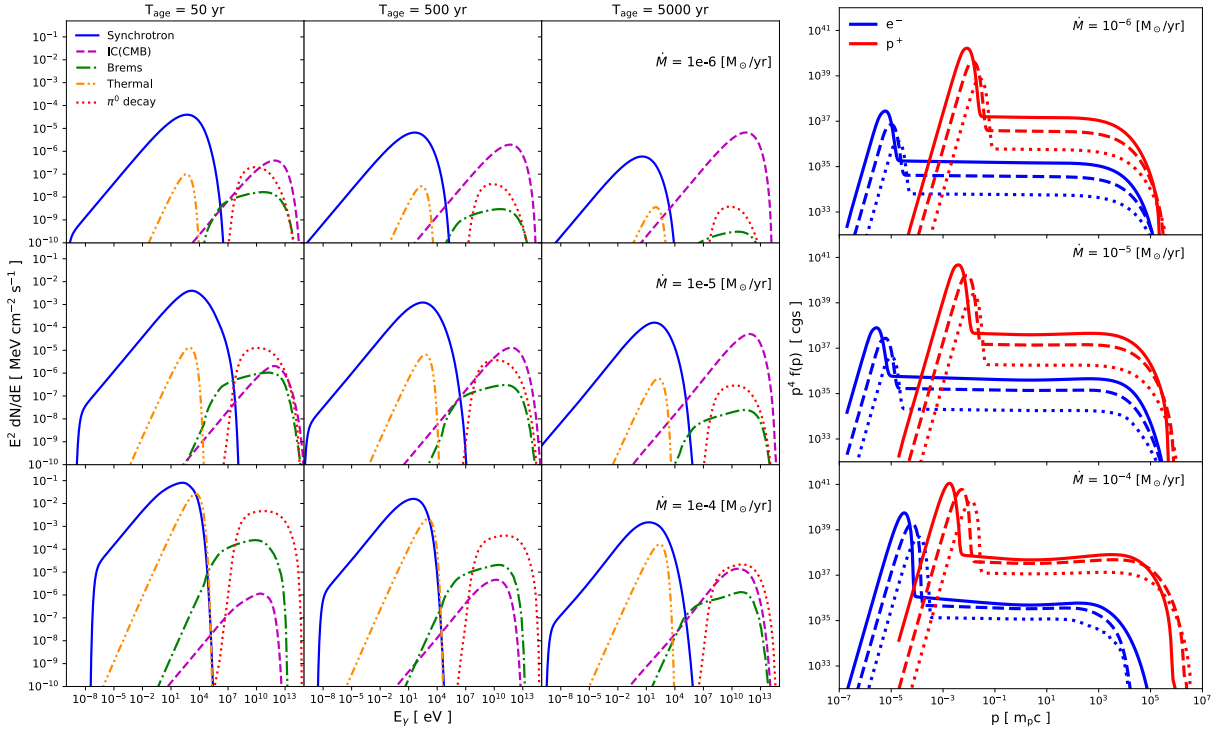

FIGURE 2.6: Left panel: SED evolution for our CC SNR models in different CSM environments. $t_{\rm age}$ = 50, 500, 5000 yr from left to right and $\dot{M} = 10^{-6}$, 10^{-5}, 10^{-4} $M_\odot$/yr from top to bottom which corresponds to Model B1, B2 and B3 respectively. The lines shown have the same format as in left panel of Fig. 2.4. Right panel: time-evolution of CR distribution function. $\dot{M} = 10^{-6}$, 10^{-5}, 10^{-4} $M_\odot$/yr from top to bottom. The lines shown have the same format as in right panel of Fig. 2.4.

2.3.3 CC SNR models with a power-law CSM-like ambient medium

3 $M_\odot$ case

Here we simulate the SNR evolution in a power-law CSM inside which a CCSN explodes with an ejecta mass of $M_{\rm ej} = 3.0\ M_\odot$. The results are shown in Fig. 2.6 and Fig. 2.7. The models correspond to a CSM with $\dot{M} = 10^{-6}, 10^{-5}, 10^{-4}$ $M_\odot$/yr for Model B1, B2 and B3 respectively. In the GeV-TeV spectrum, the IC flux increases, while the π^0-decay and non-thermal bremsstrahlung fluxes decrease as time proceeds, which is an opposite behavior compared to the uniform ISM models we see earlier. Since the CSM has a power-law density distribution in these CC SNR models, the CSM provides a dense target for producing π^0-decay and bremsstrahlung photons effectively which dominate the spectrum in the GeV-TeV range in the very early phase after the

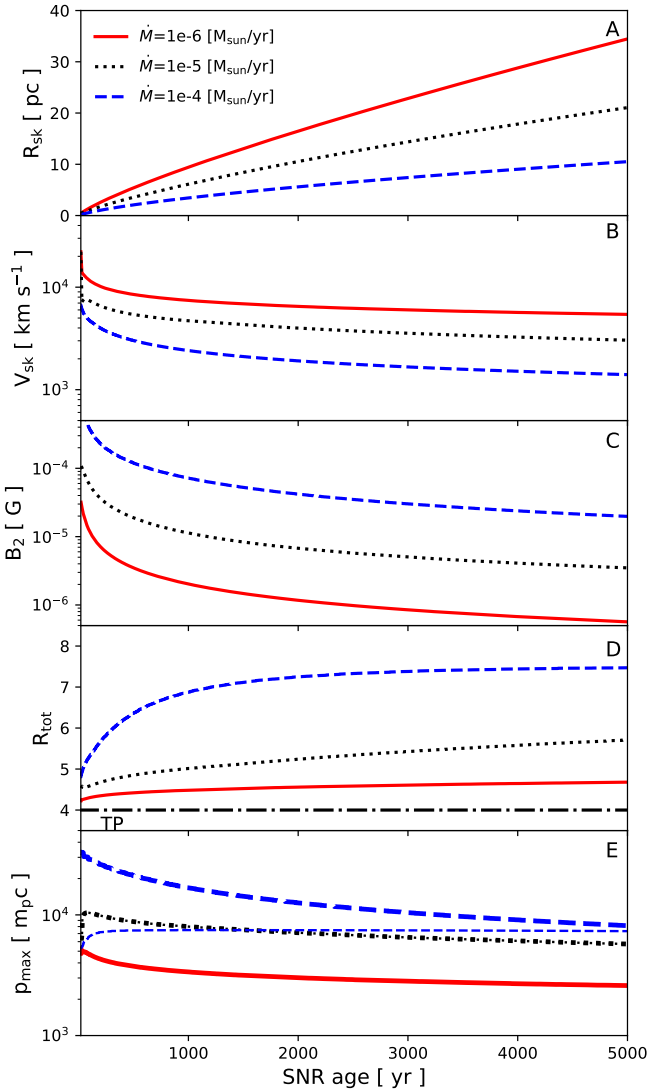

FIGURE 2.7: Time evolution of hydro and DSA outputs from model B1, B2, and B3. In all panels, the red solid, black dotted and blue dashed lines correspond to the cases of $\dot{M} = 10^{-6}, 10^{-5}, 10^{-4}\ M_\odot/\mathrm{yr}$ respectively. The line formats are identical to Fig 2.5.

explosion. However, as the CSM density decreases as r^{-2}, as time passes and the shock propagates through the wind material, the target gas density becomes low quickly, so the emission efficiency through π^0-decay and bremsstrahlung is suppressed accordingly. Moreover, the accelerated particles advected downstream from the shock also suffer from adiabatic loss to a larger extent than Model A due to the fast expansion of the SNR in a $\rho \propto r^{-2}$ wind. As a result, the fluxes of π^0-decay and non-thermal bremsstrahlung constantly decrease with age. On the contrary, the target photons of IC which are CMB here are homogeneous in space. The magnetic field is also lower than those we see in the uniform ISM cases (see panel C of Fig. 2.5 compared to that of Fig. 2.7). This means synchrotron loss is less important in the CC SNR models. Indeed, the quick shift of the peak energy of the synchrotron and IC components which is seen in Fig. 2.4 does not occur here, and the IC emission gradually increases with time with the peak staying at more-or-less the same energy range. These are the main reasons why the IC photons are constantly produced in the power-law CSM cases. In the center and bottom panels of Fig. 2.6, we can also see a low-energy cutoff in the synchrotron spectrum in the radio band. This is because free-free absorption is efficient at early time due to the dense unshocked CSM in front of the shock. The absorption becomes inefficient with time, however, as the SNR shock propagates into the relatively thin region of the CSM, so the cutoff shifts to lower frequencies.

Our SED evolution model for the CCSN with power-law CSM cases suggests a *hadronic*-to-*leptonic* transition in the GeV-TeV range if the wind density is moderately dense with a $\dot{M} = 10^{-5}$ $M_\odot$/yr, which is again the exact opposite behavior we see in the Ia SN cases with uniform ISM. We suggest that these contrasting spectral evolution and transition of dominant γ-ray component can be useful for probing the surrounding environment of SNRs, especially in the near future as the sample of γ-ray SNR observations is enlarged by future observatories such as the upcoming observatories such as CTA (see section 3.6).

10 $M_\odot$ case

The results from our CCSN models with an ejecta mass $M_{\rm ej} = 10\ M_\odot$ are shown in Fig. 2.8. For comparison, the results of $M_{\rm ej} = 3\ M_\odot$ are also overlaid. From panel A and B, it can be seen that while the shock dynamics for the case of $\dot{M} = 10^{-6}$ $M_\odot$/yr and $\dot{M} = 10^{-5}$ $M_\odot$/yr are affected by a different ejecta mass, the results for $\dot{M} = 10^{-4}$ $M_\odot$/yr are nearly identical. These

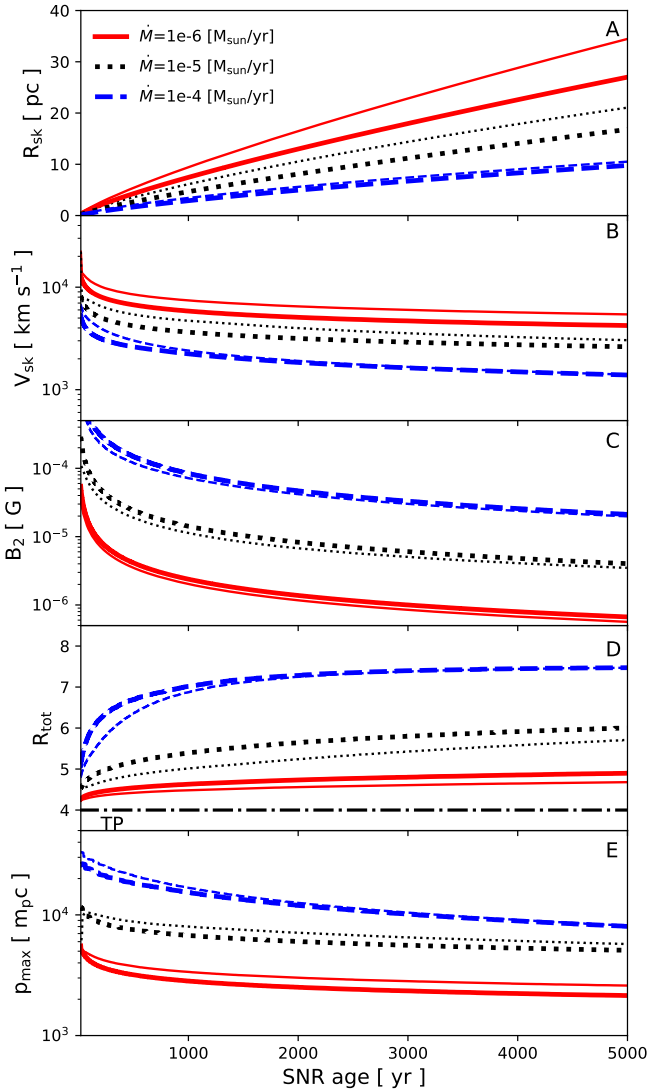

FIGURE 2.8: Same as Fig. 2.7, but with an ejecta mass of $M_{\rm ej} = 10.0\ M_\odot$. Only the $p_{\rm max}$ of protons is plotted here in panel E for clarity. The thick red solid, black dotted, and blue dashed lines show the results of model B4, B5, and B6. For comparison, thin lines show the results of the $3M_\odot$ case as in Fig. 2.7.

differences can be explained by a different evolutionary phase of the SNR at a given age. In the cases of $\dot{M} = 10^{-6}$ $M_\odot$/yr and $\dot{M} = 10^{-5}$ $M_\odot$/yr, the CSM density is relatively low and the mass swept up by the FS is smaller than the ejecta mass, the dynamics of these two cases thus follow the self-similar solution, $R_{sk} \propto (E_{SN}/M_{ej}A)^{1/5}t^{4/5}$ and $V_{sk} \propto (E_{SN}/M_{ej}A)^{1/5}t^{-1/5}$ (Chevalier, 1982a; Chevalier, 1982b), where $A \equiv \dot{M}/4\pi V_w$, which depends on the ejecta mass. On the contrary, the CSM material in the case of $\dot{M} = 10^{-4}$ $M_\odot$/yr are dense enough and the swept mass become comparable to the ejecta mass at $t_{age} \leq 1000$ yr, the dynamics hence follows the Sedov solution, $R_{sk} \propto (E_{SN}/A)^{1/3}t^{2/3}$ and $V_{sk} \propto (E_{SN}/A)^{1/3}t^{-1/3}$ (Sedov, 1959), which are independent of the ejecta mass.

As for the other quantities shown in Fig. 2.8 like B-field and p_{max}, the differences are found to be subtle only [4]. As a result, we do not see any remarkable difference in the non-thermal SED between the 3 $M_\odot$ and 10 $M_\odot$ models. We can conclude that it is hard to distinguish the progenitor from the non-thermal emission in the SNR phase, and other information which reflect the progenitor properties such as thermal X-ray emission lines are needed to link an observed SNR to its progenitor origin. In section 2.3.5 where we compare our results to observations, we will only show the results from the 3 $M_\odot$ models because of this insensitivity of the γ-ray emission to ejecta mass.

2.3.4 A case of pre-SN enhanced mass loss

Results from Model C where the $\dot{M}$ is boosted to 10^{-2} $M_\odot$/yr in the last 1000 yr before CC are shown in Fig. 2.9 and Fig. 2.10. Fig. 2.9 shows the phase-space distributions of the accelerated primary (solid) and secondary (dashed) particles in the upper panels, and the photon SEDs in the lower panels. We choose to show the results at $t_{age} = 400$ (left panels) and 1000 (right panels) yr because these time epochs represent the phases before and after the shock has crossed the interface at R_{tr} between the dense confined CSM and the less dense wind outside. In this model, the shock reaches R_{tr} at $t_{age} \sim 600$ yr (see, Fig. 2.10).

As the FS propagates in the region of dense CSM material with density $n \sim 10^4$ cm^{-3} and a high magnetic field ≥ 1 mG (see, panel C of Fig. 2.10), the electron maximum momentum $p_{max,e}$ is determined by the energy loss

[4]The fact that the shock velocities in the 10 $M_\odot$ cases are lower than those of the 3 $M_\odot$ models at any given age implies that the effects of CR back-reaction and shock modification becomes important at an earlier phase. This is evident from the slightly higher total compression ratio and amplified magnetic field, as shown in panel C and D in Fig. 2.8.

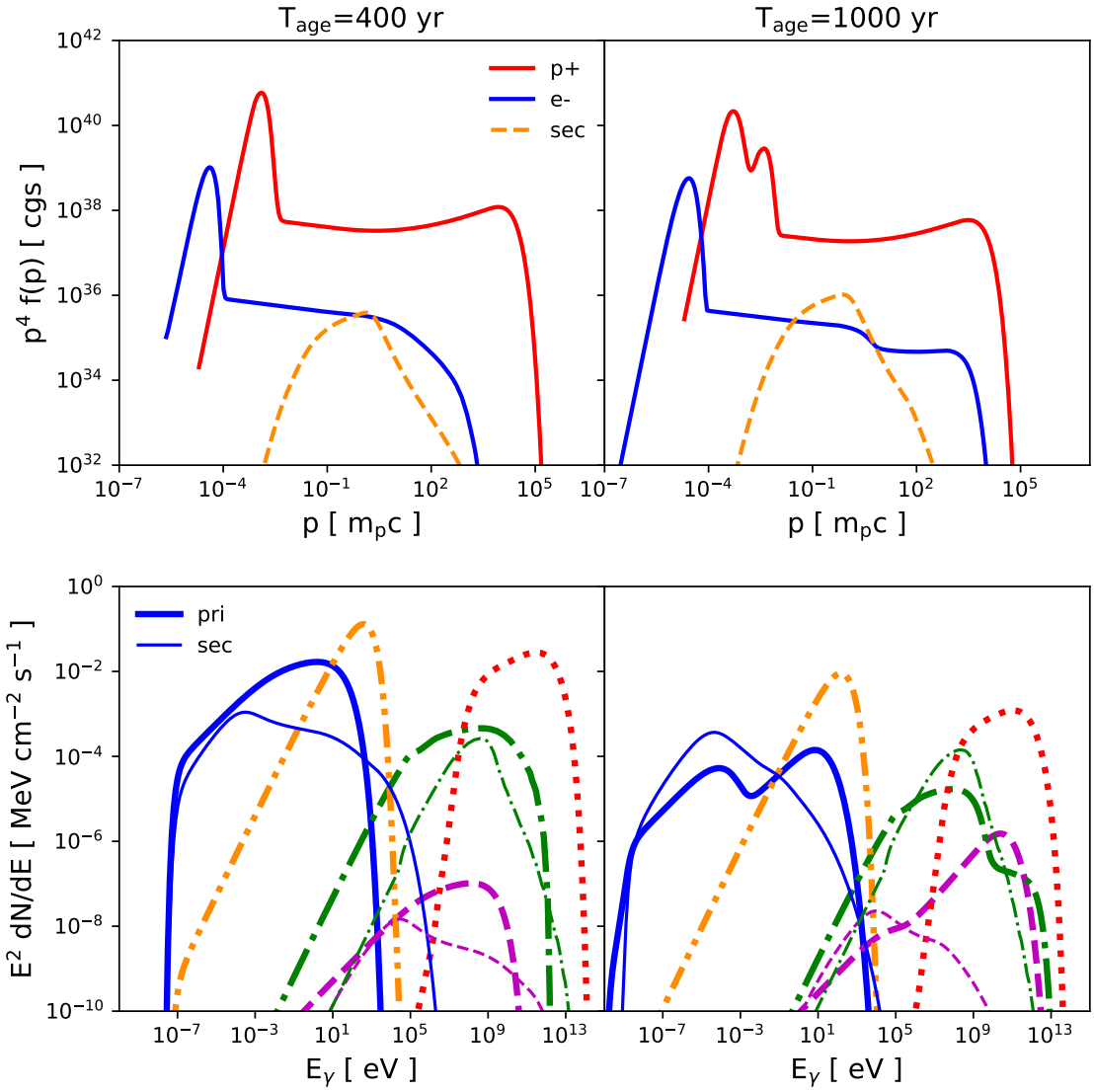

FIGURE 2.9: Time-evolution of the volume-integrated distribution function of the accelerated particles (upper panels) and broadband emission SED (lower panels), which correspond to Model C. Left and right panels show the results at $t_{\rm age}$ =400, 1000 yr, respectively. In the upper panels, the red solid, blue solid and orange dashed lines correspond to the primary protons, electrons, and secondary electrons/positrons, respectively. In the lower panels, the thick lines show the emission produced by the primary particles, and the thin lines are by the secondaries. The line colors are the same as Fig. 2.4.

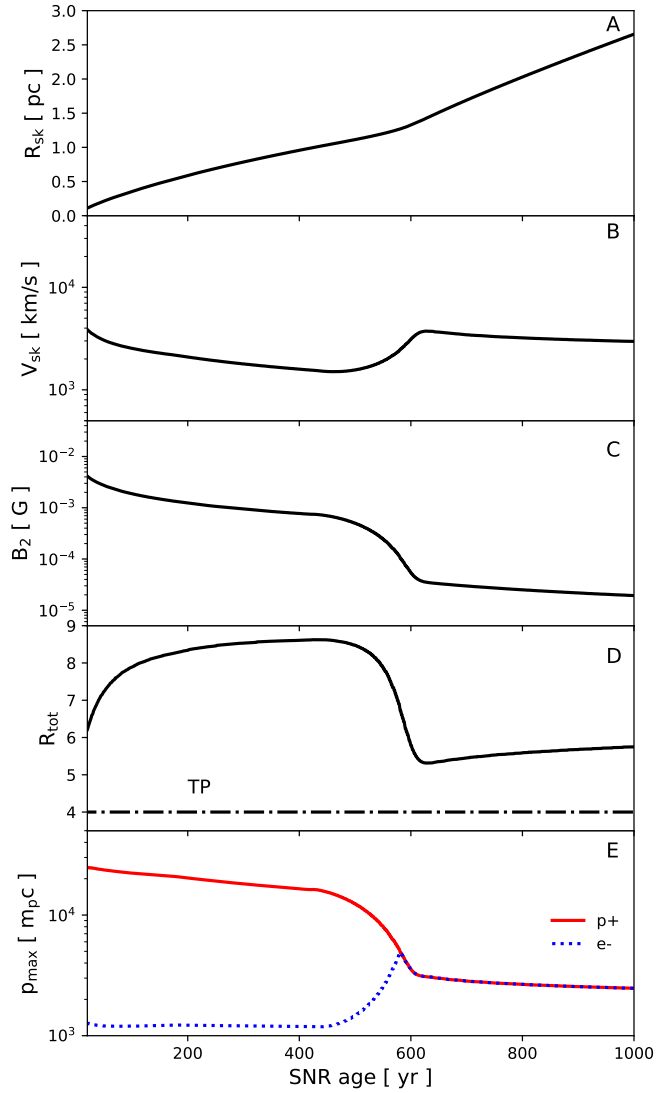

FIGURE 2.10: Time evolution of various values using model C. The values of each panel shows are the same as Fig. 2.5 and Fig. 2.7.

time-scale $t_{\rm loss}$ rather than the age or escape time-scale because $t_{\rm loss} \sim t_{\rm syn} \sim 12 B_{-3}^{-2} E_{12}^{-1}$ yr, where $B_{-3} = B_2/10^{-3}$G and $E_{12} = E_e/10^{12}$eV, is less than the SNR age at a given time (see, panel E of Fig. 2.10). However, as the FS breaks out from the dense inner shell, $p_{\rm max,e}$ is now limited by their escape through the FEB because the shock velocity is now restored to ~ 4000 km/s and the magnetic field decreases to ~ 10 μG (see, panel B, C and E in Fig. 2.10). Therefore, we can see two cutoffs at $p \sim 10\ m_{\rm p}c$ and $p \sim 10^3\ m_{\rm p}c$ in the volume-integrated electron spectrum (upper right panel in Fig. 2.9) while the proton spectrum has one cutoff only at $p \sim 10^4 m_{\rm p}c$. These effects of a transition from a dense wind to a lower density wind also reflects in the spectra of synchrotron, non-thermal bremsstrahlung and IC emission (see, lower right panel in Fig. 2.9).

In the radio range of the SED, before the shock breaks out from the dense region, the dominant component is synchrotron radiation from the primary electrons (solid) and a spectral cutoff can be seen at $E_\gamma \sim 10^{-7}$ eV due to a strong free-free absorption. However, after the breakout, the dominant component is now the synchrotron emission from the secondary electrons and positrons. The reason is as follows. Electrons accelerated earlier on in the dense wind suffer from rapid energy loss through synchrotron emission and adiabatic expansion, and the freshly accelerated electrons in the outer tenuous wind have a higher $p_{\rm max}$ as mentioned above, but the synchrotron radiation from these freshly accelerated electrons is relatively weak due to a lower magnetic field in the tenuous wind, therefore the synchrotron flux from the primaries decreases with time. On the other hand, the contribution from the secondaries do not decrease as rapidly because these secondary particles are produced via π^0-decay not only by the freshly accelerated protons, but also by the proton accelerated earlier on in the dense wind continuously as the protons do not lose their energy as quickly as the electrons. This is why the transition from primary to secondary dominance happens in the synchrotron radiation.

We suggest that this transition can potentially constrain the mass-loss history of massive stars. For example, the spectral index of synchrotron emission produced by the secondary particles is expected to be different from that produced by the primary electrons, which is evident from their very different distribution functions as shown in the upper panels of Fig. 2.9. In particular, the synchrotron spectrum from the secondaries tends to be harder in the radio band. In fact, hard radio indices are usually observed in older SNRs interacting with dense molecular clouds, such as IC443 (e.g., Castelletti et al.,

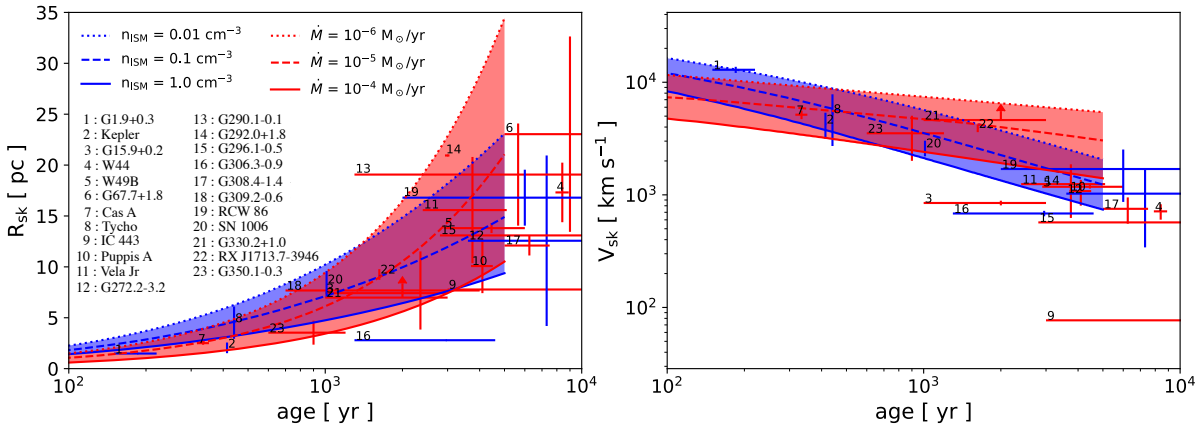

FIGURE 2.11: Left panel: FS location as a function of age. Blue (red) dotted, dashed, and solid line show the results of Model A1 (B1), A2 (B2), and A3 (B3), respectively. Right panel: FS velocity as a function of time. The observation data are shown by the blue (Ia) and red (CC) data points in both panels, and are summarized in Table 2.3.

2007; Castelletti et al., 2011). These remnants are also believed to be producing a significant amount of secondaries. If a harder-than-expected spectral index will be observed in young SNRs which is not colliding with any dense cloud at the moment, it is possible that the SNR has evolved inside a dense confined CSM in the past, which can provide a hint on an enhanced mass loss of the progenitor star prior to CC.

2.3.5 Model versus data

We now try to compare our simulation results to observation results so far in terms of dynamics (e.g., shock radius and velocity) and γ-ray luminosity to check if our models are able to reproduce the bulk properties of observed SNRs. We include data like SN type, distance, shock radius, shock velocity, and radio, GeV, and TeV fluxes of SNRs from a younger age ($\sim$ 100 yr) to middle age ($\sim$ 10,000 yr). We summarize these data in Table 2.3. The data on SNR radii with errors are taken from the *Fermi* catalog (Acero et al., 2016), and those without errors are determined by the size of the radio remnants and are taken from the *SNRcat* (Ferrand and Safi-Harb, 2012). The flux data is obtained again mainly from the *Fermi* and H.E.S.S (H. E. S. S. Collaboration et al., 2018) catalogs (see Table 2.3 for details); those with errors are for detected SNRs, and those without errors are the upper limits of non-detected SNRs.

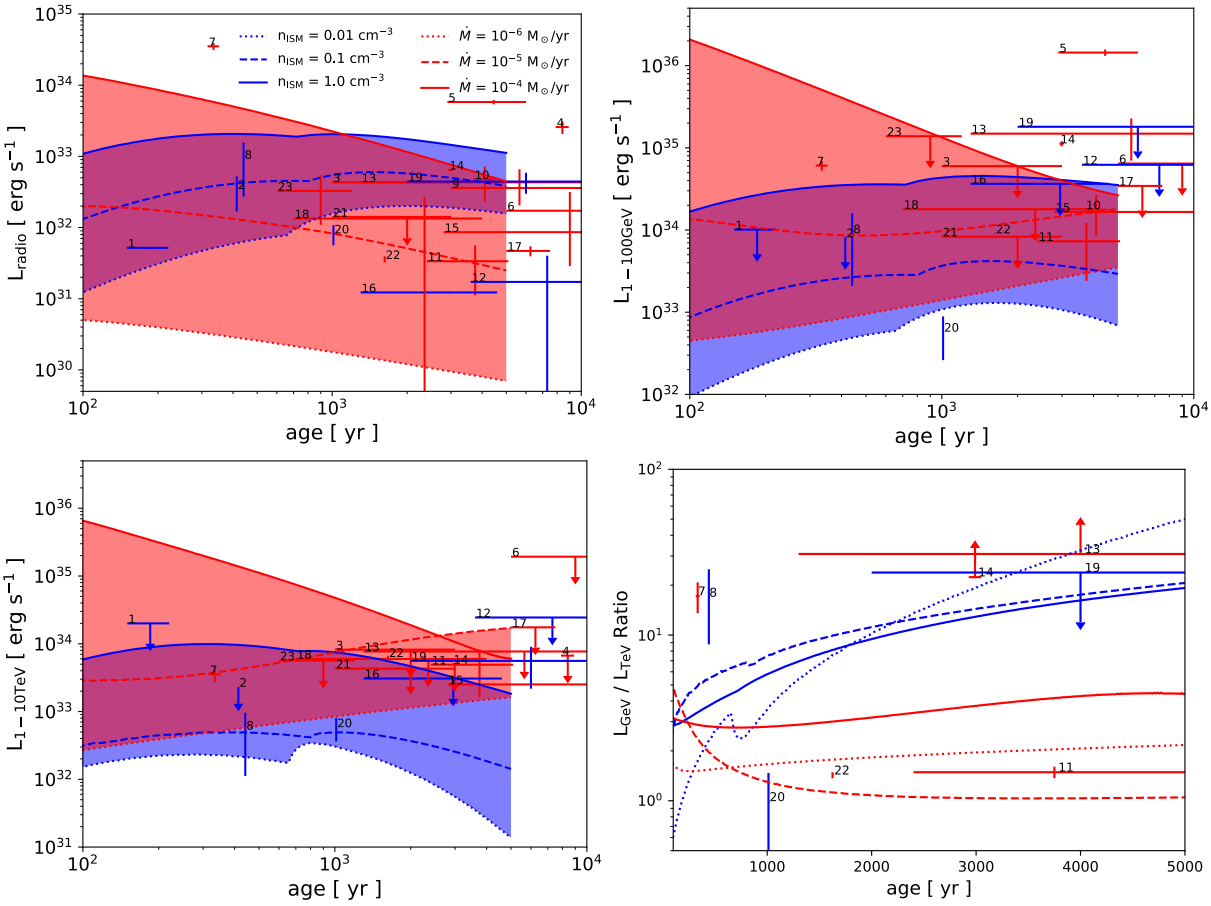

FIGURE 2.12: Upper left panel: radio luminosity at 1 GHz as a function of time. Upper right panel: integrated γ-ray luminosity from 1 GeV to 100 GeV as a function of time. Lower left panel: integrated γ-ray luminosity from 1 TeV to 10 TeV as a function of time. Lower right panel: the ratio of GeV to TeV luminosity as a function of time. The format of lines and data in all panels is the same as in Fig. 2.11.

Fig. 2.11 shows the comparison of dynamical properties including the shock radius and shock velocity as a function of time from our models with observations. The blue data points are for the Type Ia SNRs and red ones are for the CC SNRs. We label each SNR by a number as summarized in left panel of Fig. 2.11. In general, the overall trend of the observed distribution of shock radius and velocity as a function of SNR age can be explained by our simulation results for the parameter space we explored. There exist a few "outliers" which have small radii and velocities, which can be interpreted as SNRs interacting with a medium denser than what our models have considered. In fact, many of these are known to be interacting with dense molecular clouds at the moment.

Fig. 2.12 shows the time evolution of the luminosity in three different energy ranges. The upper left panel shows the luminosity of 1 GHz radio continuum emission, which reflects the time-evolution of synchrotron spectrum for both the uniform ISM cases and power-law CSM cases (see also, Fig 2.4 and Fig 2.6). Since synchrotron emissivity is proportional to the flux of accelerated electrons and the square of the local magnetic field strength, for the magnetic field which is constantly distributed in the uniform ISM cases, the synchrotron emissivity does not vary much and the spectral peak shifts to a lower energy with time, similar to the IC component previously discussed in sec. 2.3.2. On the other hand, in a power-law CSM case, the magnetic field decreases in proportion to r^{-1}, the synchrotron flux then also decreases with time just as the π^0-decay γ-rays do. Thus, radio luminosity increases gradually with time as a volume effect in the uniform ISM cases, but decreases in the power-law CSM cases.

The upper right and lower left panels show the GeV luminosity integrated from 1 GeV to 100 GeV and TeV luminosity from 1 TeV to 10 TeV as a function of age, respectively. For the uniform ISM cases, while the GeV luminosity increases with time, TeV luminosity decreases. At the bottom end of the predicted flux which corresponds to the case of $n_{\rm ISM} = 0.01$ cm^{-3}, the γ-rays are dominated by IC at all time, and the decrease of the TeV flux can be understood as the energy loss of the highest-energy electrons. For the other two cases with a denser ISM, the trend reflects the time evolution of not only the normalization but also the shape of the π^0-decay spectra predicted by these models. As seen in Fig. 2.4, the π^0-decay spectrum become softer as time passes by. The reason has been discussed in the end of sec. 2.3.2, which is mainly because of the increasing importance of the effect from v_A, i.e., the velocity of the magnetic scattering centers. As the shock sweeps up more material as the SNR ages, the π^0-decay flux increases with time in general, but the TeV flux decreases due to a spectral softening of the underlying proton distribution.

On the other hand, in the power-law CSM cases, both GeV and TeV luminosity decrease only in the case of the densest wind with $\dot{M} = 10^{-4} M_\odot/{\rm yr}$, but increase in the other two cases. This can be easily understood according to the discussion above in sec. 2.6 on the evolution of IC and π^0-decay fluxes, and the dominant component is π^0-decay in the case of $\dot{M} = 10^{-4} M_\odot/{\rm yr}$.

Here, to obtain the data points from the γ-ray observations, we assume that the observed spectra have a simple power-law distribution, so that the

integrated luminosity can be calculated using the following expression,

$$L_\Delta = 4\pi d_{\rm SNR}^2 \frac{(-\Gamma+1)(E_{\rm max}^{-\Gamma+2} - E_{\rm min}^{-\Gamma+2})}{(-\Gamma+2)(E_{\rm max}^{-\Gamma+1} - E_{\rm min}^{-\Gamma+1})} F_\Delta, \tag{2.12}$$

where $F_\Delta, \Gamma, d_{\rm SNR}, E_{\rm min}, E_{\rm max}$ are the integrated flux, photon index, distance to the SNR, minimum and maximum energies of the integrated energy range.

The radio luminosities from observations of both Type Ia and CC SNRs can be bulkly reproduced by our models with a few outliers such as Cas A and middle-aged SNRs interacting with MCs. As for the GeV and TeV observations, the statistics is still clearly very poor due to the small sample size of detected sources, so at the moment the comparison with the models is only preliminary. For older CC SNRs, a few outliers are found with significantly higher luminosities than our results. These are again mostly middle-aged SNRs interacting with dense MCs which are not covered by our parameter space.

The lower right panel shows the ratio of GeV to TeV luminosities which roughly quantifies the γ-ray spectral shape. Two trends can be seen in the result: one trend rises with time, and the other is nearly flat. These can be possibly explained by our discussion on flux evolution above. If π^0-decay is the dominant emission in γ-rays, the GeV luminosity increases and TeV luminosity decreases with time in uniform-ISM cases, and as a result, the ratio increases with time, while the ratio in power-law CSM case becomes nearly flat regardless of time because both GeV and TeV luminosities decrease with time, and case. If, however, IC is the dominant contributor, the SED evolves without changing its shape, so the ratio does not vary in any significant way with time. Indeed, the observation data also appear to split into two regions; $L_{\rm GeV}/L_{\rm TeV} \sim 1$ and $L_{\rm GeV}/L_{\rm TeV} \geq 10$ despite the poor statistics. If both GeV and TeV emissions can be observed from an increased number of SNRs in the future, we will be able to see if the SNRs will segregate into two groups in this plot, which can make this quantity a useful probe of the ambient environment and hence the progenitor origin of SNRs.

2.3.6 Prospects for Cherenkov Telescope Array

An instrument which can observe over a broad energy range from GeV to TeV energies with a high sensitivity, such as the Cherenkov Telescope Array (CTA), is ideal for a systematic investigation as introduced in this study. CTA can achieve an unprecedented sensitivity superior to existing detectors

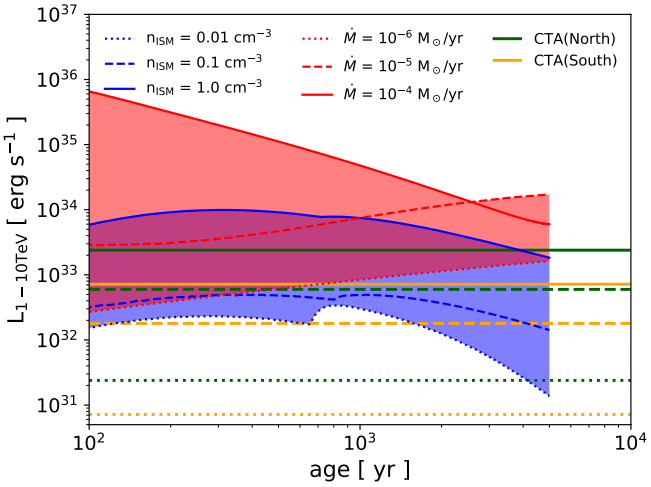

FIGURE 2.13: TeV luminosity as a function of time from our models compared with CTA sensitivities assuming different SNR distances. The green (yellow) lines show the sensitivities of CTA at the north (south) site for a source distance of 1.0 (dotted), 5.0 (dashed) and 10.0 (solid) kpc.

in the 20 GeV to 100 TeV energy range. With CTA, we expect that the number of detected γ-ray emitting SNRs will increase by roughly a factor of 10, which is essential for understanding the SNR population and their ambient environments.

Here, we compare the calculated TeV luminosity from our Ia and CC SNR models with the CTA sensitivities to predict the horizons for SNRs residing in different types of ambient environments. Fig. 2.13 shows the range of model TeV luminosity and CTA sensitivities for different source distances. These sensitivities are calculated using the differential sensitivity curve assuming an observation time of 50 h (see, for details, http://www.cta-observatory.org/science/cta-performance/ (version prod3b-v1)). We do not consider the possibility of source confusion, (fore-)background contamination, and other complications for simplicity.

For SNRs with $d_{\rm SNR} = 1.0$ kpc, we see that, within the parameter range of our models, they are easily detectable regardless of age or ambient environment. For $d_{\rm SNR} = 5.0$ kpc, the detectability starts to depend on the SN type, age and environment. For both the southern and northern sky, the CC SNRs should be observable irrespective of age and environment. The Ia's are also detectable except for those in the southern sky with $t_{\rm age} \geq 2000$ yr interacting with a very tenuous $n_{\rm ISM} \sim 0.01$ cm^{-3} environment, or those in the northern sky with a density $n_{\rm ISM} \leq 0.1$cm^{-3}. For $d_{\rm SNR} = 10.0$ kpc,

the sensitivity for the southern sky is roughly the same as that of the northern sky for $d_{\rm SNR} = 5.0$ kpc. SNRs in the northern sky can be detected if the environment is dense, with $n_{\rm ISM} \sim 1.0$ cm^{-3} for an Ia in a uniform ISM or $\dot{M} \geq 10^{-5}\ M_\odot$/yr for a CC in a wind. So, let $n_{\rm ISM} = 0.1$ cm^{-3} and $\dot{M} = 10^{-5}\ M_\odot$/yr to be the typical values for an ISM-like and a power-law CSM-like environments, respectively, we can conclude that the CTA has a sufficient sensitivity to observe most Type Ia SNRs with $d_{\rm SNR} \leq 5.0$ kpc and CC SNRs with $d_{\rm SNR} \leq 10.0$ kpc and younger than 5000 yr, provided that they have a particle acceleration efficiency similar to Tycho and RX J1713. These results are encouraging in that the number of the SNRs whose VHE emission will be detected at a distance $d_{\rm SNR} \leq 5.0$ kpc will dramatically increase in the CTA era.

2.4 Conclusion

In this study, we model the time evolution of SNRs using a hydrodynamical simulation coupling with efficient particle acceleration based on previous works (e.g., Blasi, 2004; Caprioli, Amato, and Blasi, 2010; Caprioli et al., 2010; Lee, Ellison, and Nagataki, 2012a), and investigate how their broadband nonthermal SEDs evolve in various kinds of ambient environments. We prepare three models for the ambient medium, including a uniform ISM-like case for Type Ia SNRs, a power-law CSM from a steady isotropic stellar wind for CC SNRs, and a case with a pre-SN enhanced mass-loss from a massive star that creates a dense confined CSM shell surrounding the ejecta.

In the Ia models with a uniform ISM, while the π^0-decay flux increases with time, IC flux does not vary much with its spectral peak shifting to lower energy as the SNR ages. In the CC models with a simple power-law CSM, while π^0-decay flux decreases with time, the IC contribution increases with time on the contrary. We found that the key aspects that dictate these evolutionary trends are the density distribution of the interaction targets for each emission component, and the rate of energy loss of the electrons due to synchrotron radiation. In our models, since the interaction target is the ambient gas for π^0-decay and the uniform CMB radiation field for IC, the spatial distribution of the ambient gas density is a key to understand the evolution of the γ-ray spectrum, including a possible transition between a leptonic and a hadronic origin at a certain evolutionary stage. Moreover, the accelerated electrons lose their energy via synchrotron radiation due to a highly amplified magnetic field in the uniform ISM cases. Our results are consistent with

the previously proposed picture that the ISM/CSM gas density decide the dominant component of γ-ray emission from a SNR (e.g., Yuan, Liu, and Bi, 2012). In addition, we propose that not only the number density of the ambient environment but also the distribution of magnetic field is also important in understanding the time evolution of VHE emission. In the case of an enhanced mass loss from a massive star progenitor, the production of secondary particles are found to be very efficient in the dense confined CSM shell and contribute importantly to the overall SED. For example, they can dominate the synchrotron radiation after the SNR breaks out from the shell into a tenuous wind.

A comparison between our models and observations show a broad agreement. A dramatic enlargement of the sample size of γ-ray emitting SNRs is anticipated in the CTA era to further constrain the parameter space in our systematic survey of SNR broadband models. CTA will have a sufficient sensitivity to detect VHE emission from most Ia and CC SNRs in various environments with a distance within ~ 5.0 kpc. Future observations by CTA will reveal the detailed morphological and spectral properties of γ-ray emissions from SNRs and make important progress on our understanding of particle acceleration mechanism at astrophysical collisionless shocks.

We note that the current study has only examined several simple models for the ambient environment, which in reality can be much more complicated such as the presence of a cavity, dense shells, clumpy winds and MCs, etc. Our code is designed to be modular which makes it easy for us to expand into a broader parameter space, including more complicated models for the environment. In future work, we will also explore other important physics such as the acceleration of heavier ions, thermal X-ray line emission, radiative shocks and so on.

TABLE 2.1: The SED data references in each wavelength in Fig. 2.1, Fig. 2.2, and Fig. 2.3.

SNR	radio	X-ray	GeV γ-ray	TeV γ-ray
G34.7−0.4			Ackermann et al., 2013 Giuliani et al., 2011	
G111.7−2.1	Artyukh, Vitkevich, and Dagkesamanskii, 1967	Maeda et al., 2009 Wang and Li, 2016	Abdo et al., 2010	Acciari et al., 2010 Sinitsina and Sinitsina, 2015 Ahnen et al., 2017
G120.1+1.4	Kothes et al., 2006	Troja et al., 2014	Giordano et al., 2012 Archambault et al., 2017	Acciari et al., 2011 Archambault et al., 2017
G189.1+3.0			Tavani et al., 2010 Ackermann et al., 2013	Albert et al., 2007 Acciari et al., 2009
G260.4−3.4	Hewitt et al., 2012 Planck Collaboration et al., 2016		Xin et al., 2017	H. E. S. S. Collaboration et al., 2015
G266.2−1.2	Duncan and Green, 2000		Tanaka et al., 2011	H.E.S.S. Collaboration et al., 2018a
G327.6+14.6	Allen, Petre, and Gotthelf, 2001	Bamba et al., 2008	Condon et al., 2017	Acero et al., 2010
G347.3−0.5	Lazendic et al., 2004 Acero et al., 2009	Tanaka et al., 2008	Abdo et al., 2011	Aharonian et al., 2007 Aharonian et al., 2011 H. E. S. S. Collaboration et al., 2018

TABLE 2.2: Model parameters of ejecta and ISM/CSM properties

Model	M_{ej} [$M_\odot$]	n_{ISM} [cm^{-3}]	$\dot{M}$ [$M_\odot$ yr^{-1}]	V_w [km s^{-1}]	$\dot{M}_2$ [$M_\odot$ yr^{-1}]	$V_{w,2}$ [km s^{-1}]	χ_{inj}
A0[5]	1.4	0.3	-	-	-	-	3.6
A1	1.4	0.01	-	-	-	-	3.6
A2	1.4	0.1	-	-	-	-	3.6
A3	1.4	1.0	-	-	-	-	3.6
B0[6]	3.0	-	7.5×10^{-6}	20	-	-	3.75
B1	3.0	-	1.0×10^{-6}	20	-	-	3.75
B2	3.0	-	1.0×10^{-5}	20	-	-	3.75
B3	3.0	-	1.0×10^{-4}	20	-	-	3.75
B4	10.0	-	1.0×10^{-6}	20	-	-	3.75
B5	10.0	-	1.0×10^{-5}	20	-	-	3.75
B6	10.0	-	1.0×10^{-4}	20	-	-	3.75
C[7]	10.0	-	5.0×10^{-6}	15	0.01	1000	3.75

[5] All model A use an exponential profile for the ejecta, $E_{SN} = 10^{51}$ erg, $T_0 = 10^4$ K, $B_0 = 4.0$ μG, and $d_{SNR} = 3.2$ kpc.

[6] All model B use a power-law profile for the ejecta with $n_{pl} = 7$, $E_{SN} = 10^{51}$ erg, $T_0 = 10^4$ K, $\sigma_w = 0.004$, and $d_{SNR} = 1.0$ kpc.

[7] This model uses a power-law profile for the ejecta with $n_{pl} = 7$, $E_{SN} = 10^{51}$ erg, $T_0 = 10^4$ K, $n_{pl,2} = 1.5$, and $d_{SNR} = 1.0$ kpc.

TABLE 2.3: The SNR observation data, radio flux from Green, 2017, GeV flux from Acero et al., 2016, TeV flux from H. E. S. S. Collaboration et al., 2018, and the other data from *SNRcat* (available at "http://www.physics.umanitoba.ca/snr/SNRcat/") and other references

SNR	common name	type[8]	age [yr]	distance [kpc]	radius [deg]	velocity [″/yr]	$F_{1\mathrm{GHz}}$ [Jy]	$F_{1-100\mathrm{GeV}}$[9] [10^{-9} cm^{-2} s^{-1}]	$F_{1-10\mathrm{TeV}}$[10] [10^{-13} cm^{-2} s^{-1}]	references.
G1.9+0.3		Ia	150 - 220	8.5	0.01	0.32±0.02	0.6	0.27	0.72	Carlton et al. (2011), H.E.S.S. Collaboration et al. (2014)
G4.5+6.8	Kepler	Ia	414	2.9 - 4.9	0.03	0.23±0.01	19	0.65	0.12	Aharonian et al. (2008), Vink (2008)
G15.9+0.2		CC	1000 - 3000	8.5	0.05	0.021±0.001	5.0	1.6	2.6	Sasaki et al., 2018
G34.7−0.4	W44	CC	7900 - 8900	2.7 - 3.3	0.31 ± 0.02	0.047	240	54.95 ± 2.68	11.2	Uchida et al., 2012, Ackermann et al., 2013
G43.3−0.2	W49B	CC	2900 - 6000	10.9 - 11.7	0.07	0.022	38	19.24 ± 1.01	-	Keohane et al., 2007, Zhu, Tian, and Zuo, 2014
G67.7+1.8		CC	5000 - 13000	7.0 - 17.0	0.11	-	1.0	0.43	15.3	Hui and Becker, 2009
G111.7−2.1	Cas A	CC	316 - 352	3.3 - 3.7	0.041 ± 0.001	0.31 ± 0.02	2400	6.25 ± 0.42	5.8 ± 1.2	DeLaney and Rudnick, 2003
G120.1+1.4	Tycho, SN1572	Ia	446	2.4 - 5.0	0.07	0.30 ± 0.10	56	1.06 ± 0.33	1.1 ± 0.4	Katsuda et al., 2010, Giordano et al., 2012
G189.1+3.0	IC443, Jellyfish Nebula	CC	3000 - 30000	0.7 - 2.0	0.33 ± 0.01	0.012	165	57.27 ± 1.15	-	Ackermann et al., 2013, Ambrocio-Cruz et al., 2017
G260.4−3.4	Puppis A	CC	3700 - 4500	1.3 - 2.2	0.33 ± 0.02	0.13	130	8.04 ± 0.56	-	Reynoso, Cichowolski, and Walsh, 2017
G266.2−1.2	Vela Jr, RX J0852.0-4622	CC	2400 - 5100	0.5 - 1.0	1.19 ± 0.04	0.35 ± 0.13	50	12.11 ± 0.89	200 ± 6.58	Allen et al., 2015, H.E.S.S. Collaboration et al., 2018a
G272.2−3.2		Ia	3600 - 11000	2.0 - 10.0	0.12	0.036	0.4	1.2	5.6	Sánchez-Ayaso et al., 2013
G291.0−0.1		CC	1300 - 10000	3.5 - 6.0	0.23	-	16	13.04 ± 0.78	4.9	Roger et al., 1986
G292.0+1.8		CC	2930 - 3050	6.0	0.2	0.043	15	6.17 ± 0.43	3.2	Gaensler and Wallace, 2003, Gonzalez and Safi-Harb, 2003
G296.1−0.5		CC	2800 - 28000	2.0 - 4.0	0.25	0.040±0.003	8	2.0	3.6	Gök and Sezer, 2012
G306.3−0.9		Ia	1300 - 4600	8.0	0.02	0.018±0.001	0.16	1.1	1.1	Reynolds et al., 2013, Sezer, Ergin, and Yamazaki, 2017
G308.4−1.4		CC	5000 - 7500	9.1 - 10.7	0.07	0.016±0.004	0.4	0.58	3.5	Prinz and Becker, 2012
G309.2−0.6		CC	700 - 4000	2.0 - 6.0	0.11	-	7	0.96	3.8	Rakowski, Hughes, and Slane, 2001
G315.4−2.3	RCW86	Ia	2000 - 10000	2.3 - 3.2	0.35	0.13±0.06	49	34	18.2 ± 9.4	Helder et al., 2013, H.E.S.S. Collaboration et al., 2018b
G327.6+14.6	SN1006	Ia	1012	1.6 - 2.2	0.25	0.29	19	0.72	3.7 ± 0.8	Nikolić et al., 2013, Condon et al., 2017
G330.2+1.0		CC	1000 - 3000	≥5.0	0.08	0.20	5	0.64	7.3	H.E.S.S. Collaboration et al., 2014, Williams et al., 2018
G347.3−0.5	RX J1713.7-3946	CC	1625	1.0	0.53 ± 0.03	0.82 ± 0.06	30	4.94 ± 0.81	146 ± 6	Tsuji and Uchiyama, 2016, H. E. S. S. Collaboration et al., 2018
G350.1−0.3		CC	600 - 1200	4.5 - 9.0	0.03	0.11±0.03	6	3.3	1.6	Lovchinsky et al., 2011

[8]type of SN explosion, 'Ia' implies thermonuclear explosion and 'CC' implies core-collapse SN. About the SNRs whose explosion type is not known much, it is assumed to be 'CC' in this table.

[9]the integrated flux by *Fermi*-LAT in 1-100 GeV range, but those without error are the 99 % confidence upper limit with photon index $\Gamma = 2.5$ because the SNR is not observed by *Fermi*-LAT, see Acero et al., 2016 for details.

[10]the integral flux by H.E.S.S. in 1-10 TeV range, that with error is the detected value and that without error is the upper limit of 99 % confidence level with $\Gamma = 2.3$.

Chapter 3

Dark Age of Type II Supernova Remnants

Part of this chapter was published as Yasuda, Lee, & Maeda 2021, ApJL, 919, L16.

3.1 Scope of this chapter

Supernovae (SNe) are one of the most energetic phenomena in the Universe in which stars explode and release a tremendous amount of energy at the final stage of stellar evolution. Type II SNe are known to be coming from the death of massive stars in their final evolutionary stage such as red supergiants (RSG) (Smartt, 2015). Electromagnetic radiation from SNe provides information about their progenitors and surrounding environments, which are crucial in understanding stellar evolution and mass loss history of massive stars (Filippenko, 1997). However, SN observations are usually limited to a timescale of an order of weeks to years, which means that we can only extract the mass loss history shortly before explosion. On the other hand, observations of their supernova remnants (SNRs) interacting with their CSM environments are an effective supplementary tool for probing mass loss at earlier phases well before core collapse.

Young and dynamically active SNRs are usually observable in multiwavelength from radio to TeV-γ rays, indicating that SNRs are in-situ acceleration sites of relativistic particles, which are widely believed to be closely linked to the origin of Galactic cosmic rays (CRs) accelerated at the SNR shock fronts through the diffusive shock acceleration (DSA) mechanism (Fermi, 1949; Bell, 1978a; Blandford and Ostriker, 1978). The non-thermal emissions are mostly produced by the interactions between the accelerated CRs and the surrounding interstellar medium (ISM) and circumstellar medium (CSM). They therefore hold the key to understanding the ambient environments in which SNe explode. Yasuda and Lee, 2019 (hereafter YL19) calculated the evolution of

young SNRs and the accompanying non-thermal emissions in various environments until 5000 yr, and they found that the spectral energy distribution (SED) of the broadband emission varies with time in a way strongly correlated with the density and spatial structure of the surrounding ISM/CSM gas and magnetic field. However, they used very simplified models for the environments by assuming simple power-law distributions extended to infinity for the CSM density for example, without considering the mass loss history and stellar evolution of the progenitor stars. A systematic calculation linking the progenitors, SNe and SNRs, especially with the mass loss history taken into account, is therefore on high demand for facilitating the usage of SNR observations for diagnosing SN types, mass loss mechanism and progenitor natures.

In this chapter, we first prepare realistic CSM models using one-dimensional hydrodynamic simulations considering the mass-loss history of a Type II SN progenitor. Using another set of hydrodynamical simulations coupled with efficient particle acceleration, we then compute the time evolution of SNR dynamics and non-thermal emissions in such CSM environments up until an age of 10^4 yrs. In section. 3.2, we introduce our numerical method for the hydrodynamics and particle acceleration for SNR evolution, and for the generation of reasonable CSM models based on SN observations. Section. 3.3 shows our results on the non-thermal emissions from SNRs assuming different progenitor masses and stellar wind properties, and their comparisons to the currently available observation data. Discussions and conclusion are summarized in Section. 3.4 and Section. 3.5

3.2 Method

3.2.1 Hydrodynamics

The hydrodynamics code used in this work is in a large part identical to the *CR-Hydro* code developed in YL19 except for a few differences which we will overview in the following. The hydrodynamic calculations are based on the *VH-1* code (e.g., Blondin and Ellison, 2001) which solves multi-dimensional Lagrangian hydrodynamic equations. As introduced in YL19, we modified the code to include feedback from CR acceleration, and assumed a spherical symmetry for simplicity;

$$\frac{\partial r}{\partial m} + \frac{1}{4\pi r^2 \rho} = 0 \tag{3.1}$$

$$\frac{\partial u}{\partial t} + \frac{\partial P_{\rm tot}}{\partial m} = 0 \tag{3.2}$$

$$\frac{\partial e}{\partial t} + \frac{\partial}{\partial m}(P_{\rm tot} u) = -n^2 \Lambda_{\rm cool} \tag{3.3}$$

$$e = \frac{1}{2}u^2 + \frac{P_{\rm tot}}{(\gamma_{\rm eff} - 1)\rho}, \tag{3.4}$$

where ρ, n, m, u and e are the gas mass density, number density, mass coordinate, fluid velocity and internal energy density, respectively. We treat the gas and accelerated CRs in an one-fluid description by employing an effective gamma $\gamma_{\rm eff}$ for the equation-of-state (e.g., Chevalier, 1983; Blondin and Ellison, 2001), and a total pressure defined as $P_{\rm tot} = P_{\rm g} + P_{\rm CR} + P_{\rm B}$, where $P_{\rm g}$, $P_{\rm CR}$ and $P_{\rm B}$ are gas pressure, CR pressure and magnetic pressure, respectively. Since *VH-1* is not a magnetohydrodynamics (MHD) code, we provide an additional treatment for the time evolution of the post-shock magnetic field strength. Ignoring effects such as amplification by MHD turbulence, the magnetic field strength follows the conservation of magnetic flux $B \propto r^{-2}$ along with the advection of the downstream gas. Combined with the mass conservation $\rho \propto r^{-2}$, we can obtain $B \propto \rho$. As in YL19, the magnetic field also receives an amplification by CR-streaming instability in the shock precursor which is calculated self-consistently with the particle acceleration. The temperatures of protons T_p and electrons T_e are equilibrated by their post-shock Coulomb collisions. To allow for the calculation of late-phase SNR evolution, especially in a high-density medium which YL19 did not consider, we implement optically thin radiative cooling as well in this work using an exact integration scheme (Townsend, 2009). A non-equilibrium ionization cooling curve from Sutherland and Dopita, 1993 is used for the cooling function $\Lambda_{\rm cool}$.

3.2.2 Cosmic-ray spectrum

The phase-space distribution function of the accelerated protons, $f_p(x, p)$, can be obtained by solving the following diffusion-convection equation written in the shock rest frame (e.g., Caprioli, Amato, and Blasi, 2010; Caprioli et al., 2010; Lee, Ellison, and Nagataki, 2012a) assuming a steady-state and isotropic distribution in momentum space,

$$\begin{aligned}&[u(x) - v_A(x)]\frac{\partial f_p(x,p)}{\partial x} - \frac{\partial}{\partial x}\left[D(x,p)\frac{\partial f_p(x,p)}{\partial x}\right] \\ &= \frac{p}{3}\frac{d[u(x) - v_A(x)]}{dx}\frac{\partial f_p(x,p)}{\partial p} + Q_p(x,p),\end{aligned} \tag{3.5}$$

where $D(x,p)$, $v_A(x)$ and $Q_p(x,p)$ is the spatial diffusion coefficient, Alfvén speed and proton injection rate at position x in the shock rest frame. We assume a Bohm diffusion, such that $D(x,p) = pc^2/3eB(x)$, where $B(x)$ is the local magnetic field strength at position x. We adopt the so-called 'thermal-leakage' injection model (Blasi, 2004; Blasi, Gabici, and Vannoni, 2005) for the DSA injection rate $Q_p(x,p)$ such that

$$Q_p(x,p) = \eta \frac{n_1 u_1}{4\pi p_{\rm inj}^2} \delta(x)\delta(p - p_{\rm inj}), \tag{3.6}$$

where n_1 is the number density of proton at immediately upstream of the shock and $p_{\rm inj}$ is the CR injection momentum, which is defined as $p_{\rm inj} = \chi_{\rm inj}\sqrt{2m_p k_{\rm b} T_p}$, where m_p, $k_{\rm B}$ and T_p are the proton mass, Boltzmann constant and temperature respectively. $\chi_{\rm inj}$ and η are free parameters in this work, which control the fraction of thermal particles injected into the DSA process as described in YL19.

Here, we solve eq. (3.5) at the shock position $x = 0$ so that the distribution function can be written in an implicit form with an exponential cutoff (Blasi, 2004; Blasi, Gabici, and Vannoni, 2005);

$$\begin{aligned} f_p(x=0,p) &= \frac{\eta n_0}{4\pi p_{\rm inj}^3} \frac{3S_{\rm tot}}{S_{\rm tot}U(p) - 1} \\ &\quad \times \exp\left(- \int_{p_{\rm inj}}^{p} \frac{dp'}{p'} \frac{3S_{\rm tot}U(p')}{S_{\rm tot}U(p') - 1} \right) \\ &\quad \times \exp\left[- \left(\frac{p}{p_{\rm max,p}} \right)^{\alpha_{\rm cut}} \right], \end{aligned} \tag{3.7}$$

where $S_{\rm tot}$ and $U(p)$ are the effective compression ratio and normalized fluid velocity, respectively. The explicit expressions of these quantities are easily obtained by referring to Caprioli, Amato, and Blasi, 2010 and Lee, Ellison, and Nagataki, 2012a. $\alpha_{\rm cut}$ is introduced because of a poor understanding of the escape process of CRs, which is directly related to the CR spectral shape beyond the maximum momentum $p_{\rm max,p}$.

For the electron spectrum, we use a parametric treatment where the electron distribution function is given as $f_e(x,p) = K_{ep} f_p(x,p) \exp[-(p/p_{\rm max,e})^{\alpha_{\rm cut}}]$. K_{ep} typically takes a value between 10^{-3} and 10^{-2} based on constraints from SNR observations. The determination of the maximum momenta of each particle species is the same as in YL19.

The particles accelerated at the shock are assumed to be co-moving with the gas flow and suffer from energy loss through non-thermal radiations and

adiabatic loss. For the non-thermal radiation mechanisms, we consider synchrotron radiation, inverse Compton scattering (IC), bremsstrahlung from the accelerated electrons, and pion productions by proton-proton interaction (π^0 decay) by the accelerated protons.

3.2.3 Circumstellar medium and SN ejecta

In this study, we first prepare models for the circumstellar medium (CSM) of a Type II SNR by accounting for stellar evolution and mass loss histories of the SN progenitor. The CSM models are generated by performing hydrodynamic simulations in which stellar winds run into a uniform ISM region. The results are used as the initial conditions for the subsequent calculation for the evolution of the SNR.

The progenitor of a Type II SN is believed to be massive OB stars with zero-age main sequence (ZAMS) mass $\geq 10 M_\odot$. This type of stars evolves to red supergiants (RSG) after their main sequence (MS) phase, and explodes via core collapse of their iron cores. Although the mass loss mechanism is not well understood and is still under discussion, it is thought that the star loses its mass from its envelope mainly in the form of stellar wind. The wind blown in MS phase is thin and fast from the compact OB stars, and the total amount of mass lost in the MS phase is relatively small. On the contrary, the star loses most of its mass in the RSG phase through a denser and slower wind. The typical values for the mass loss rate $\dot{M}_{\rm w}$, wind velocity $V_{\rm w}$ and time duration $\tau_{\rm phase}$ in each phase are, $\dot{M}_{\rm w} \sim 10^{-8} - 10^{-7}\ M_\odot/{\rm yr}$, $V_{\rm w} \sim 1 - 3 \times 10^3$ km/s and $\tau_{\rm phase} \sim 10^6 - 10^7$ yr for the MS phase, and $\dot{M}_{\rm w} \sim 10^{-6} - 10^{-5}\ M_\odot/{\rm yr}$, $V_{\rm w} \sim 10 - 20$ km/s and $\tau_{\rm phase} \sim 10^5 - 10^6$ yr for the RSG phase. The relation between the ZAMS mass and pre-SN mass of the progenitor has been investigated (e.g., Kasen and Woosley, 2009; Sukhbold and Woosley, 2014; Woosley and Heger, 2015; Sukhbold et al., 2016), so the mass lost through the MS and RSG winds, and the ejecta mass $M_{\rm ej}$ can be determined if the ZAMS mass is fixed. In this study, we consider two cases for the ZAMS mass, i.e., a $12 M_\odot$ (model A) and $18 M_\odot$ (model B) progenitor star. We also use a time-independent, constant mass loss rate and wind velocity during each phase for simplicity. The exact values used in the models are summarized in Table. 3.1.

When these progenitors explode, the stellar debris propagates outward as a SN ejecta, but some of it falls back onto the stellar core which forms a neutron star. The ejecta mass is calculated as $M_{\rm ej} = M_{\rm ZAMS} - \sum(\dot{M}_{\rm w}\tau_{\rm phase}) -$

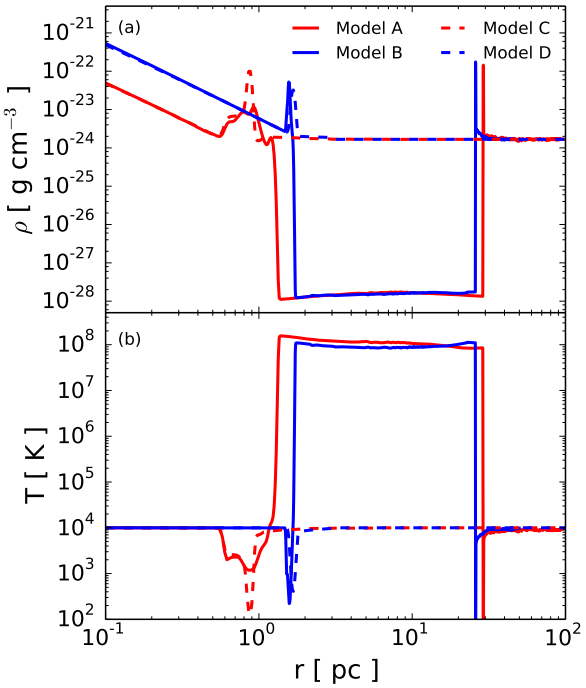

FIGURE 3.1: CSM models for a Type II SNR. The upper panel shows the gas density as a function of radius, and the lower panel shows the average gas temperature. The red (blue) solid line corresponds to the low (high) progenitor mass case. The dashed lines show the results from models in which the MS bubble does not exist for comparison.

$M_{\rm rm}$, where $M_{\rm rm}$ is the stellar remnant mass after explosion. In the ZAMS mass range we consider in this work, $M_{\rm rm}$ is typically $1.4 \sim 1.7\ M_\odot$ (Woosley and Heger, 2007; Sukhbold et al., 2016; Woosley, Sukhbold, and Janka, 2020). $M_{\rm rm} = 1.5\ M_\odot$ is adopted in all models here. For the SN ejecta structure, we assume a power-law envelope model in Truelove and McKee (1999) for all of our models;

$$\rho(r) = \begin{cases} \rho_{\rm c} & (r \leq r_{\rm c}) \\ \rho_{\rm c}(r/r_{\rm ej})^{-n_{\rm SN}} & (r_{\rm c} \leq r \leq r_{\rm ej}), \end{cases} \tag{3.8}$$

where $\rho_{\rm c}$, $r_{\rm c}$ and $r_{\rm ej}$ are the core density, core radius and ejecta size, respectively. These values are uniquely determined by mass and energy conservation. The related parameters are, therefore, the ejecta mass $M_{\rm ej}$, the kinetic energy of the explosion $E_{\rm SN}$, and the power-law index of the envelope $n_{\rm SN}$. We assume $E_{\rm SN} = 1.2 \times 10^{51}$ erg and $n_{\rm SN} = 7$. The ejecta masses depend on the ZAMS masses in each model, and are summarized in Table. 3.1.

Figure. 3.1 shows the density and temperature structures provided by our stellar wind simulations. The upper panel (a) shows the radial density distribution of the CSM created by the stellar wind from a Type II SN progenitor.

TABLE 3.1: The wind parameters and ejecta properties for a Type II SNR. The wind temperature is set to be $T = 10^4$ K, SN explosion energy $E_{SN} = 1.2 \times 10^{51}$ erg, power-law index of the ejecta envelope $n_{ej} = 7$, and stellar remnant mass $M_{rm} = 1.5 M_\odot$ (Woosley and Heger, 2007; Sukhbold et al., 2016; Woosley, Sukhbold, and Janka, 2020) in all models. We also assume $n = 1.0$ cm^{-3} and $T = 10^4$ K for the outer ISM region.

Model	M_{ZAMS} $[M_\odot]$	Phase	$\dot{M}$ $[M_\odot$ yr$^{-1}]$	V_w [km s^{-1}]	M_w $[M_\odot]$	τ_w yr	M_{ej} $[M_\odot]$
A	12	MS	5.0×10^{-8}	2000	0.5	10^7	
		RSG	1.0×10^{-6}	10	0.5	5.0×10^5	9.5
B	18	MS	6.0×10^{-8}	2000	0.3	5.0×10^6	
		RSG	1.0×10^{-5}	10	2.7	2.7×10^5	13.5
C	12	RSG	1.0×10^{-6}	10	1.0	10^6	9.5
D	18	RSG	1.0×10^{-5}	10	3.0	3.0×10^5	13.5

The red and blue solid lines correspond to the results of the 12 $M_\odot$ (model A) and 18 $M_\odot$ (model B) cases, respectively. The dashed lines represent the models in which mass loss in the MS phase is not considered for comparison (model C and D). The lower panel (b) shows the gas temperature as a function of radius. In the stellar wind simulations, the winds are assumed to be blown into a uniform ISM with $n_{ISM} = 1.0$ cm^{-3} and $T = 10^4$ K in all of our models.

From the solid lines in panels (a) and (b), we can see that the CSM structure can be divided into 5 characteristic regions from the outer to inner radius; (i) uniform ISM, (ii) MS shell, (iii) MS bubble, (iv) RSG shell, and (v) RSG wind. Because the MS wind has a low density and high velocity, and it is blown over a relatively long time period, the MS wind sweeps up the ISM and forms a dense cold shell between the ISM and the MS bubble at $r \sim 30$ pc. The swept ISM mass is $M = (4\pi/3) r^3 m_p n_{ISM} \sim 2700\, M_\odot (r/30\,\mathrm{pc})^3 (n_{ISM}/1\,\mathrm{cm}^{-3})$, which is much larger than the total mass inside the MS wind $\sim 0.5\, M_\odot$. A termination shock is formed and heats the MS wind up to a high temperature. As a result, the environment is characterized by a tenuous ($n \sim 10^{-4}$ cm^{-3}) and hot ($T \sim 10^8$ K) plasma as a "MS bubble". After that, the RSG wind sweeps up the thin gas inside the bubble, and a RSG wind shell is formed at the outer edge of the wind at $r \sim 1$ pc.

The differences between models A and B are mainly in the locations of the MS shell and RSG shell. They are attributed to the slight differences in the mass loss rates and time duration of the mass loss phases mainly determined by the mechanical balance between the ram pressure of the winds and the

thermal pressure of the external gas. On the other hand, while model C and D do not include mass loss in the MS phase intentionally, the RSG shells locate at more-or-less the same radius as models A and B because the thermal pressures in the ISM and the MS bubble are almost the same. In overall, the major difference between models A and B (solid lines) and models C and D (dashed lines) lies in the (non-)existence of the MS bubble and MS shell.

The results from the stellar wind simulations above are used as the initial conditions for our subsequent calculations for the evolution of the SNR. We further define the local magnetic field strength in the CSM environment as $B(r) = \sqrt{8\pi n(r) k_{\rm B} T(r)/\beta}$, where β is the plasma beta $\beta \equiv P_{\rm g}/P_{\rm B}$. From observations of SNe and SNRs, β is typically ≥ 100 inside a wind, and ~ 1 in the ISM close to equi-partition. In this study, β and the other free parameters mentioned above are obtained by fitting to the observation of SNR RX J1713.7-3946 as in YL19, i.e., $\beta \sim 825$ for the unshocked wind and wind shells, and $\beta \sim 2.17$ for the ISM region, which correspond to magnetic field strengths $B \sim 0.3$ μG in the wind region (at $r \sim 1$ pc) and $B \sim 4.0$ μG in the ISM region (at $r \geq 10$ pc). The other parameters such as $\chi_{\rm inj}$ and $\alpha_{\rm cut}$ are the same as in Model B in YL19.

3.3 Results

In the SNR simulations, we compute the hydrodynamical evolution of a Type II SNR up to an age of 10^4 yr, and the non-thermal emissions resulted from its interaction with the environment models provided by the wind simulations as described in the previous section.

Figure. 3.2 shows the time evolution of the SNR radius $R_{\rm sk}$ (upper panel) and shock velocity $V_{\rm sk}$ (lower panel) for each of our models. As a reference, we also plot the results of two fiducial models from YL19[1] (see their models A2 and B2), i.e., a model with a uniform ISM-like environment with $n_{\rm ISM} = 0.1$ cm^{-3} (hereafter, "Type Ia" case) and another with a power-law CSM extended to an infinite radius with $\dot{M} = 10^{-5}\ M_\odot/{\rm yr}$ (hereafter, "continuous power-law" case). Observational data from a selection of γ-ray bright SNRs are also plotted with blue points for Type Ia SNRs and red points for core collapse SNRs. They are sorted with numbers and the corresponding

[1] As the SN ejecta, an exponential profile $\rho(r) \propto \exp(-r/r_{\rm ej})$ for Type Ia case (Dwarkadas and Chevalier, 1998) was assumed. For continuous power-law model, a power-law envelope model was used with the same eqn. (3.8). The ejecta mass and kinetic energy of each case were 1.4 $M_\odot$ and 10^{51} erg for Type Ia case, and 3.0 $M_\odot$ and 10^{51} erg for power-law case. $n_{\rm SN} = 7$ was also assumed in the latter model.

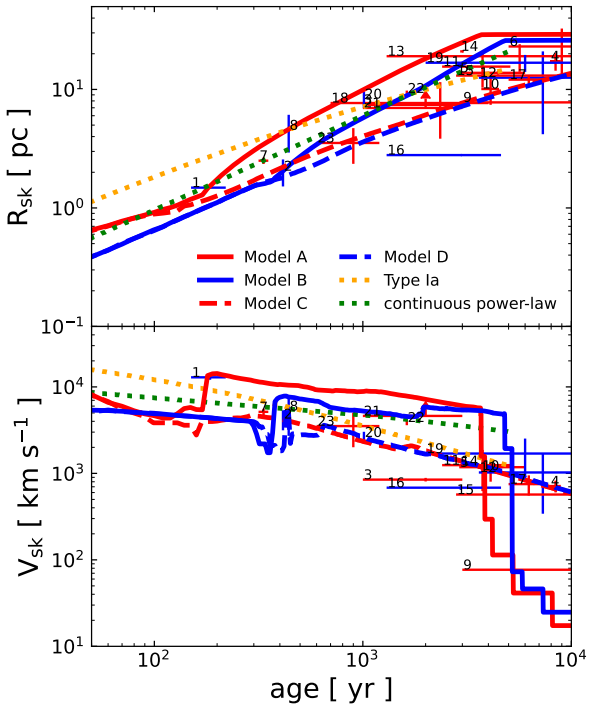

FIGURE 3.2: The hydrodynamical evolution of a Type II SNR. Upper panel shows the forward shock radius as a function of SNR age, and the lower panel shows the evolution of the shock velocity. The line formats are the same as Figure. 3.1. The dotted lines are taken from Model A2 (orange) and B2 (green) in YL19 for comparison (see text). Actual observation data from γ-ray bright SNRs are overlaid, for which the references can be found in YL19.

table is summarized in Fig. 11 in YL19. The details and references for the observational data can again be found in YL19.

We first look at the results from model D (blue dashed line) which has the most straightforward evolution behavior. In the early phase with $t \leq 300$ yr, the SNR shock is propagating inside the RSG wind, and the time evolution is similar to the continuous power-law case except that the absolute values are slightly different because parameter values such as the ejecta mass are not the same. As the SNR continues to expand, it collides with the RSG shell and results in a small deceleration of the shock. The deceleration is not significant because the mass inside the RSG shell is much smaller than the ejecta mass. Finally, the SNR expands into the uniform ISM region and eventually sweeps up an amount of ISM material more massive than the ejecta, and the SNR enters the self-similar Sedov phase. During this phase, the shock radius and velocity depend only on the SN explosion energy, ISM gas density and age, therefore model D shows a similar behavior to the Type Ia case after $t \geq$

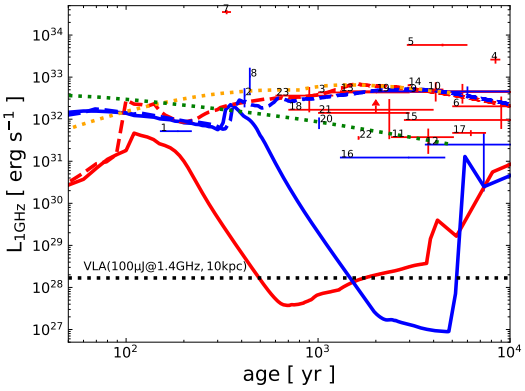

(a)

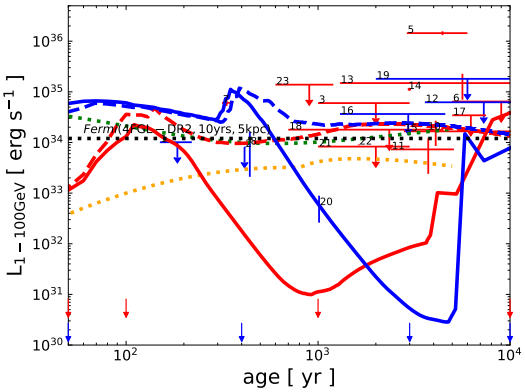

(b)

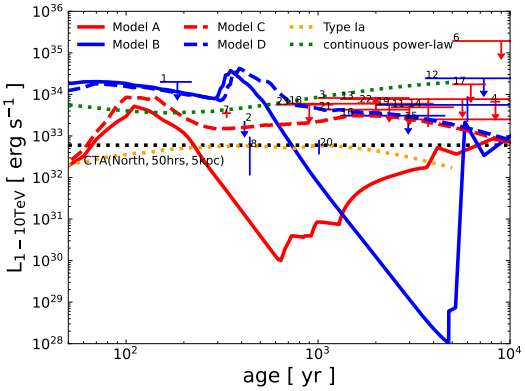

(c)

FIGURE 3.3: Light curves of the 1 GHz radio continuum (left panel (a)), γ-ray integrated over the 1-100 GeV band (middle panel (b)) and 1-10 TeV band (right panel(c)). The line formats are the same as in Fig. 3.2. In panel (a), (b) and (c), the detection limit of VLA, *Fermi*-LAT and CTA are plotted with black lines, respectively. Results from multi-wavelength observations of selected SNRs as shown in Fig. 3.2 are also overlaid.

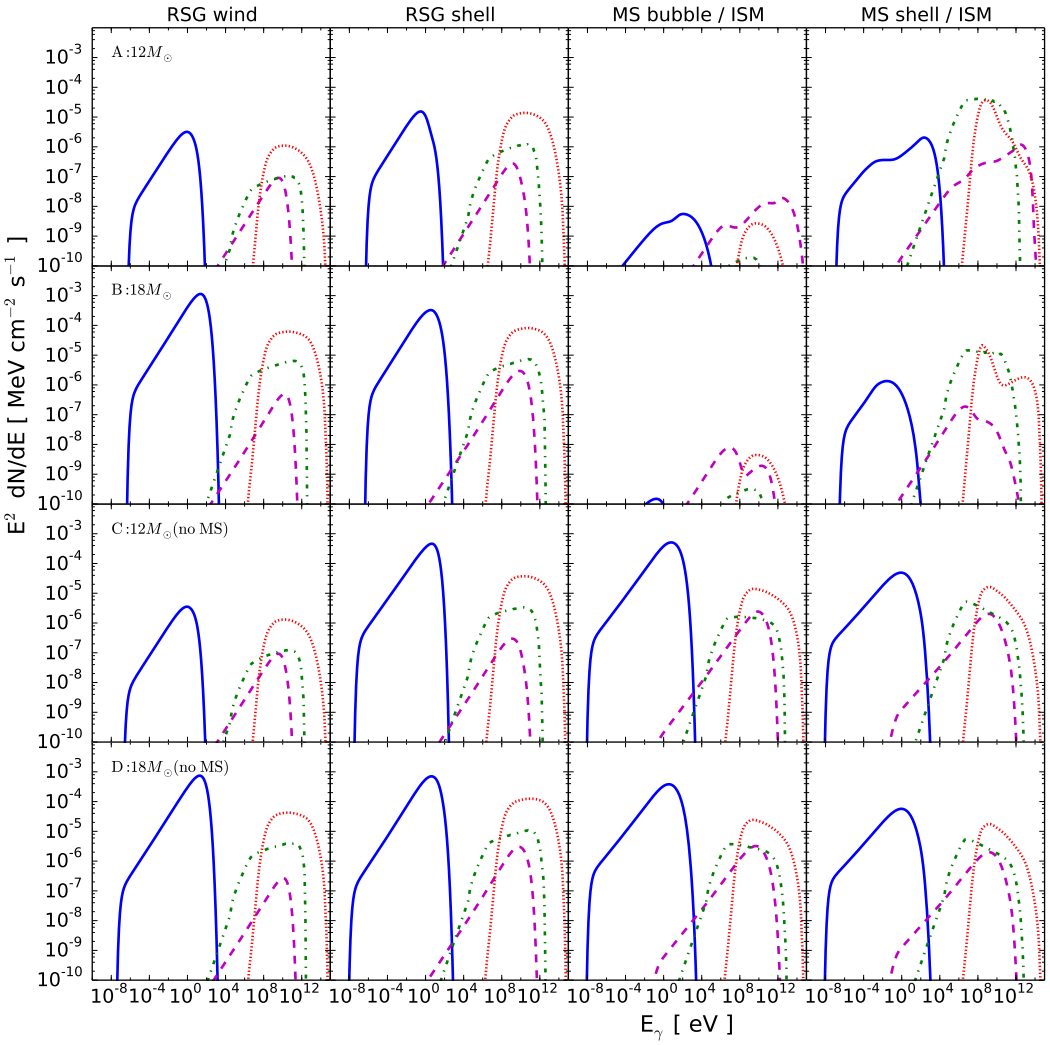

FIGURE 3.4: Broadband SED from a Type II SNR with different progenitor masses and CSM models (top to bottom) and at different ages (left to right). The exact ages for each of the four panels from left to right are characterized by the location of the forward shock in different regions of the CSM environment, and are showed in panel (b) of Fig. 3.3 with red arrows for model A and C, and blue arrows for model B and D. The emission components include synchrotron (blue solid), π^0 decay (red dotted), IC (magenta dashed), and non-thermal bremsstrahlung (green dot-dashed).

3,000 yr. For model C (red dashed line), the shock decelerates at an earlier time than model D because the RSG shell is located at a smaller radius than in model D for the reasons already explained in section. 3.2.3. Otherwise, the general evolution is qualitatively similar to model D.

Model B follows the same evolution trend as model D until the shock hits the RSG shell. The shock breaks out from the RSG shell into a tenuous MS bubble, so that the shock accelerates and the expansion of the SNR speeds

up. Afterwards, the shock collides with a dense cold shell at the outer edge of the MS bubble, and rapidly decelerates to $V_{\rm sk} \sim 10$ km/s. The expansion of the SNR then slows down drastically and the SNR size stays more-or-less unchanged. The evolution shown by model A is qualitative similar to model B except for differences in timing simply due to the different locations of the MS bubble.

Figure. 3.3 shows the light curves for the 1 GHz radio continuum (left panel (a)), GeV γ-rays in the 1-100 GeV band (middle panel (b)), and TeV γ-rays in the 1-10 TeV band (right panel (c)). The color and line formats are the same as Fig. 3.2. From left to right, Figure. 3.4 shows the spectral energy distribution (SED) from each model at four chosen characteristic ages as indicated by the arrows in panel (b) of Fig. 3.3 (red arrows for models A and C with $M_{\rm ZAMS} = 12M_{\odot}$, and blue arrows for models B and D with $M_{\rm ZAMS} = 18M_{\odot}$).

The light curves from model D behave similarly in all wavelengths to the continuous power-law case at early times ($t \leq 300$ yr) and to the Type Ia case at larger ages ($t \geq 3000$ yr) which is in accordance with the hydrodynamical evolution. At early times, the γ-rays are dominated by the hadronic component from π^0 decay because of the high gas density in the RSG wind, and suffer from strong adiabatic loss due to the inverse power-law distribution of the CSM as r^{-2}. As a result, the γ-ray luminosity decrease with time. The shock expands into the uniform ISM later on, and the γ-rays stay dominated by the π^0 decay channel. The spectral power-law index of the accelerated proton and hence the γ-ray spectrum becomes steeper however due to shock deceleration in the ISM and an increased influence from the Alfvén velocity on the non-linear DSA process as the SNR enters its Sedov phase (see the rightmost panel in Fig. 3.4), and the γ-ray luminosity decreases accordingly in particular for the TeV band. These evolution behaviors are found to be similar to the results in YL19. At intermediate ages ($300 \leq t \leq 3000$ yr), the SNR hits the RSG shell, and the emissions brighten briefly for about 200 yrs before the light curves gradually converge back to those similar to the Type Ia case. In model C, the SNR collides with the RSG shell at an earlier age of 60 yrs and brightens from 100 to 200 yrs, but otherwise shows similar behavior to model D after an age of 2000 yrs.

Of the biggest interest and surprise are the results from model B. Up until the collision of the SNR with the RSG shell ($t \leq 500$ yr), the light curves basically follow the same evolution as model D. After the collision, however,

the radio and γ-ray luminosities rapidly decrease to a point that they are undetectable by current observational instruments. We can interpret this rapid dimming based on two reasons. First, as the SNR shock enters the tenuous and hot MS bubble region, it becomes difficult for the shock to accelerate particles through DSA because injection becomes inefficient due to the low density of the ambient gas $n \sim 10^{-4}$ cm^{-3}, and the shock sonic Mach number M_s decreases drastically due to the high temperature $T \sim 10^8$ K in the bubble, namely $M_s = V_{\rm sk}/C_s \sim 5\ (V_{\rm sk}/5 \times 10^3\ {\rm km/s})(T/10^8\ {\rm K})^{-1/2}$, where C_s is the local sound speed. Second, the SNR expands rapidly while the shock is inside the MS bubble. The particles accelerated earlier on in the RSG wind suffer from fast adiabatic loss from the rapid expansion, and the luminosities drop down by at least three orders of magnitudes. These results can also be observed from the SEDs in the third column in Fig. 3.4. After the SNR shock has propagated through the bubble and eventually hit the cold dense shell at the edge, the shock starts to sweep up the dense material in the shell and the non-thermal emissions are then enhanced from the increased gas density. The SNR brightens again enough to be observable by currently available detectors, as will be discussed in more details below.

The SNR shock is interacting with the MS shell at an age of 10,000 yr (Fig. 3.2). After that, it is expected that the shock will break out from the shell and propagate into the uniform ISM region. In this phase, the shock velocity should have decelerated to a velocity too low to accelerate new particles efficiently in the ISM, and the luminosities will decrease with time due to adiabatic loss. Continuing our simulations beyond 10,000 yrs would allow us to estimate the exact lifespan of the SNR in the radio and γ-ray energy bands, but it is beyond the scope of this work.

Model A shows slightly different results from model B, in particular during the MS bubble phase. The ejecta mass of model A is smaller than model B, and the total mass inside the RSG wind is also about 5 times smaller. This leads to a shock velocity in model A almost 2 times higher than in model B when the shock is inside the MS bubble (Fig. 3.2). As a result, the sonic Mach number is also higher by roughly a factor ~ 2 at $M_s \sim 10$ while inside the MS bubble. This shock can accelerate new particles despite the low gas density inside the bubble, therefore the light curves rise gradually with time from 600 yrs which is different from the behavior shown by model B with a more massive progenitor.

To assess the observational detectability of a Type II SNR based on our models, observation sensitivities in the radio and γ-ray bands are plotted in

panel (a), (b) and (c) in Fig. 3.3 with black dotted lines. We compare the detection limit of the Very Large Array (VLA) with our models for the radio band. Radio galaxies and active galactic nuclei are often observed with a sensitivity $\sim$ 100 μJy at 1.4 GHz (e.g. Schinnerer et al., 2004; Simpson et al., 2012). The lower limit of the radio luminosity from a source at a distance of 10 kpc is therefore $\sim 2 \times 10^{28}$ erg/s. We note that it is a very optimistic limit, since this is the typical sensitivity for a targeted observation. If there is no detection in other wavelength, the radio sensitivity should be lower. We also compare with the sensitivity of the *Fermi* Large Area Telescope (*Fermi*-LAT) for GeV γ-rays. For TeV γ-rays, we use the sensitivity data of the Cherenkov Telescope Array (CTA), the most powerful next-generation ground-based γ-ray telescope expected to start observing the Universe in year 2022 (Cherenkov Telescope Array Consortium et al., 2019). *Fermi*-LAT has a flux sensitivity of $\sim 2 \times 10^{-12}$ erg cm^{-2} s^{-1} in the 1-100 GeV band based on 10 yrs of survey data (see, for details, Abdollahi et al., 2020; Ballet et al., 2020 and https://www.slac.stanford.edu/exp/glast/groups/canda/lat_Performance.htm), which corresponds to a luminosity $\sim 1.2 \times 10^{34}$ erg/s for a γ-ray source at 5 kpc. The detection limit of CTA at 5 kpc is $\sim 6 \times 10^{32}$ erg/s with a flux sensitivity $\sim 10^{-13}$ erg cm^{-2} s^{-1} in the 1-10 TeV band for the northern telescopes and an observation time of 50 hrs (see, for details, https://www.cta-observatory.org/science/ctao-performance/). We do not consider other effects like interstellar absorption and source contamination for simplicity.

Our results show that the γ-rays cannot be observed from 1000 yr to 10^4 yrs for the case with a $18M\odot$ progenitor, and from 300 yr to 10^4 yr for a $12M\odot$ star. In addition, the radio emission also stays faint and barely comparable to the VLA sensitivity limit until 5000 yrs. On the contrary, we can observe Type II SNRs with ages of 5000 yr $\leq t \leq$ 10000 yr but only in the radio. So, we conclude that with the presence of a tenuous hot bubble created by the MS stellar wind, most Type II SNRs experience a "dark age" in which they become too faint to be observable at ages $\sim 1000 - 5000$ yrs, although the span and exact timing can depend on the surrounding environment, mass loss history of individual progenitors and the detection limits of currently available detectors.

3.4 Discussion

We have chosen a few model parameters related to DSA to match our previous model of RX J1713 (see, e.g., Fig.3 inYL19), which showed a good agreement with the bulk properties and the overall broadband spectrum but without considering a collision with molecular clouds. However, the correlation of RX J1713 with molecular clouds has been reported by some recent works (e.g., Fukui et al., 2012; Tanaka et al., 2020), which may necessitate a revision of our model for this particular object in the future. Our results and conclusions in this work are mainly dependent of the bulk dynamics of the SNR shock in its surrounding CSM environment created by the RSG progenitors, which do not rely on any fine-tuning of model parameters mentioned above. Therefore, our results can be considered robust and present two possibilities:

1. If the MS bubbles exist, most Type II SNRs cannot be detected as it enters the bubble, which corresponds to an age of 10^3 - 5×10^3 yr for a RSG progenitor exploded inside a typical ISM,

2. The MS bubbles indeed might not exist or be compact enough so that accelerated particles are not affected too much by adiabatic loss.

If the first scenario is true, all detected core collapse SNRs so far with ages around 1000 to 5000 yrs old are most probably not originated from Type II SNe. Indeed, the total SN rate in our galaxy is almost $1/30$ yr^{-1} (e.g, Adams et al., 2013) so that the number of expected SNRs with an age of 1000 to 5000 yrs should be at least 100. Nevertheless the number of SNRs detected in radio and other wavelengths falling into this age range is only at an order of ten (Green, 2017; Acero et al., 2016; H. E. S. S. Collaboration et al., 2018). Because Type II SNe are expected to produce almost half of the total population of SNRs (e.g. Li et al., 2007), this is consistent with our results that many Type II SNRs actually cannot be detected. On the contrary, our results for cases without the MS bubble show that the SNRs are bright enough to be detected with present detectors. The detection rate should be larger if the MS bubbles do not exist or compact enough to be unimportant. The interpretation therefore depends on the general (non-)existence of MS bubbles around the massive star progenitors.

One related caveat is that we have only considered a simple scenario for stellar evolution in this work. For example, the wind velocity plays an important role for shaping the CSM environment. If the MS stellar wind is slower than what we assumed here, and/or the RSG wind is faster, the MS bubble

is expected to be smaller in size so that the RSG wind can sweep through almost its entirety before core collapse. A smaller mass loss in the MS phase will lead to the same result. From this point of view, type Ib/c SNe are possibly important objects. The progenitors of type Ib/c SNe are thought to be Wolf-Rayet (WR) stars. A WR star is a compact star which has lost its entire hydrogen envelope via stellar wind and/or binary interaction through a phase of Roche-lobe overflow. It ejects a very fast wind with $V_{\rm w} \sim 10^3$ km/s, and this wind can sweep up the MS bubble all the way close to the edge where the dense cold shell sits. This may help their SNRs avoid the strong adiabatic loss of the accelerated particle due to a fast expansion of the remnant in the MS bubble. This therefore may present a possibility that most of the detected core collapse SNRs with an age of a few 1000 yrs are coming from stripped envelope SNe. We are now expanding our study to calculate models for SNRs from a type Ib/c origin to explore this possibility. The results will be reported in a separate paper in the near future.

Another caveat is that it is possible that some of the progenitors are evolving inside or close to an environment with a higher density than the average ISM, for example, giant molecular clouds (MCs). In these environments, the MS wind can sweep up a large amount of gas in the surrounding dense gas and rapidly convert its kinetic energy to thermal energy, halting its expansion effectively (Mackey et al., 2015). In addition, the emission luminosity is also expected to be higher because of the high density. However, these SNRs are exploded in a small cavity surrounded by a dense environment, so they are expected to enter the radiative phase quickly and become very dim (so-called “dark SNRs"), and their lifespans will be relatively short anyway.

Anyhow, the detection of MS bubbles around SN progenitors is indispensable for a resolution. However, that is quite difficult because MS bubbles typically have very low densities and high temperatures, so that both emission and absorption are inefficient. Gvaramadze et al., 2017 reported a first example of MS bubble detection. By comparison to radiation-hydrodynamics simulations, they interpreted the observation by the collision of the MS wind from B type stars and nearby MCs. While illuminating, a statistical discussion of MS bubble is still impossible due to the small sample of observational examples. Theoretical approaches is therefore important. An expansion of our work to consider higher density environments will be done in a follow-up paper.

At last, we note that our simulations are 1-dimensional and do not include

multi-dimensional effects. This imposes that the ISM is isotropically distributed. If the wind material and ISM distribute anisotropically, and/or the SN exploded asymmetrically, a non-spherical situation is expected, probably accompanied by bow shocks (e.g., Mohamed, Mackey, and Langer, 2012). Multi-dimensional effects like Rayleigh-Taylor fingers have been observed too in a number of remnants like Tycho (e.g., Warren et al., 2005) which can also affect the emission to some extent. To investigate these effects, especially for the modeling of specific objects, multi-D simulations will indeed be desirable. As a first study, however, we aim at constructing a "standard" evolutionary picture for Type II SNRs in general, and evaluate the effects of the (non-)existence of a rarefied MS bubble beyond the RSG wind on the bulk properties of the non-thermal emission. In this context, we consider a parametric study using 1-D simulations suitable.

3.5 Conclusion

Young SNRs are usually bright in multi-wavelength from radio to γ-ray from the interaction between CRs accelerated by the SNR shock and the surrounding ambient environment. This suggests that non-thermal emissions from SNRs are effective probes of the CSM structure and hence the mass-loss history of SN progenitors. In this work, we have calculated the long-term time evolution of non-thermal emissions from Type II SNRs interacting with a realistic CSM considering stellar evolution and mass-loss history of their progenitors.

We show that the non-thermal emissions are bright enough to be observed by current and future detectors in the RSG wind phase ($t \leq 1000$ yr), but become very faint beyond detectable in the MS bubble phase (1000 yr $\leq t \leq$ 5000 yr). After the collision with the MS shell ($t \geq$ 5000yr), the SNR rebrightens in radio and γ-rays, but gradually declines in luminosity immediately afterwards due to a rapid deceleration of the shock in the dense cold shell. We conclude that most Type II SNRs experience a "dark age" from 1000 to 5000 yrs for progenitors with ZAMS mass $M_{\rm ZAMS} \leq 18\ M_\odot$ exploded in a typical ISM surrounding. This phenomenon is mainly caused by an inefficient particle acceleration and fast adiabatic loss in the thin and hot MS bubble. Our results may help to fill in the gap between the Galactic SN rate and SNR observations. While the existence of a spatially extended MS bubble around massive stars is still uncertain, and is affected by various factors such as the wind properties, the surrounding ISM environment and so on,

our conclusion is robust in that it does not depend on any fine-tuning of parameters of aspects such as particle acceleration and explosion properties. A further investigation by expanding our parameter space including different progenitor systems is under way and will be reported in a follow-up work.

Chapter 4

Resurrection of Nonthermal Emissions from Type Ib/c Supernova Remnants

Part of this chapter was accepted for publication in the Astrophysical journal.

4.1 Scope of this chapter

Core-collapse supernovae (SNe) are classically divided into two major classes; Type II SNe and Type Ib/c SNe (Elias et al., 1985; Wheeler and Harkness, 1986). This classification is based on the presence or absence of absorption lines from H and He in their spectra around the maximum light. The difference is believed to be originated from the differences in the nature of their progenitor stars and the associated mass-loss histories. The classification of SN types is hence important for the investigation of stellar evolution of massive stars and their explosion mechanism(s).

The rate of Type Ib/c SNe is estimated to be about one-third of their Type II counterpart (e.g., Smith et al., 2011). However, a smoking-gun observational evidence for a Type Ib/c supernova remnant (SNR) is still absent. Type Ib/c SNe are also noteworthy from the perspective of the production of neutron star systems and millisecond pulsars (e.g., Tauris and Savonije, 1999; van den Heuvel, 2009; Wang et al., 2021), and theoretical studies of Type Ib/c SNe have developed rapidly in the past few decades (e.g., Smith, 2017; Yoon, 2017; Woosley, 2019; Ertl et al., 2020; Woosley, Sukhbold, and Janka, 2020; Woosley, Sukhbold, and Kasen, 2021). On the other hand, detailed evolution and emission models for Type Ib/c SNRs are still scarce in the literature, which, however, are essential for their future identifications and a comprehensive understanding of the SNR population. In fact, there are only few

examples of known Galactic SNRs which are speculated to bear a Type Ib/c origin, such as RX J1713.7-3946 (Katsuda et al., 2015). A theoretical study linking SNe and SNRs (Yasuda, Lee, and Maeda, 2021, hereafter YLM21) in a self-consistent evolution model is an urgent and crucial task.

In this chapter, we first prepare self-consistent CSM models taking into account the stellar evolution and mass-loss history of a Type Ib/c progenitor using one-dimensional hydrodynamic simulations. Second, we calculate long-term time evolution of the SNR dynamics and the resulted non-thermal emissions produced by the interaction of the SNR with their CSM environments up to an age of 10^4 yr. In Section 4.2, we briefly introduce our simulation method for the hydrodynamics, particle acceleration, and the construction of CSM models aided by knowledge from SN observations and progenitor models. In Section 4.3, we show the results on the non-thermal emissions from Ib/c SNRs with different progenitor masses and CSM structures, and their detectability by currently available and future detectors. Discussion and conclusions can be found in Section 4.4 and Section 4.5.

4.2 Method

4.2.1 Particle acceleration and Hydrodynamics

We use the well-tested *CR-Hydro* hydrodynamic code as in YLM21, which has also been used recently in YL19 and decades of previous works referenced therein. This code simultaneously calculates the hydrodynamic evolution of a SNR coupled to the particle acceleration at the SNR shocks and the accompanying multi-wavelength emission in a time and space-resolved fashion. In this section, we introduce the *CR-Hydro* code briefly, and other details can be referred in YL19; YLM21.

This code solves the hydrodynamic equations written in Lagrangian coordinate m which assumes a spherical symmetry and includes feedbacks from efficient cosmic rays (CRs) production via nonlinear diffusive shock acceleration;

$$\frac{\partial r}{\partial m} + \frac{1}{4\pi r^2 \rho} = 0 \tag{4.1}$$

$$\frac{\partial u}{\partial t} + \frac{\partial}{\partial m}\left(P_{\rm g} + P_{\rm CR} + \frac{B^2}{8\pi}\right) = 0 \tag{4.2}$$

$$\frac{\partial e}{\partial t} + \frac{\partial}{\partial m}\left[\left(P_{\rm g} + P_{\rm CR} + \frac{B^2}{8\pi}\right) u\right] = -n^2 \Lambda_{\rm cool} \tag{4.3}$$

$$e = \frac{1}{2}u^2 + \frac{1}{\rho}\left(\frac{P_{\rm g}}{\gamma_{\rm g}-1} + \frac{P_{\rm CR}}{\gamma_{\rm CR}-1} + \frac{B^2}{8\pi}\right). \tag{4.4}$$

The code also solves the diffusion-convection equation written in the shock-rest frame assuming a steady-state and isotropic distribution of the accelerated particles in momentum space (Caprioli, Amato, and Blasi, 2010; Caprioli et al., 2010; Lee, Ellison, and Nagataki, 2012b);

$$\begin{aligned}&[u(x) - v_A(x)]\frac{\partial f_p(x,p)}{\partial x} - \frac{\partial}{\partial x}\left[D(x,p)\frac{\partial f_p(x,p)}{\partial x}\right] \\ &= \frac{p}{3}\frac{d[u(x)-v_A(x)]}{dx}\frac{\partial f_p(x,p)}{\partial p} + Q_p(x,p).\end{aligned} \tag{4.5}$$

In the above equations, ρ, $P_{\rm g}$, and u are the mass density, pressure, and flow velocity of thermal gas, $P_{\rm CR} = \int 4\pi p^2 f_{\rm p} dp$ is the CR pressure, and $f_{\rm p}(x,p)$ is the phase-space distribution function of the accelerated protons. By adopting the so-called thermal-leakage model (Blasi, 2004; Blasi, Gabici, and Vannoni, 2005) as a convenient parameterization for the DSA injection term $Q_p(x,p)$, we can obtain the semi-analytic solution of $f_p(x,p)$ (Caprioli, Amato, and Blasi, 2010; Caprioli et al., 2010; Lee, Ellison, and Nagataki, 2012b), for which the explicit expression can be found in YL19; YLM21. The treatment of the magnetic field strength $B(x)$ and the spatial diffusion coefficient $D(x,p)$ of the accelerating particles can also be found in YLM21.

In addition, we parametrically treat the electron distribution function as $f_e(x,p) = K_{\rm ep} f_p(x,p)\exp[-(p/p_{\rm max})^{\alpha_{\rm cut}}]$. $K_{\rm ep}$ typically takes a value between 10^{-3} and 10^{-2} which is limited by SNR observations so far. The determination of the maximum momenta $p_{\rm max}$ and the cut-off index $\alpha_{\rm cut}$ is done in the same way as in YL19.

The accelerated particles are advected to the downstream and are assumed to be co-moving with the post-shock gas flow by magnetic confinement. Both the freshly accelerated particles at the shock and the advected particles interact with their surrounding gas to produce multi-wavelength non-thermal emissions and meanwhile lose their energies through radiation and adiabatic expansion. In our models, we include non-thermal radiation mechanisms by synchrotron radiation, inverse Compton scattering (IC), non-thermal bremsstrahlung from the accelerated electrons, and pion productions and decay from proton-proton interactions (π^0 decay) by the accelerated protons. In this study, only the cosmic microwave background radiation (CMB) is considered for the target photon field of IC for generality, but this can be modified when we target any specific SNR.

We note that our code is similar in construct to that used in some previous works (Ptuskin, Zirakashvili, and Seo, 2010; Zirakashvili and Ptuskin, 2012). Zirakashvili and Ptuskin (2012) conducted simulations of SNR evolution and particle acceleration in detail, in which they consider models typical of Type Ia SNRs evolving in a uniform ISM-like environment. In this work, we have included a few additional physical components such as radiative cooling, a treatment of magnetic field amplification (MFA) from resonant streaming instability (Bell, 1978a; Bell, 1978b), as well as a spatially inhomogeneous CSM environment for core-collapse SNRs motivated by the time-dependent mass loss histories of their progenitors prior to explosion, as we will discuss in more detail in the next section.

4.2.2 Circumstellar medium and SN ejecta

In this study, we first construct CSM models for a Type Ib/c SNR by performing hydrodynamic simulations in which stellar winds from the progenitor run into a uniform ISM. We account for the stellar evolution and mass-loss histories of the SN progenitor under a grid of model parameters inspired by observations. These results are used as the initial conditions for calculating the subsequent long-term evolution of the SNR.

The progenitor of a Type Ib/c SN is usually linked to massive OB-type stars with zero-age main sequence (ZAMS) mass $\geq 10 M_{\odot}$ in a binary system. When the progenitors evolve to red supergiants (RSG) after their main sequence (MS), their envelopes fill the Roche-lobe and the hydrogen envelopes are stripped by a Roche-lobe overflow (RLOF). As a result, they evolve to a helium or carbon-oxygen star called a Wolf-Rayet (WR) star, which eventually explode via core collapse. The stellar wind blown in the MS and WR phases are fast because of the compactness of the OB and WR stars, and the total amount of mass lost in these phases is relatively small. On the other hand, the mass-loss mechanism in the RLOF phase is still under discussion. Two channels can be considered: (i) the material stripped by RLOF is spread out into the circumstellar environment in the form of a stellar wind, and (ii) the stripped gas accretes onto the companion stars. It strongly depends on the binary properties such as the mass ratio and separation of the two stars. For simplicity, we treat the accretion efficiency as a parameter ($\beta_{\rm acc}$) in our models, so that $\beta_{\rm acc} \equiv \dot{M}_{\rm sec}/\dot{M}_{\rm pri}$ where $\dot{M}_{\rm pri}$ and $\dot{M}_{\rm sec}$ are the mass loss

rates of the donor star and the accretion rate onto the secondary star, respectively. This procedure is known as a wind Roche-lobe overflow model (Mohamed and Podsiadlowski, 2012; Abate et al., 2013; Ilkiewicz et al., 2019). An effective mass loss rate is then obtained as $(1-\beta_{\rm acc})\dot{M}_{\rm pri}$. In this paper, we consider two extreme cases of $\beta_{\rm acc}=0$ and $\beta_{\rm acc}=1$, and adopt the $\beta_{\rm acc}=0$ case for our main results. Results from the $\beta_{\rm acc}=1$ case is discussed in Appendix A for reference.

The evolution of helium stars up to core collapse is well studied by simulations (e.g., Yoon, 2017; Woosley, 2019; Ertl et al., 2020; Woosley, Sukhbold, and Kasen, 2021; Vartanyan et al., 2021), from which the mass lost in each evolutionary phase and the ejecta mass $M_{\rm ej}$ can be determined for a given ZAMS mass. In this study, we consider two cases for the ZAMS mass in our fiducial models, i.e., a $12M_\odot$ (model A) and $18M_\odot$ (model B) progenitor star. For comparison, we prepare two additional models (models C and D) in which the ZAMS mass is the same but the mass loss in the MS stage is not taken into account.

We note that there is another possible way for the stars to explode as Type Ib/c SNe. A star more massive than $M_{\rm ZAMS}\geq 30\ M_\odot$ may evolve as a single star from MS to RSG and becomes a WR star if its mass-loss rate is high enough to strip off their entire hydrogen envelope in the RSG phase. These stars also have massive helium cores, so in order to explode as Type Ib/c SNe, implying a high mass-loss rate in the WR phase as well (Yoon, 2017; Woosley, 2019; Ertl et al., 2020; Woosley, Sukhbold, and Kasen, 2021). We will discuss the results of a single star evolution model with $M_{\rm ZAMS}=30\ M_\odot$ in Appendix A.

The typical mass-loss rate $\dot{M}_{\rm w}$, wind velocity $V_{\rm w}$ and time duration $\tau_{\rm phase}$ in each mass loss phase are $\dot{M}_{\rm w}\sim 10^{-8}-10^{-7}\ M_\odot\ {\rm yr}^{-1}$, $V_{\rm w}\sim 1-3\times 10^3\ {\rm km\ s}^{-1}$, and $\tau_{\rm phase}\sim 10^6-10^7$ yr for the MS phase, $\dot{M}_{\rm w}\sim 10^{-3}-10^{-2}\ M_\odot\ {\rm yr}^{-1}$, $V_{\rm w}\sim 10-100\ {\rm km\ s}^{-1}$, and $\tau_{\rm phase}\sim 10^3-10^4$ yr for the RLOF phase, and $\dot{M}_{\rm w}\sim 10^{-6}-10^{-5}\ M_\odot\ {\rm yr}^{-1}$, $V_{\rm w}\sim 1-3\times 10^3\ {\rm km\ s}^{-1}$, and $\tau_{\rm phase}\sim 10^5-10^6$ yr for the WR phase (e.g., Smith, 2017; Yoon, 2017; Woosley, 2019; Ertl et al., 2020; Woosley, Sukhbold, and Kasen, 2021). We use a time-independent, constant mass loss rate and wind velocity during each phase for simplicity. The exact values used in the models are summarized in Table 4.1.

The SN ejecta mass in each model is calculated as $M_{\rm ej}=M_{\rm ZAMS}-\sum(\dot{M}_{\rm w}\tau_{\rm phase})-M_{\rm rm}$, where $M_{\rm rm}$ is the compact remnant mass after explosion. For the ZAMS mass range we consider in this work, $M_{\rm rm}$ is typically $1.3\sim 1.6\ M_\odot$ (Woosley,

Sukhbold, and Janka, 2020). $M_{\rm rm} = 1.5\ M_\odot$ is adopted in all models here. For the SN ejecta structure, we use the power-law envelope model in Truelove and McKee (1999) for all of our models:

$$\rho(r) = \begin{cases} \rho_{\rm c} & (r \le r_{\rm c}) \\ \rho_{\rm c}(r/r_{\rm ej})^{-n_{\rm SN}} & (r_{\rm c} \le r \le r_{\rm ej}), \end{cases} \tag{4.6}$$

where $\rho_{\rm c}$, $r_{\rm c}$, and $r_{\rm ej}$ are the core density, core radius and ejecta size, respectively, which can be obtained by mass and energy conservation. We assume an explosion kinetic energy $E_{\rm SN} = 1.2 \times 10^{51}$ erg and the power-law index of the envelope $n_{\rm SN} = 10$ (e.g., Matzner and McKee, 1999; Chevalier and Fransson, 2006). The ejecta masses in each model are summarized in Table 4.1.

TABLE 4.1: Wind parameters and ejecta properties for a Type Ib/c SNR. The wind temperature is set to $T = 10^4$ K, SN explosion energy $E_{\rm SN} = 1.2 \times 10^{51}$ erg, power-law index of the ejecta envelope $n_{\rm ej} = 10$, and stellar remnant mass $M_{\rm rm} = 1.5 M_\odot$ (Woosley, Sukhbold, and Janka, 2020) in all models. We also assume $n = 1.0\ {\rm cm}^{-3}$ and $T = 10^4$ K for the outer ISM region.

Model	$M_{\rm ZAMS}$ $[M_\odot]$	Phase	$\dot{M}$ $[M_\odot\ {\rm yr}^{-1}]$	$V_{\rm w}$ [km s^{-1}]	$M_{\rm w}$ $[M_\odot]$	$\tau_{\rm w}$ yr	$M_{\rm ej}$ $[M_\odot]$
A	12	MS	5.0×10^{-8}	2000	0.5	1.0×10^7	
		RLOF	8.5×10^{-4}	10	8.5	1.0×10^4	
		WR	5.0×10^{-6}	2000	0.5	1.0×10^5	1.0
B	18	MS	6.0×10^{-8}	2000	0.3	5.0×10^6	
		RLOF	1.27×10^{-3}	10	12.7	1.0×10^4	
		WR	1.0×10^{-5}	2000	1.0	1.0×10^5	2.5
C	12	RLOF	9.0×10^{-4}	10	9.0	1.0×10^4	
		WR	5.0×10^{-6}	2000	0.5	1.0×10^5	1.0
D	18	RLOF	1.3×10^{-3}	10	13.0	1.0×10^4	
		WR	1.0×10^{-5}	2000	1.0	1.0×10^5	2.5

The results of our stellar wind simulations are shown in Figure 4.1. The upper panel (a) shows the radial density distribution of the CSM created by the stellar wind from a Type Ib/c SN progenitor. The lower panel (b) shows the gas temperature as a function of radius. The red and blue solid lines correspond to the results of the 12 $M_\odot$ (model A) and 18 $M_\odot$ (model B) cases in both panels, respectively. The dashed lines represent the models for which the mass loss in the MS phase is not considered for comparison (models C and D). As the initial condition for the wind simulations, we assume a uniform ISM with $n_{\rm ISM} = 1.0\ {\rm cm}^{-3}$ and $T = 10^4$ K in all of our models.

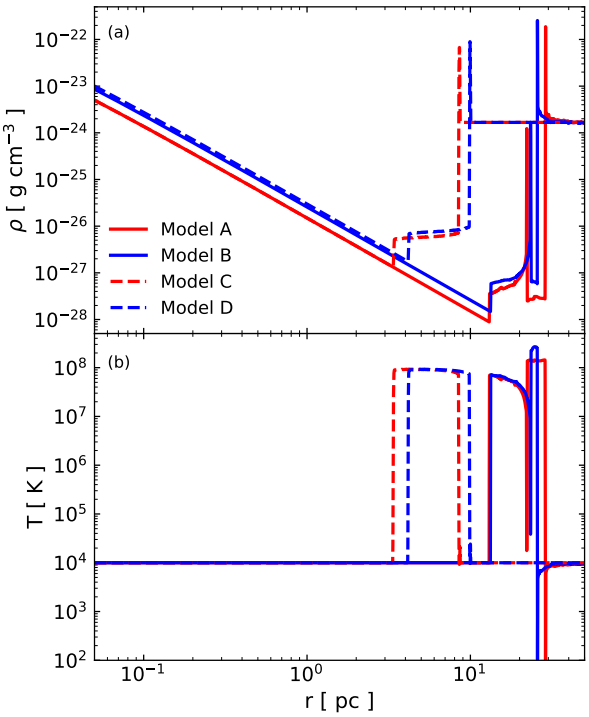

FIGURE 4.1: CSM models for a Type Ib/c SNR. The upper panel shows the gas density as a function of radius, and the lower panel shows the gas temperature. The red (blue) solid line corresponds to the low (high) progenitor mass case. The dashed lines show the results from models for which the mass loss in the MS phase is not considered for comparison.

From the results of model A and B, we can see that the CSM structure can be broken into five characteristic regions from the outer to inner radii; (i) uniform ISM, (ii) MS shell, (iii) MS bubble, (iv) WR shell, and (v) WR wind. The formation mechanism and features of the MS shell and MS bubble have been explained in detail in YLM21. Because the RLOF wind is characterized by a high mass-loss rate but slow velocity and a short time period, a dense ($\rho \geq 10^{-20}$ g cm^{-3}) and compact ($r \leq 0.1$ pc) structure with a power-law profile in density is formed. On the other hand, the subsequent WR wind has a higher velocity and longer time duration than that in the RLOF phase. The fast WR wind hence sweeps up all of the above structures created by previous phases of mass loss, and creates a WR shell at $r \sim 20$ pc. This result implies that the more compact structures in the CSM created before the WR phase are most probably washed away by the subsequent WR wind and accumulate onto the dense WR shell. This can also be seen in the two extra models (the $\beta_{\rm acc} = 1$ model and the $M_{\rm ZAMS} = 30\ M_\odot$ model single star model) to be discussed in Appendix A. The differences in the CSM structure between models A and B are coming from the slight difference in the mass loss rate

and time duration in each pre-SN evolution phase, which leads model B to have the MS shell shifted inward and the WR shell outward, and the size of MS bubble reduced compared to model A.

On the other hand, because models C and D do not include the mass loss in the MS phase intentionally, the CSM structures in these models are relatively simple and can be divided into three main regions: (i) uniform ISM, (ii) WR shell, and (iii) WR wind. One unique feature of these models is that WR shell is located at a small radius $r \sim 10$ pc. In these models, the WR wind first sweeps up the dense CSM material from the RLOF phase (whose structures are almost identical to those of models A and B), beyond which the CSM density is higher than models A and B because a tenuous MS bubble is absent without the mass loss in the MS phase taken into account. The formation of the WR shell thus happens in a shorter timescale than Models A and B since the expanding WR wind cavity is sweeping up the ISM material in the downstream which has a much higher density than the tenuous MS bubble. The rapidly accumulating mass in the WR shell leads to a stronger deceleration of the cavity expansion, and hence a smaller cavity size prior to core-collapse. There is no drastic difference between model C and D. Overall, the (non-)existence of the MS mass loss phase gives rise to the most significant variation in the hydrodynamic structure of the CSM among the models considered in this work.

In the next step, we employ these results as the initial conditions for our simulations of the subsequent SNR evolution after explosion. We note that we do not consider the effect of metallicity in the wind models as well as the SNR simulations, and assume a solar abundance for simplicity. We will discuss this treatment in Section 4.4.

4.3 Results

Equipped by the CSM models described in Section 4.2.2, we next calculate the hydrodynamic evolution of a Type Ib/c SNR up to an age of 10^4 yr, and the non-thermal emissions resulted from the interaction of the SNR blastwave with the CSM environments.

4.3.1 Hydrodynamics

Figure 4.2 shows the time evolution of the SNR radius $R_{\rm sk}$ (upper panel), shock velocity $V_{\rm sk}$ (middle panel), and the magnetic field $B(x)$ at the shock

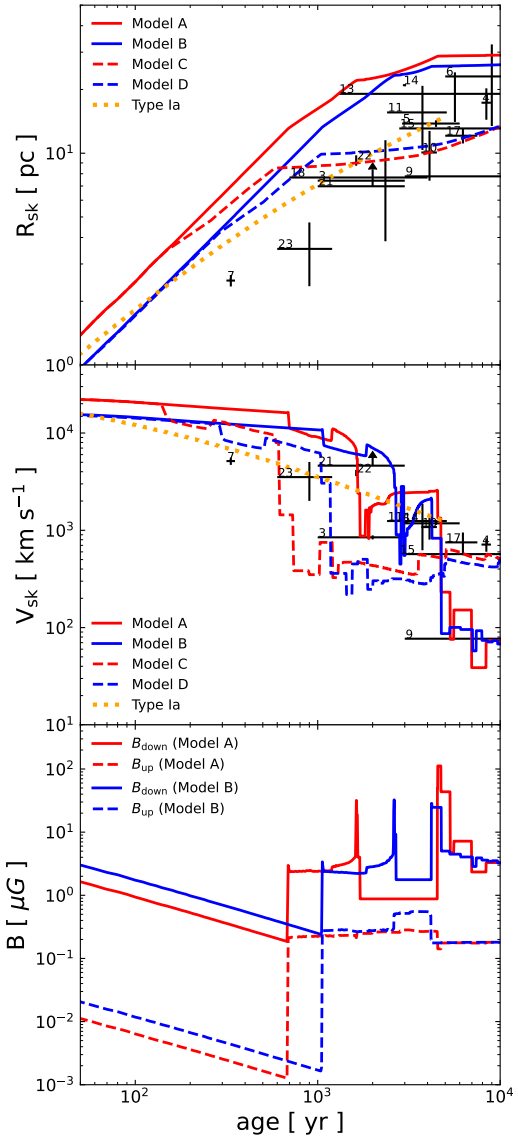

FIGURE 4.2: The hydrodynamic evolution of a Type Ib/c SNR. The upper panel shows the time evolution of the forward shock radius, the middle panel shows the shock velocity as a function of SNR age, and the lower panel shows the magnetic field at the immediate upstream and downstream of the shock. The line formats in upper and middle panels are the same as in Figure. 4.1. The orange dotted lines are taken from Model A2 in YL19 for comparison (see text). Actual observational data of selected core-collapse SNRs are overlaid, for which the references can be also found in YL19. In the lower panel, the red (blue) line shows the magnetic field strengths near the forward shock from Model A (B). The solid (dashed) lines represent values measured at the immediate downstream (upstream) of the forward shock.

position (lower panel) for each model. Similar to YLM21, we also plot the results from a Type Ia SNR model for comparison (see YL19 and YLM21 for

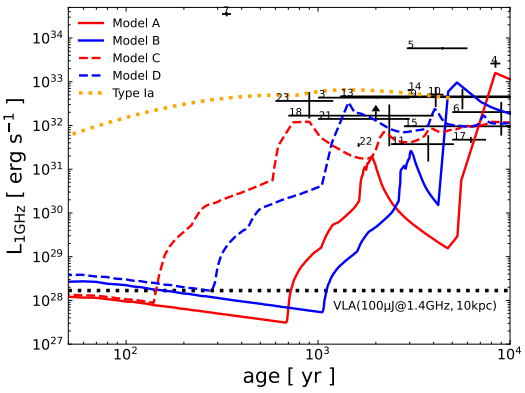

(a)

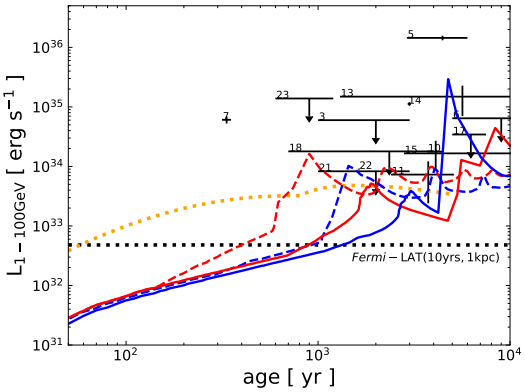

(b)

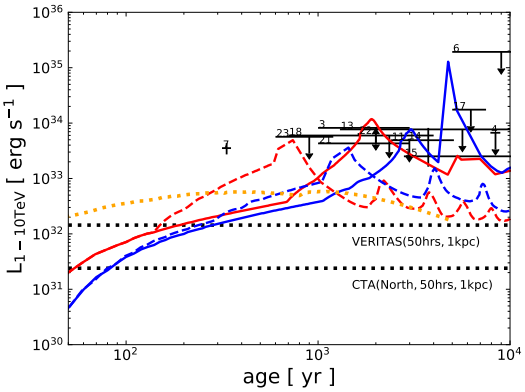

(c)

FIGURE 4.3: Light curves of the 1 GHz radio continuum (panel (a)), γ-ray emissions integrated over the 1-100 GeV band (panel (b)) and 1-10 TeV band (panel (c)) are shown. The line formats are the same as in Figure 4.2. The detection limit of VLA in panel (a), *Fermi*-LAT in panel (b), and VERITAS and CTA in panel (c) are plotted with black dotted lines, respectively. The results from multi-wavelength observations of selected SNRs as shown in Figure 4.2 are also overlaid.

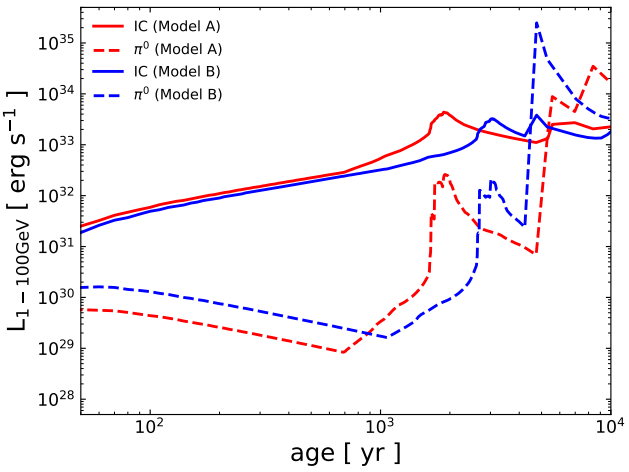

(a)

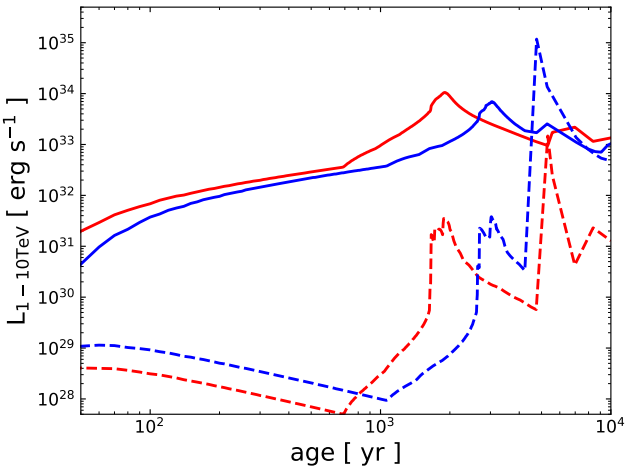

(b)

FIGURE 4.4: Same as panels (b) and (c) in Figure 4.3, but the contribution from each emission component is shown separately. The solid (dashed) line shows the IC (π^0 decay) component, and the red (blue) color represents the results from Model A (B).

details.). Observational data of selected core-collapse SNRs are also overlaid as black data points. These SNRs are chosen from the γ-ray source catalog of *Fermi* (Acero et al., 2016) and H. E. S. S. (H. E. S. S. Collaboration et al., 2018), and the exact values and references can be found in YL19.

We first look at the results of models A (red solid line) and B (blue solid line) in upper and middle panels. In the early phase ($t \leq 1,000$ yr), the SNR forward shock freely expands into the tenuous unshocked WR wind with a velocity $\sim 10,000$ km s^{-1}. Afterwards at an age of ($1,000$ yr $\leq t \leq 5,000$ yr), the SNR blastwave collides with the WR shell, and the shock speed

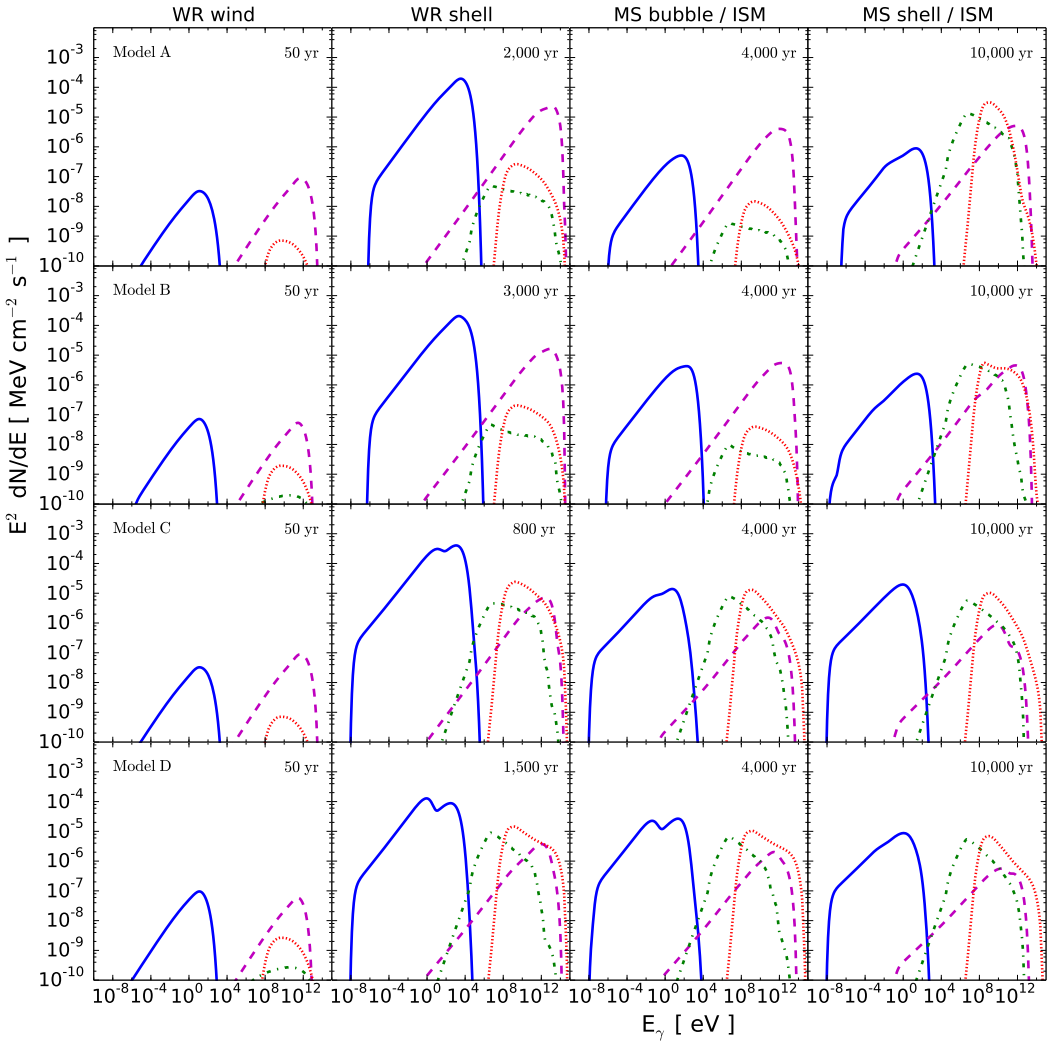

FIGURE 4.5: Broadband SED from a Type Ib/c SNR with different progenitor masses and CSM models (top to bottom) and at different ages (left to right). The exact age is shown in each panel at the upper right corner. The emission components correspond to synchrotron (blue solid), IC (magenta dashed), nonthermal bremsstrahlung (green dot-dashed) and π^0 decay (red dotted). The distance from a source is assumed to be 1 kpc.

decreases to $\leq 1,000$ km s^{-1}. The shock eventually breaks out from the WR shell into the low-density hot MS bubble, and the shock velocity restores to $\sim 2,000$ km/s. In the late phase ($t \geq 5,000$ yr), the blastwave hits a dense wall at the MS shell and decelerates to ≤ 100 km s^{-1}. As the shock sweeps up the large amount of gas contained inside the MS shell, the SNR makes a transition to its radiative phase, and slowly expands into the ISM region after the shock breaks out from the MS shell. The differences between these models are mainly in the timings of transition into each dynamical phase as stated above, which in turn originate from the differences in the mass-loss

rates and durations in each pre-SN evolutionary phases, as well as the ejecta mass.

From models C (red dashed line) and D (blue dashed line) in upper and middle panels, we find that the evolution in the early phase is similar to model A and B as the SNR expands into the unshocked WR wind until it hits a the termination shock and starts decelerating at an age $\sim$ 100 yr. Afterwards, the shock collides with the dense WR shell and slows down to a velocity of the order of 100 km s^{-1} at an age of around 1,000 yr. As this happens, the SNR again sweeps up a large amount of gas inside the WR shell and enters the radiative phase. When the radiative shock runs into the ISM region, the expanding hot SN ejecta heated by the reverse shock pushes the cold dense shell formed behind the radiative forward shock outward, causing the forward shock velocity to oscillate (see, e.g., Lee et al., 2015). The differences between these models are the same as what we have described above. From these results, we can see that the (non-)existence of a MS bubble critically affects the dynamical evolution of a Type Ib/c SNR.

In the lower panel, we can see that the magnetic field strengths at the immediate downstream of the shock (solid lines) are amplified from those in the upstream (dashed lines). Their evolution reflects closely the CSM structure and the shock velocity which are critical parameters for the particle acceleration efficiency and therefore the strength of the CR-driven magnetic turbulence.

4.3.2 Non-thermal emissions

Figure 4.3 shows the light curves of the 1 GHz radio continuum (panel (a)), γ-ray emissions in the 1-100 GeV band (panel (b)), and the 1-10 TeV band (panel (c))[1]. The line formats and colors are the same as in Figure 4.2. The contributions from IC and π^0 decay are independently plotted in Figure 4.4. The corresponding spectral energy distribution (SED) of each model is plotted in Figure 4.5 at four characteristic ages from left to right, which is explicitly indicated at the upper right corner of each panel.

[1]We note that X-ray emission is also important for deciphering the properties of SNRs. X-rays from SNRs are produced by not only synchrotron radiation but also thermal components including bremsstrahlung, various continua, and line emission from the hot plasma confined between the forward and reverse shock. By focusing on the non-thermal components in this work, we postpone the presentation of light curves in the X-ray bands to a future work in which a proper implementation of the thermal emission will be included.

From the results of models A and B, we can observe that both the GeV and TeV γ-ray luminosities gradually increase with time, while the radio counterpart decreases during the first 1,000 yrs. This can be understood as follows. The dominant emission mechanisms for the radio emission is synchrotron radiation, while that for the γ-rays is IC for both the GeV and TeV bands (see Figure 4.4 and the left panels in Figure 4.5). The synchrotron emissivity is proportional to both the total number of the non-thermal electrons as well as the square of the downstream magnetic field strength. While the wind density drops with radius as r^{-2} so that the injection rate becomes smaller with time, the number of accelerated electrons integrated over the volume of the SNR does increase with time as they are advected and accumulate in the downstream. The magnetic field strength immediately upstream from the shock is proportional to r^{-1} from the density structure, and the field strength behind the shock further decreases from adiabatic expansion and flux conservation as the shocked gas advects downstream, assuming that the magnetic fields are frozen in the shocked plasma. The overall synchrotron flux hence decreases with the expansion of the SNR. On the other hand, the IC emissivity is proportional to the product of the number of accelerated electrons and the energy density of the target photon field. Because the CMB is assumed as the photon target of IC in this work which is constant in space, IC flux increases with time as the shock keeps accelerating electrons from the inflowing wind material.

After that, as the shock approaches the WR shell, the luminosities in both radio and γ-rays increase with time and reach their first maxima at $\sim$2,000 to 3,000 yrs. Until $\sim$4,000 to 5000 yrs, the SNR expands and breaks out into the tenuous MS bubble, and the non-thermal emission suffers a decay of 1 to 2 orders of magnitude from the rapid adiabatic loss, but this declination does not make the SNR undetectable by current and future instruments because the spatial extend of the MS bubble is compact as we have already explained in Section 4.2.2. Finally, the SNR collides with the dense MS shell and becomes bright again in all wavelengths. Once the shock enters the ISM region, it becomes hard for the shock to accelerate particles efficiently anymore due to its low velocity, and the luminosities gradually decrease with time via adiabatic loss again.

As mentioned in Section 4.2.2, the WR shells in models C and D are located at smaller radii than those in model A and B (see Figure 4.1 again), so that the luminosities begin to rise earlier from a few 100 yrs and reach the maximum brightness at around 1,000 yrs. Until 10,000 yrs, the luminosities

stay at more-or-less the same level except for slight oscillations originating from the velocity fluctuation of the radiative shock as seen in Figure 4.2.

From the SED in Figure 4.5, we can also see a steepening of the π^0 decay spectra in all models, which comes from the steepening of the underlying proton spectrum. The power-law index of the proton spectrum is roughly obtained as $d\ln f(p)/d\ln p \sim -3S_{\rm tot}/(S_{\rm tot}-1)$, where $S_{\rm tot}$ is the effective compression ratio (e.g., Caprioli et al., 2009) which is determined by the difference between the shock velocity and the velocity of the magnetic scattering centers. In situations where MFA is efficient, the effective compression ratio can become smaller than 4 and the resulting proton spectra hence steepen. As a result, when π^0 decay is the dominant emission channel in the late evolutionary phase, the total γ-ray spectrum is characterized by a soft spectrum.

We note that the luminosity of the “Type Ia" model referenced here is relatively large compared to the Type Ib/c models, especially in the early phase. This is stemming from differences in the assumed DSA injection rate $\chi_{\rm inj}$ and the surrounding ISM/CSM environment. The injection rate $\chi_{\rm inj}$ determines the amount of particles injected into the acceleration process and the resulting acceleration efficiency (see, e.g., Blasi, 2004; Blasi, Gabici, and Vannoni, 2005). Here, we have adopted $\chi_{\rm inj} = 3.6$ for the Type Ia model and $\chi_{\rm inj} = 3.75$ for the Type Ib/c models based on YL19. More importantly, according to our CSM models, Type Ib/c SNRs expand into a tenuous wind cavity whereas the Type Ia model adopts a uniform ISM-like environment with $n_{\rm ISM} = 0.1$ cm^{-3} as in YL19. While the absolute luminosities do depend on the DSA parameters which should be constrained by observation data of individual SNRs, our results show that the light curve of a Type Ia SNR evolving in a more-or-less uniform ISM is expected to be much flatter and uncharacteristic compared to the remnants of Type Ib/c SNe, for which the latter heavily anchors to the highly inhomogeneous structure of the CSM environment and hence the progenitor mass loss history.

We can now assess the observational detectability of a Type Ib/c SNR based on our models. The sensitivities of various instruments are plotted in all panels in Figure 4.3 with black dotted lines. For the radio band, we compare the detection limit of the Very Large Array (VLA) with our models. The sensitivity for a targeted observation of objects like radio galaxies and active galactic nuclei is ~ 100 μJy at 1.4 GHz (e.g. Schinnerer et al., 2004; Simpson et al., 2012), and the lower limit from a source at a distance of 10 kpc therefore corresponds to $\sim 2\times10^{28}$ erg s^{-1}. We note that non-targeted sky surveys

have much shallower sensitivities, but this does not affect the following discussion and our main conclusion. We use the sensitivity of the *Fermi* Large Area Telescope (*Fermi*-LAT) for the GeV γ-rays, and VERITAS (Very Energetic Radiation Imaging Telescope Array System) and the Cherenkov Telescope Array (CTA) for TeV γ-rays. Based on 10 yrs of survey data[2] (see, for details, Abdollahi et al., 2020; Ballet et al., 2020), the flux sensitivity of *Fermi*-LAT in the 1-100 GeV is $\sim 2 \times 10^{-12}$ erg cm^{-2} s^{-1}, which corresponds to a luminosity $\sim 4.8 \times 10^{32}$ erg s^{-1} for a γ-ray source at 1 kpc. That of VERITAS and the northern telescopes of CTA in the 1-10 TeV band with an observation time of 50 hrs is $\sim 6 \times 10^{-13}$ erg cm^{-2} s^{-1} and $\sim 10^{-13}$ erg cm^{-2} s^{-1}, respectively[3]. For a source at a distance of 1 kpc, the detection limits are $\sim 1.4 \times 10^{32}$ erg s^{-1} and $\sim 2.4 \times 10^{31}$ erg s^{-1}. In this calculation, we do not take other effects like interstellar absorption into account.

Our results show that Type Ib/c SNRs are most probably too faint to be observed in radio and GeV γ-rays in the first 1,000 yrs after explosion, although they can potentially be detected as a TeV-bright SNR in the CTA era if they are close by ($\leq$ 1 kpc). On the other hand, the SNRs are bright enough to be detectable in all wavelengths from 1,000 to 10,000 yrs after the blastwave has swept through the low-density WR wind and starts to interact with the denser CSM beyond the WR wind. We can conclude that Type Ib/c SNRs are very likely to experience a "resurrection" in non-thermal brightness, meaning that they are too dark to be observable in the first 1,000 yrs but re-brighten significantly afterwards until 10,000 yrs. If the MS bubble does not exist, even younger SNRs can become detectable. However, we note that while the occurrence of the "resurrection" is a robust prediction of our models, its exact timing depends on various additional factors which we have not fully explored in our parameter space, such as the nature of the progenitors including their ZAMS masses and mass-loss rates, and their surrounding ambient environment in which they evolve (e.g., in or near a giant molecular cloud (MC)).

[2] https://www.slac.stanford.edu/exp/glast/groups/canda/lat_Performance.htm

[3] VERITAS specifications from https://veritas.sao.arizona.edu/about-veritas/veritas-specifications, and CTA performance from https://www.cta-observatory.org/science/ctao-performance/

4.4 A comparison with Type II SNRs

4.4.1 Light curves

The present results as complemented with the results of YLM21 provides a new picture of SNR evolution highlighted by the difference between Type II and Ib/c SNRs, which is directly linked to their progenitor evolution. Figure 4.6 compares the model light curves of Type II SNRs from YLM21 and Type Ib/c SNRs presented in this study. The red lines correspond to Type II remnants (see Models A and B in YLM21) and the blue lines to Type Ib/c objects (this work). The solid and dashed lines represent models with $M_{\rm ZAMS} =$ 12 $M_\odot$ and 18 $M_\odot$, respectively. In YLM21, the authors proposed that Type II SNRs are very likely to experience a "dark age" in which the SNRs become too faint to detect in multi-wavelengths for a prolonged period of time. Meanwhile, this work suggests that Type Ib/c SNRs can experience a "resurrection" after a certain age. Combining these results and for a fixed condition of the ambient ISM, it can be found that Type II SNRs tend to be bright when Type Ib/c ones are faint, and vice versa. These results suggest a profound implication that there may exist an observational bias in the detected SNR population, in which there is a correlation between the SNR ages and their originating SN types and progenitor natures, thus providing an additional tool for the back-engineering of the observed SNRs and linking them to their progenitor stars and SN explosions.

However, the determination of SNR age (and distance for that matter) is usually a nontrivial task. Except when a SNR is identified with historical SN like Tycho's and Kepler's SNR, the age is generally obtained by from the sigma-D relation (e.g., Poveda and Woltjer, 1968; Clark and Caswell, 1976; Case and Bhattacharya, 1998), which can involve large uncertainties. Suzuki et al., 2020 shows that the dynamical age from fitting the apparent diameter with the Sedov solution provides good agreement with the plasma age inferred from X-ray observations of the non-equilibrium ionization plasma in several SNRs (see their Figure 9). Further improvements in the accuracy of age determination through multi-wavelength observations are hence critical for linking any observed core-collapse SNR to its progenitor origin and SN type.

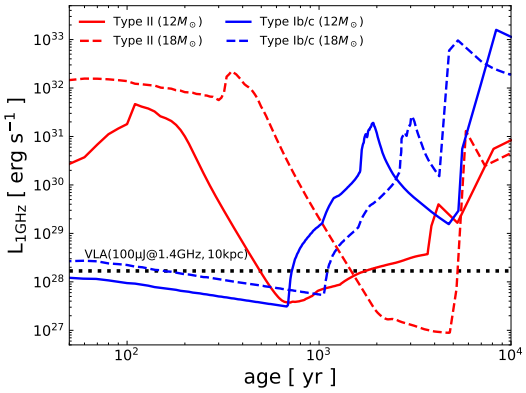

(a)

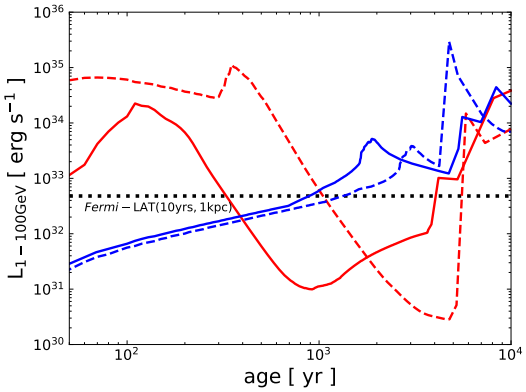

(b)

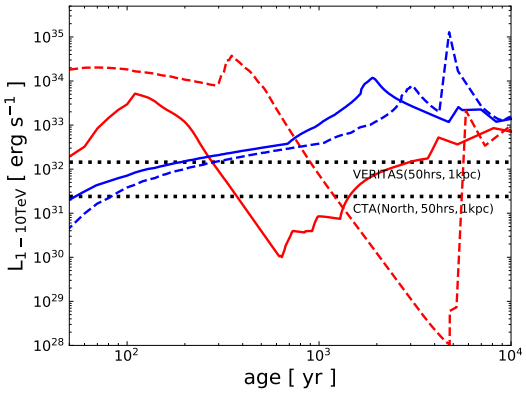

(c)

FIGURE 4.6: Comparison of Type II SNRs (red lines; YLM21) and Type Ib/c SNRs (blue lines; this work). Solid lines plot the results of $M_{\rm ZAMS} = 12\ M_\odot$ model and dashed lines show those of 18 $M_\odot$ model for both colors. The detection limit of various detectors are also plotted with black lines as shown in Figure 4.3.

4.4.2 Spectral properties

In addition, we found that our results well reproduce the observations of several γ-ray bright SNRs as well in terms of their spectral properties. As mentioned above, Type II SNRs are bright in γ-rays in their early evolutionary phase. As shown by Figure 4 in YLM21, their dominant γ-ray emission process is via π^0 decay. On the other hand, Type Ib/c SNRs are γ-ray bright in ages when their Type-II counterparts tend to become faint with the primary emission component being IC emission (see upper panels in Figure 4.5). From these results, one can expect that the γ-ray spectrum of an SNR is characterized by (i) a flat spectra produced by π^0 decay at a very young age ($\leq$ 1,000 yrs old) as dominated by a Type II origin, (ii) a hard spectrum from IC emission at intermediate ages ($\leq$ 5,000 yrs old) with a Type Ib/c origin, and (iii) a soft spectrum at older ages ($\geq$ 10,000 yrs old) independent of SN type (i.e., a mixture of Type II and Ib/c SNRs) as the shock has collided with the dense MS shell and decelerates, with π^0 decay being the dominant emission component. In panel (a) of Figure 4.7, we plot our simulation results for the SEDs in the sub-GeV to 100 TeV band of Type II SNRs and Type Ib/c ones at the indicated characteristic ages. Meanwhile, panel (b) shows the observed γ-ray SEDs of a few core-collapse SNRs. Indeed, we can see that very young objects like Cas A do exhibit a relatively flat spectrum (Acciari et al., 2010; Yuan et al., 2013; Ahnen et al., 2017; Abeysekara et al., 2020), while SNRs of a few 1,000 yrs old like RX J1713.7-3946 (Abdo et al., 2011; H. E. S. S. Collaboration et al., 2018), Vela Jr (Tanaka et al., 2011; H.E.S.S. Collaboration et al., 2018a), and G150.3+4.5 (Devin et al., 2020) show harder spectra, and the more evolved middle-aged SNRs like IC 443 and W44 (Ackermann et al., 2013) typically show very soft spectra. While this general agreement does not necessarily imply that the picture above is applicable for every single individual object, our results imply in general a strong correlation of the γ-ray spectral properties of a SNR with its progenitor nature and hence the mass-loss history and CSM structure.

We emphasize that this transition of the SED properties is expected only when we consider the mass-loss histories of the progenitors. For example, YL19 also attempted to calculate the time evolution of core-collapse SNRs with a method similar to this work, but they assumed that the SNRs are embedded within a simple power-law CSM ($\rho \propto r^{-2}$) without considering the pre-SN mass loss history. Their more simplistic models did not predict such a SED transition described above regardless of the choice of parameters such as the mass-loss rate, whereas the transition emerges naturally in this work

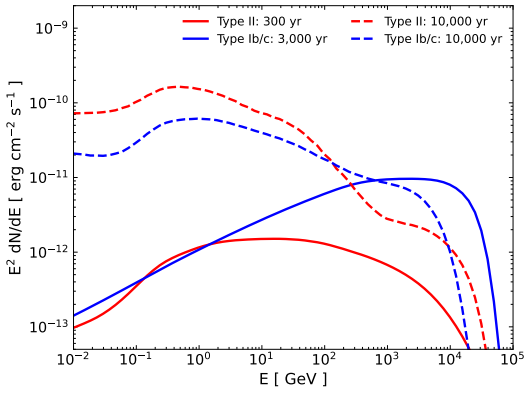

(a)

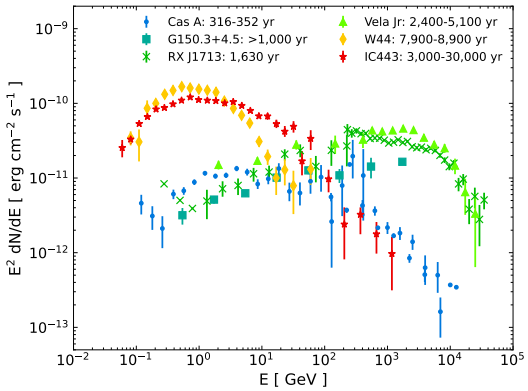

(b)

FIGURE 4.7: Upper panel (a): simulated γ-ray SED from this work and YLM21. Red lines show the results of Model A in YLM21 at 300 yr (solid) and 10,000 yr (dashed), and Blue ones correspond to those of Model A in this work at 3,000 yr (solid) and 10,000 yr (dashed). Lower panel (b): SEDs of several core-collapse SNRs. References of each SNR: Cas A (Ahnen et al., 2017; Abeysekara et al., 2020), G150.3+4.5 (Devin et al., 2020), RX J1713 (H. E. S. S. Collaboration et al., 2018), Vela Jr (Tanaka et al., 2011; H.E.S.S. Collaboration et al., 2018a), W44 (Ackermann et al., 2013), and IC443 (Albert et al., 2007; Ackermann et al., 2013). The values of age estimations are taken from SNRcat (Ferrand and Safi-Harb, 2012, and `http://www.physics.umanitoba.ca/snr/SNRcat/`).

and YLM21 by using more self-consistent CSM models linked to the evolution of the progenitor stars. Moreover, a mixture of SN types is found to play an important role as well.

4.4.3 Additional remarks

One caveat is that our simulation is one-dimensional and we assume that the SN progenitors evolve into an ISM with a fixed density of 1 cm^{-3}. However, many core-collapse SNRs are known to have asymmetrical morphologies, and some of them are known to be interacting with high-density materials like MCs as mentioned above. Hence, we do not expect that our results can be applied to explain detailed properties of every individual SNR. The investigation of multi-dimensional effects and the diversity of the surrounding ISM is postponed to a future work. Nonetheless, we believe that our one-dimensional but sophisticated evolution models succeed to capture a big picture of how the pre-SN evolution of the progenitors which spans millions of years can be linked to the observational properties (non-thermal emission in particular for this work) of their SNRs thousands of years after the explosion.

Another additional factor that we have not explored yet is the effect of a non-solar metallicity. We assume a solar abundance throughout our simulation box, while we expect that the WR wind should possess a metal-rich composition such as Helium and/or Carbon-Oxygen. However, we note that this does not affect our main results because the dominant non-thermal emission mechanisms while the blastwave is inside the WR wind are from synchrotron in radio and IC in GeV-TeV band respectively, for which the effect from an altered metallicity is mainly on the free electron number density. We can estimate that the change of the density in a helium-rich environment is only about a factor different from that in an environment with a solar-like abundance. This error is much smaller than the uncertainties from poorly constrained parameters such as the mass-loss properties, distance and so on. We hence ignore the metallicity for our calculations of non-thermal emissions here as a secondary effect. A future follow-up study will include other processes such as heavy ion acceleration and escape in the stellar wind as well (Biermann et al., 2010; Ohira and Ioka, 2011; Aguilar et al., 2015b; Aguilar et al., 2015a; Aguilar et al., 2017) and investigate their effects on the resultant non-thermal emission properties.

Finally, it is illustrative to discuss other possible subtypes of SNRs beyond what we have modeled so far. For example, almost 10% of all core-collapse SNe are classified as Type IIb (Smith et al., 2011), of which the representative remnant objects include the Galactic SNR Cassiopeia A (Borkowski et al., 1996; Krause et al., 2008) Their progenitors are believed to be helium stars embraced by a thin hydrogen envelope that is not completely stripped off by the binary interaction and stellar winds. They show a diversity in the CSM

density, but it is generally larger than the WR wind case and close to the RSG wind. As such, we expect that Type IIb SNRs will evolve in a similar manner with Type II SNRs. In addition, the diversity in the CSM density and thus in the final mass-loss rate is suggested to be linked to the timing of the binary interaction (Maeda et al., 2015), which may reflect expected diversity in the initial binary configuration leading to SNe IIb (Ouchi and Maeda, 2017). Therefore, theoretical investigation adopting a realistic mass-loss history for SNe IIb will provide an interesting possibility to further constrain the details of the stellar evolution scenarios and roles of the binary interaction toward SNe. An expansion of our work to model other possible types of SNRs will be found in a follow-up paper.

4.5 Conclusion

Non-thermal emission from various types of SNRs is an effective probe of their surrounding environment and hence the nature and evolution of their progenitor stars. Following the method of YLM21 who focused on Type II SNRs, we have conducted simulations of the long-term evolution of Type Ib/c SNRs interacting with their CSM in this work, taking into account the mass-loss history of their progenitors. The non-thermal emissions produced by the interactions between the accelerated CRs and the surrounding environment are presented.

We show that the non-thermal emissions from Type Ib/c SNRs are faint and below the sensitivities of current and near-future detectors in the early phase when the SNR blastwave is inside the unshoced WR wind region ($t \leq 1,000$ yr), except if the source is extremely close ($d \leq 1$ kpc) and the TeV emission can be potentially picked up by future observatories such as CTA. These objects are also predicted to be non-thermally bright after the SNR shock has begun to penetrate through the WR wind shell ($t \geq 1,000$ yr). As the SNR shock passes through the dense shell at around 2,000-3,000 yrs, the brightness of SNRs decreases gradually due to the weakening of the shock and fast adiabatic cooling in the hot compact MS bubble until 5,000 yr. Finally, they collide with the dense MS shell and re-brighten again, but gradually lose their punches once more because of the rapid deceleration of the shock into the radiative phase. We conclude that the non-thermal emission from most Type Ib/c SNRs should experience a "resurrection" at some point ($\sim 1,000$ yr for a typical ambient ISM density of $n = 1$ cm^{-3}) for progenitors with ZAMS mass $M_{\rm ZAMS} \leq 18\ M_\odot$. While the exact values of the timescales mentioned

above depend on the (non-)existence of the MS bubble, the ejecta mass, the wind and ISM properties and so on, our conclusion on the predicted general evolution of a Type Ib/c SNR stays robust because it is independent on any fine-tuning of parameters.

We have also compared the results in this work to a previous study on Type II SNRs as reported in YLM21. We show that while Type II SNRs are expected to be bright in the first 1,000 yrs or so but faint afterwards for a few 1,000 yrs in both radio and γ-rays, Type Ib/c SNRs are showing an opposite evolution characteristics, i.e., they are predicted to be dark in the early phase but re-brighten after an age of about 1,000 yr, assuming an $n = 1$ cm^{-3} ISM density. This contrasting behavior leads to an evolutionary picture for the SNR population which is found to be compatible with the γ-ray observation of core-collapse SNRs, in particular the observed broadband spectral properties against the SNR ages, which cannot be reproduced by simplistic models without considering the mass loss histories of the SN progenitors. Another profound implication from our results is that there is a possible observational bias in the current and future SNR observations, i.e., the SN type and progenitor origin of an observed SNR are correlated to its age or evolutionary phase. By the inclusion of other SN subtypes (probably including the different kinds of Ia's as well), and as further observational constraints becoming available in the future, we plan to expand our work to provide a more complete description of the SNR population as a whole.

Chapter 5

Conclusion Remarks

In this dissertation, we have presented serious studies to develop a fuller understanding of the links among SNe, SNRs, and CRs with a numerical simulation and compare the observation data from various detectors. A short summary of the main results, conclusions, and future works of each chapter is described as below:

- In chapter 2, we first developed a numerical model which can compute the non-thermal emissions from various types of SNRs evolved within their circumstellar environment. As the results, we showed that in the Ia models with a uniform ISM, while the π^0-decay flux increases with time, IC flux does not vary much with its spectral peak shifting to lower energy as the SNR ages. In the CC models with a simple power-law CSM, while π^0-decay flux decreases with time, the IC contribution increases with time on the contrary. In the case of an enhanced mass loss from a massive star progenitor, the production of secondary particles are found to be very efficient in the dense confined CSM shell and contribute importantly to the overall SED. For example, they can dominate the synchrotron radiation after the SNR breaks out from the shell into a tenuous wind. We found that the key aspects that dictate these evolutionary trends are the density distribution of the interaction targets for each emission component, and the rate of energy loss of the electrons due to synchrotron radiation by the amplified magnetic field.

  A comparison between our models and observations show a broad agreement. A dramatic enlargement of the sample size of γ-ray emitting SNRs is anticipated in the CTA era to further constrain the parameter space in our systematic survey of SNR broadband models. CTA will have a sufficient sensitivity to detect VHE emission from most Ia and CC SNRs in various environments with a distance within $\sim$ 5.0 kpc. Future observations by CTA will reveal the detailed morphological and

spectral properties of γ-ray emissions from SNRs and make important progress on our understanding of particle acceleration mechanism at astrophysical collisionless shocks.

We note that the current study has only examined several simple models for the ambient environment, which in reality can be much more complicated such as the presence of a cavity, dense shells, clumpy winds and MCs, etc. Our code is designed to be modular which makes it easy for us to expand into a broader parameter space, including more complicated models for the environment. In future work, we will also explore other important physics such as the acceleration of heavier ions, thermal X-ray line emission, radiative shocks and so on.

- In chapter 3, we show that the non-thermal emissions are bright enough to be observed by current and future detectors in the RSG wind phase ($t \leq 1000$ yr), but become very faint beyond detectable in the MS bubble phase (1000 yr $\leq t \leq$ 5000 yr). After the collision with the MS shell ($t \geq$ 5000yr), the SNR re-brightens in radio and γ-rays, but gradually declines in luminosity immediately afterwards due to a rapid deceleration of the shock in the dense cold shell. We conclude that most Type II SNRs experience a “dark age" from 1000 to 5000 yrs for progenitors with ZAMS mass $M_{\rm ZAMS} \leq 18\ M_{\odot}$ exploded in a typical ISM surrounding. This phenomenon is mainly caused by an inefficient particle acceleration and fast adiabatic loss in the thin and hot MS bubble. Our results may help to fill in the gap between the Galactic SN rate and SNR observations. While the existence of a spatially extended MS bubble around massive stars is still uncertain, and is affected by various factors such as the wind properties, the surrounding ISM environment and so on, our conclusion is robust in that it does not depend on any fine-tuning of parameters of aspects such as particle acceleration and explosion properties. A further investigation by expanding our parameter space including different progenitor systems is under way and will be reported in a follow-up work.

- In chapter 4, we show that the non-thermal emissions from Type Ib/c SNRs are faint and below the sensitivities of current and near-future detectors in the early phase when the SNR blastwave is inside the unshoced WR wind region ($t \leq 1,000$ yr), except if the source is extremely close ($d \leq 1$ kpc) and the TeV emission can be potentially picked up by future observatories such as CTA. These objects are also predicted

to be non-thermally bright after the SNR shock has begun to penetrate through the WR wind shell ($t \geq 1,000$ yr). As the SNR shock passes through the dense shell at around 2,000-3,000 yrs, the brightness of SNRs decreases gradually due to the weakening of the shock and fast adiabatic cooling in the hot compact MS bubble until 5,000 yr. Finally, they collide with the dense MS shell and re-brighten again, but gradually lose their punches once more because of the rapid deceleration of the shock into the radiative phase. We conclude that the non-thermal emission from most Type Ib/c SNRs should experience a "resurrection" at some point ($\sim 1,000$ yr for a typical ambient ISM density of $n = 1$ cm^{-3}) for progenitors with ZAMS mass $M_{\rm ZAMS} \leq 18\ M_{\odot}$.

We have also compared the results in this work to a previous study on Type II SNRs as reported in YLM21. We show that while Type II SNRs are expected to be bright in the first 1,000 yrs or so but faint afterwards for a few 1,000 yrs in both radio and γ-rays, Type Ib/c SNRs are showing an opposite evolution characteristics, i.e., they are predicted to be dark in the early phase but re-brighten after an age of about 1,000 yr, assuming an $n = 1$ cm^{-3} ISM density. This contrasting behavior leads to an evolutionary picture for the SNR population which is found to be compatible with the γ-ray observation of core-collapse SNRs, in particular the observed broadband spectral properties against the SNR ages, which cannot be reproduced by simplistic models without considering the mass loss histories of the SN progenitors. Another profound implication from our results is that there is a possible observational bias in the current and future SNR observations, i.e., the SN type and progenitor origin of an observed SNR are correlated to its age or evolutionary phase. By the inclusion of other SN subtypes (probably including the different kinds of Ia's as well), and as further observational constraints becoming available in the future, we plan to expand our work to provide a more complete description of the SNR population as a whole.

Appendix A

Additional models for Type Ib/c SNRs

As mentioned in Section 4.2.2, we have included two additional models here for reference: (i) a model in which all the matters stripped off by RLOF is accreted onto the secondary star (i.e., $\beta_{\rm acc} = 1$; hereafter model E), and (ii) a model in which a massive star with $M_{\rm ZAMS} = 30\ M_\odot$ evolves as a single star without binary interactions (hereafter model F). Figure A.1 shows the CSM density profiles for the two models, and the model parameters are summarized in Table A.1. Figure A.2 plots the time evolution of their non-thermal radio and γ-ray luminosities. The red and blue solid lines correspond to models E and F respectively, and we also over-plot the results of the fiducial model B as a comparison.

TABLE A.1: The wind parameters and ejecta properties of two additional models. Other details are as written in the footnote of Table 4.1.

Model	$M_{\rm ZAMS}$ $[M_\odot]$	Phase	$\dot{M}$ $[M_\odot\ {\rm yr}^{-1}]$	$V_{\rm w}$ [km s^{-1}]	$M_{\rm w}$ $[M_\odot]$	$\tau_{\rm w}$ yr	$M_{\rm ej}$ $[M_\odot]$
E	18	MS	6.0×10^{-7}	2000	0.3	5.0×10^6	
		RLOF	0.0	10	0.0	1.0×10^4	
		WR	1.0×10^{-5}	2000	1.0	1.0×10^5	2.5
F	30	MS	5.0×10^{-7}	2000	2.0	4.0×10^6	
		RSG	5.0×10^{-5}	10	18.0	3.6×10^5	
		WR	5.0×10^{-5}	2000	5.0	1.0×10^5	3.5

A.1 Model E

From Figure A.1, we can see that there are two major differences between models E and B. One is that the density in the WR shell is smaller by more than two orders of magnitude in model E; the other is that the termination

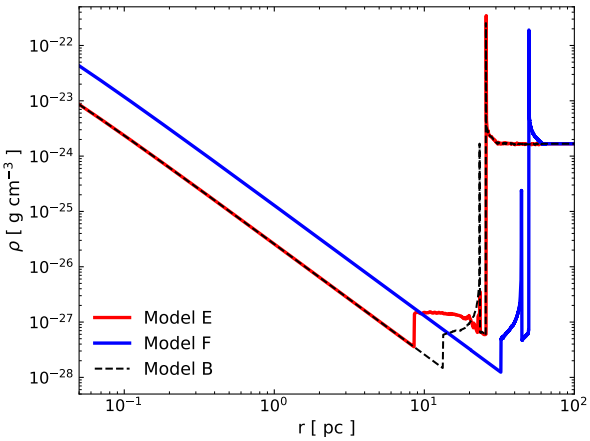

FIGURE A.1: Radial density profiles of the CSM for the two additional models. The red solid line corresponds to model E ($\beta_{\rm acc} = 1$), and the blue solid line to model F ($M_{\rm ZAMS} = 30\ M_{\odot}$). The black dashed line shows the result of model B for comparison.

shock is sitting at a more inner region in the WR wind. These are caused by their differences in the CSM formation history. As the matters stripped off from the progenitor by RLOF in model E are all accreting onto the secondary star without contributing to the CSM gas distribution, the mass swept by the subsequent WR wind is much smaller than in model B, and the WR shell contains a much smaller mass. This also leads to a faster expansion of the WR wind towards the outlying ISM, resulting into the termination shock propagating further inward against the outgoing unshocked WR wind in the last 10^5 yrs.

These differences in the CSM structure are directly reflected in the light curves shown in Figure A.2. In model E, the SNR shock collides with the termination shock at an earlier time, and the luminosities in both energy bands start to rise from $\sim$ 600 yr. The luminosities reach their maximum values at $\sim 2,000$ yr, but are smaller than in model B because the mass inside the WR shell is much smaller. This implies that if $\beta_{\rm acc} \simeq 1$, it becomes more difficult to detect Type Ib/c SNRs, especially in γ-rays.

A.2 Model F

One of the distinctive features of model F is a higher mass-loss rate in each wind phase as shown in Table A.1, which is reflected by the higher density in the wind in Figure A.1. Another difference is that the main mass-stripping mechanism is not via binary interaction but the RSG wind. Nevertheless, the

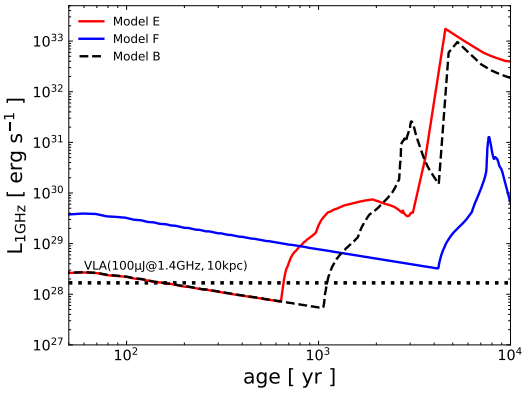

(a)

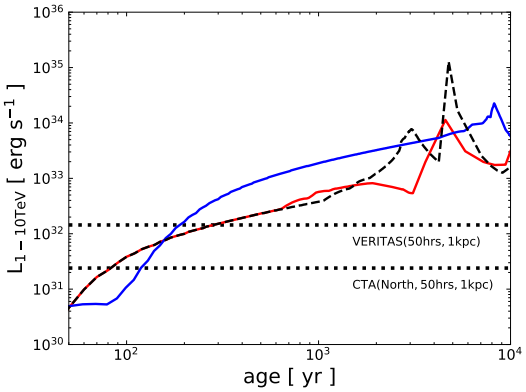

(b)

FIGURE A.2: Light curves in 1 GHz radio continuum (upper panel (a)) and 1-10 TeV band (lower panel (b)) for the additional models. The line formats are the same as in Figure A.1, and the detection limits as shown in Figure 4.3 are also shown.

CSM structure of models B and F are found to be qualitatively similar to each other except that it is more spread out in radius for model F. As explained in Section 4.2.2, the high-velocity wind from the WR star sweeps the RSG wind up quickly, forming a similar CSM structure as that in model B. The WR wind in model F has a high ram pressure from the higher mass-loss rate, therefore the wind shell is formed at a more outer region.

From Figure A.2, we find that this type of SNRs expand into the high density wind region for about 4,000 yrs, and they are brighter in both radio and γ-rays than SNRs with a lower mass progenitor in binaries for the first 1,000 yrs or so. They however becomes relatively faint in radio afterwards during 1,000-4,000 yr due to the fact that the SNR shock is still interacting with the unshocked power-law WR wind, while in model B it has already

collided with the dense WR shell. From this point on, the light curves exhibit a similar behavior as model B. This result suggests that a detection of bright non-thermal emission from a very young Type Ib/c SNR (e.g., a couple 100 yrs old) may imply a high-mass single star for the progenitor, but most probably it will be difficult to distinguish between a single star and binary origin solely from the observed non-thermal emission properties because the details in the pre-SN mass loss history are almost washed away in the emergent CSM structure by the fast WR wind prior to explosion.

Bibliography

Abate, C. et al. (Apr. 2013). "Wind Roche-lobe overflow: Application to carbon-enhanced metal-poor stars". In: *A&A* 552, A26, A26. DOI: 10.1051/0004-6361/201220007. arXiv: 1302.4441 [astro-ph.SR].

Abdo, A. A. et al. (Feb. 2010). "Fermi-Lat Discovery of GeV Gamma-Ray Emission from the Young Supernova Remnant Cassiopeia A". In: *ApJL* 710, pp. L92–L97. DOI: 10.1088/2041-8205/710/1/L92. arXiv: 1001.1419 [astro-ph.HE].

Abdo, A. A. et al. (June 2011). "Observations of the Young Supernova Remnant RX J1713.7-3946 with the Fermi Large Area Telescope". In: *ApJ* 734, 28, p. 28. DOI: 10.1088/0004-637X/734/1/28. arXiv: 1103.5727 [astro-ph.HE].

Abdollahi, S. et al. (Mar. 2020). "Fermi Large Area Telescope Fourth Source Catalog". In: *ApJS* 247.1, 33, p. 33. DOI: 10.3847/1538-4365/ab6bcb. arXiv: 1902.10045 [astro-ph.HE].

Abeysekara, A. U. et al. (May 2020). "Evidence for Proton Acceleration up to TeV Energies Based on VERITAS and Fermi-LAT Observations of the Cas A SNR". In: *ApJ* 894.1, 51, p. 51. DOI: 10.3847/1538-4357/ab8310. arXiv: 2003.13615 [astro-ph.HE].

Acciari, V. A. et al. (June 2009). "Observation of Extended Very High Energy Emission from the Supernova Remnant IC 443 with VERITAS". In: *ApJL* 698, pp. L133–L137. DOI: 10.1088/0004-637X/698/2/L133. arXiv: 0905.3291 [astro-ph.HE].

Acciari, V. A. et al. (May 2010). "Observations of the Shell-type Supernova Remnant Cassiopeia A at TeV Energies with VERITAS". In: *ApJ* 714, pp. 163–169. DOI: 10.1088/0004-637X/714/1/163. arXiv: 1002.2974 [astro-ph.HE].

Acciari, V. A. et al. (Apr. 2011). "Discovery of TeV Gamma-ray Emission from Tycho's Supernova Remnant". In: *ApJL* 730, L20, p. L20. DOI: 10.1088/2041-8205/730/2/L20. arXiv: 1102.3871 [astro-ph.HE].

Acero, F. et al. (Oct. 2009). "A joint spectro-imaging analysis of the XMM-Newton and HESS observations of the supernova remnant RX J1713.7-3946". In: *A&A* 505, pp. 157–167. DOI: 10.1051/0004-6361/200811556. arXiv: 0906.1073 [astro-ph.HE].

Acero, F. et al. (June 2010). "First detection of VHE γ-rays from SN 1006 by HESS". In: *A&A* 516, A62, A62. DOI: 10.1051/0004-6361/200913916. arXiv: 1004.2124 [astro-ph.HE].

Acero, F. et al. (May 2016). "The First Fermi LAT Supernova Remnant Catalog". In: *ApJS* 224, 8, p. 8. DOI: 10.3847/0067-0049/224/1/8. arXiv: 1511.06778 [astro-ph.HE].

Ackermann, M. et al. (Feb. 2013). "Detection of the Characteristic Pion-Decay Signature in Supernova Remnants". In: *Science* 339, pp. 807–811. DOI: 10.1126/science.1231160. arXiv: 1302.3307 [astro-ph.HE].

Adams, Scott M. et al. (Dec. 2013). "Observing the Next Galactic Supernova". In: *ApJ* 778.2, 164, p. 164. DOI: 10.1088/0004-637X/778/2/164. arXiv: 1306.0559 [astro-ph.HE].

Aguilar, M. et al. (Nov. 2015a). "Precision Measurement of the Helium Flux in Primary Cosmic Rays of Rigidities 1.9 GV to 3 TV with the Alpha Magnetic Spectrometer on the International Space Station". In: *PhRvL* 115.21, 211101, p. 211101. DOI: 10.1103/PhysRevLett.115.211101.

Aguilar, M. et al. (May 2015b). "Precision Measurement of the Proton Flux in Primary Cosmic Rays from Rigidity 1 GV to 1.8 TV with the Alpha Magnetic Spectrometer on the International Space Station". In: *PhRvL* 114.17, 171103, p. 171103. DOI: 10.1103/PhysRevLett.114.171103.

Aguilar, M. et al. (Dec. 2017). "Observation of the Identical Rigidity Dependence of He, C, and O Cosmic Rays at High Rigidities by the Alpha Magnetic Spectrometer on the International Space Station". In: *PhRvL* 119.25, 251101, p. 251101. DOI: 10.1103/PhysRevLett.119.251101.

Aharonian, F. et al. (Mar. 2007). "Primary particle acceleration above 100 TeV in the shell-type supernova remnant <ASTROBJ>RX J1713.7-3946</ASTROBJ> with deep HESS observations". In: *A&A* 464, pp. 235–243. DOI: 10.1051/0004-6361:20066381. eprint: astro-ph/0611813.

Aharonian, F. et al. (Sept. 2008). "HESS upper limits for Kepler's supernova remnant". In: *A&A* 488, pp. 219–223. DOI: 10.1051/0004-6361:200809401. arXiv: 0806.3347.

Aharonian, F. et al. (July 2011). "Primary particle acceleration above 100 TeV in the shell-type supernova remnant RX J1713.7 - 3946 with deep H.E.S.S. observations (Corrigendum)". In: *A&A* 531, C1, p. C1. DOI: 10.1051/0004-6361/20066381e.

Aharonian, F. A., S. R. Kelner, and A. Y. Prosekin (Aug. 2010). "Angular, spectral, and time distributions of highest energy protons and associated secondary gamma rays and neutrinos propagating through extragalactic

magnetic and radiation fields". In: *PhRvD* 82.4, 043002, p. 043002. DOI: 10.1103/PhysRevD.82.043002. arXiv: 1006.1045 [astro-ph.HE].

Ahnen, M. L. et al. (Dec. 2017). "A cut-off in the TeV gamma-ray spectrum of the SNR Cassiopeia A". In: *MNRAS* 472, pp. 2956–2962. DOI: 10.1093/mnras/stx2079. arXiv: 1707.01583 [astro-ph.HE].

Albert, J. et al. (Aug. 2007). "Discovery of Very High Energy Gamma Radiation from IC 443 with the MAGIC Telescope". In: *ApJL* 664, pp. L87–L90. DOI: 10.1086/520957. arXiv: 0705.3119.

Allen, G. E., R. Petre, and E. V. Gotthelf (Sept. 2001). "X-Ray Synchrotron Emission from 10-100 TeV Cosmic-Ray Electrons in the Supernova Remnant SN 1006". In: *ApJ* 558, pp. 739–752. DOI: 10.1086/322470. eprint: astro-ph/0107540.

Allen, G. E. et al. (Jan. 2015). "On the Expansion Rate, Age, and Distance of the Supernova Remnant G266.2-1.2 (Vela Jr.)" In: *ApJ* 798, 82, p. 82. DOI: 10.1088/0004-637X/798/2/82. arXiv: 1410.7435 [astro-ph.HE].

Amato, E. and P. Blasi (Feb. 2009). "A kinetic approach to cosmic-ray-induced streaming instability at supernova shocks". In: *MNRAS* 392.4, pp. 1591–1600. DOI: 10.1111/j.1365-2966.2008.14200.x. arXiv: 0806.1223 [astro-ph].

Ambrocio-Cruz, P. et al. (Nov. 2017). "Kinematic study at the H α line in the north-eastern region of the Galactic supernova remnant IC 443". In: *MNRAS* 472, pp. 51–54. DOI: 10.1093/mnras/stx1936.

Archambault, S. et al. (Feb. 2017). "Gamma-Ray Observations of Tycho's Supernova Remnant with VERITAS and Fermi". In: *ApJ* 836, 23, p. 23. DOI: 10.3847/1538-4357/836/1/23. arXiv: 1701.06740 [astro-ph.HE].

Artyukh, V. S., V. V. Vitkevich, and R. D. Dagkesamanskii (1967). "Radio-Source Spectra at Meter Wavelengths." In: *AZh* 44, p. 984.

Baade, W. and F. Zwicky (May 1934). "Cosmic Rays from Super-novae". In: *Proceedings of the National Academy of Science* 20, pp. 259–263. DOI: 10.1073/pnas.20.5.259.

Ballet, J. et al. (May 2020). "Fermi Large Area Telescope Fourth Source Catalog Data Release 2". In: *arXiv e-prints*, arXiv:2005.11208, arXiv:2005.11208. arXiv: 2005.11208 [astro-ph.HE].

Bamba, A. et al. (Jan. 2008). "Suzaku Wide-Band Observations of SN1006". In: *PASJ* 60, S153–S162. DOI: 10.1093/pasj/60.sp1.S153. arXiv: 0708.0073.

Baring, M. G. et al. (Mar. 1999). "Radio to Gamma-Ray Emission from Shell-Type Supernova Remnants: Predictions from Nonlinear Shock Acceleration Models". In: *ApJ* 513, pp. 311–338. DOI: 10.1086/306829. eprint: astro-ph/9810158.

Bell, A. R. (Jan. 1978a). "The acceleration of cosmic rays in shock fronts. I". In: *MNRAS* 182, pp. 147–156. DOI: 10.1093/mnras/182.2.147.

— (Feb. 1978b). "The acceleration of cosmic rays in shock fronts. II". In: *MNRAS* 182, pp. 443–455. DOI: 10.1093/mnras/182.3.443.

— (Sept. 2004). "Turbulent amplification of magnetic field and diffusive shock acceleration of cosmic rays". In: *MNRAS* 353, pp. 550–558. DOI: 10.1111/j.1365-2966.2004.08097.x.

Biermann, Peter L. et al. (Dec. 2010). "The Origin of Cosmic Rays: Explosions of Massive Stars with Magnetic Winds and Their Supernova Mechanism". In: *ApJ* 725.1, pp. 184–187. DOI: 10.1088/0004-637X/725/1/184. arXiv: 1009.5592 [astro-ph.HE].

Blandford, R. D. and J. P. Ostriker (Apr. 1978). "Particle acceleration by astrophysical shocks". In: *ApJL* 221, pp. L29–L32. DOI: 10.1086/182658.

Blasi, P. (Apr. 2004). "Nonlinear shock acceleration in the presence of seed particles". In: *Astroparticle Physics* 21, pp. 45–57. DOI: 10.1016/j.astropartphys.2003.10.008. eprint: astro-ph/0310507.

Blasi, P., S. Gabici, and G. Vannoni (Aug. 2005). "On the role of injection in kinetic approaches to non-linear particle acceleration at non-relativistic shock waves". In: *MNRAS* 361, pp. 907–918. DOI: 10.1111/j.1365-2966.2005.09227.x. eprint: astro-ph/0505351.

Blondin, J. M. and D. C. Ellison (Oct. 2001). "Rayleigh-Taylor Instabilities in Young Supernova Remnants Undergoing Efficient Particle Acceleration". In: *ApJ* 560, pp. 244–253. DOI: 10.1086/322499. eprint: astro-ph/0104024.

Blumenthal, George R. and Robert J. Gould (Jan. 1970). "Bremsstrahlung, Synchrotron Radiation, and Compton Scattering of High-Energy Electrons Traversing Dilute Gases". In: *Reviews of Modern Physics* 42.2, pp. 237–271. DOI: 10.1103/RevModPhys.42.237.

Borkowski, Kazimierz et al. (Aug. 1996). "A Circumstellar Shell Model for the Cassiopeia A Supernova Remnant". In: *ApJ* 466, p. 866. DOI: 10.1086/177560.

Caprioli, D., E. Amato, and P. Blasi (June 2010). "Non-linear diffusive shock acceleration with free-escape boundary". In: *Astroparticle Physics* 33, pp. 307–311. DOI: 10.1016/j.astropartphys.2010.03.001. arXiv: 0912.2714 [astro-ph.HE].

Caprioli, D., P. Blasi, and E. Amato (July 2009). "On the escape of particles from cosmic ray modified shocks". In: *MNRAS* 396, pp. 2065–2073. DOI: 10.1111/j.1365-2966.2008.14298.x. arXiv: 0807.4259.

Caprioli, D. et al. (May 2009). "Dynamical feedback of self-generated magnetic fields in cosmic ray modified shocks". In: *MNRAS* 395, pp. 895–906. arXiv: 0807.4261.

Caprioli, D. et al. (Sept. 2010). "Comparison of different methods for non-linear diffusive shock acceleration". In: *MNRAS* 407, pp. 1773–1783. DOI: 10.1111/j.1365-2966.2010.17013.x. arXiv: 1005.2127 [astro-ph.HE].

Carlton, A. K. et al. (Aug. 2011). "Expansion of the Youngest Galactic Supernova Remnant G1.9+0.3". In: *ApJL* 737, L22, p. L22. DOI: 10.1088/2041-8205/737/1/L22. arXiv: 1106.4498.

Case, Gary L. and Dipen Bhattacharya (Sept. 1998). "A New Σ-D Relation and Its Application to the Galactic Supernova Remnant Distribution". In: *ApJ* 504.2, pp. 761–772. DOI: 10.1086/306089. arXiv: astro-ph/9807162 [astro-ph].

Castelletti, G. et al. (Aug. 2007). "The low-frequency radio emission and spectrum of the extended SNR <ASTROBJ>W44</ASTROBJ>: new VLA observations at 74 and 324 MHz". In: *A&A* 471, pp. 537–549. DOI: 10.1051/0004-6361:20077062. eprint: astro-ph/0702746.

Castelletti, G. et al. (Oct. 2011). "High-resolution radio study of SNR IC 443 at low radio frequencies". In: *A&A* 534, A21, A21. DOI: 10.1051/0004-6361/201016081. arXiv: 1104.0205.

Cherenkov Telescope Array Consortium et al. (2019). *Science with the Cherenkov Telescope Array*. DOI: 10.1142/10986.

Chevalier, R. A. (Aug. 1982a). "Are young supernova remnants interacting with circumstellar gas". In: *ApJL* 259, pp. L85–L89. DOI: 10.1086/183853.

— (July 1982b). "Self-similar solutions for the interaction of stellar ejecta with an external medium". In: *ApJ* 258, pp. 790–797. DOI: 10.1086/160126.

— (Sept. 1983). "Blast waves with cosmic-ray pressure". In: *ApJ* 272, pp. 765–772. DOI: 10.1086/161338.

Chevalier, Roger A. and Claes Fransson (Nov. 2006). "Circumstellar Emission from Type Ib and Ic Supernovae". In: *ApJ* 651.1, pp. 381–391. DOI: 10.1086/507606. arXiv: astro-ph/0607196 [astro-ph].

Clark, D. H. and J. L. Caswell (Feb. 1976). "A study of galactic supernova remnants, based on Molonglo-Parkes observational data." In: *MNRAS* 174, pp. 267–305. DOI: 10.1093/mnras/174.2.267.

Condon, B. et al. (Dec. 2017). "Detection of Two TeV Shell-type Remnants at GeV Energies with FERMI LAT: HESS J1731-347 and SN 1006". In: *ApJ* 851, 100, p. 100. DOI: 10.3847/1538-4357/aa9be8. arXiv: 1711.05499 [astro-ph.HE].

DeLaney, T. and L. Rudnick (June 2003). "The First Measurement of Cassiopeia A's Forward Shock Expansion Rate". In: *ApJ* 589, pp. 818–826. DOI: 10.1086/374813. eprint: astro-ph/0303399.

Devin, J. et al. (Nov. 2020). "High-energy gamma-ray study of the dynamically young SNR G150.3+4.5". In: *A&A* 643, A28, A28. DOI: 10.1051/0004-6361/202038503. arXiv: 2009.08397 [astro-ph.HE].

Drury, L. (Sept. 1983). "On particle acceleration in supernova remnants". In: *SSRv* 36, pp. 57–60. DOI: 10.1007/BF00171901.

Duncan, A. R. and D. A. Green (Dec. 2000). "The supernova remnant RX J0852.0-4622: radio characteristics and implications for SNR statistics". In: *A&A* 364, pp. 732–740. eprint: astro-ph/0009289.

Dwarkadas, V. V. and R. A. Chevalier (Apr. 1998). "Interaction of Type IA Supernovae with Their Surroundings". In: *ApJ* 497, pp. 807–823. DOI: 10.1086/305478.

Elias, J. H. et al. (Sept. 1985). "Type I supernovae in the infrared and their use as distance indicators." In: *ApJ* 296, pp. 379–389. DOI: 10.1086/163456.

Ellison, D. C. et al. (Jan. 2012). "Core-collapse Model of Broadband Emission from SNR RX J1713.7-3946 with Thermal X-Rays and Gamma Rays from Escaping Cosmic Rays". In: *ApJ* 744, 39, p. 39. DOI: 10.1088/0004-637X/744/1/39. arXiv: 1109.0874 [astro-ph.HE].

Ertl, T. et al. (Feb. 2020). "The Explosion of Helium Stars Evolved with Mass Loss". In: *ApJ* 890.1, 51, p. 51. DOI: 10.3847/1538-4357/ab6458. arXiv: 1910.01641 [astro-ph.HE].

Fang, J. and L. Zhang (Mar. 2008). "Non-thermal emission from old supernova remnants". In: *MNRAS* 384, pp. 1119–1128. DOI: 10.1111/j.1365-2966.2007.12766.x. arXiv: 0711.4173.

Fermi, E. (Apr. 1949). "On the Origin of the Cosmic Radiation". In: *Physical Review* 75, pp. 1169–1174. DOI: 10.1103/PhysRev.75.1169.

Ferrand, G. and S. Safi-Harb (May 2012). "A census of high-energy observations of Galactic supernova remnants". In: *Advances in Space Research* 49, pp. 1313–1319. DOI: 10.1016/j.asr.2012.02.004. arXiv: 1202.0245 [astro-ph.HE].

Filippenko, Alexei V. (Jan. 1997). "Optical Spectra of Supernovae". In: *ARA&A* 35, pp. 309–355. DOI: 10.1146/annurev.astro.35.1.309.

Fukui, Y. et al. (Feb. 2012). "A Detailed Study of the Molecular and Atomic Gas toward the γ-Ray Supernova Remnant RX J1713.7-3946: Spatial TeV γ-Ray and Interstellar Medium Gas Correspondence". In: *ApJ* 746, 82, p. 82. DOI: 10.1088/0004-637X/746/1/82. arXiv: 1107.0508.

Gaensler, B. M. and B. J. Wallace (Sept. 2003). "A Multifrequency Radio Study of Supernova Remnant G292.0+1.8 and Its Pulsar Wind Nebula". In: *ApJ* 594, pp. 326–339. DOI: 10.1086/376861. eprint: astro-ph/0305168.

Gaggero, D. et al. (Apr. 2018). "Time evolution of gamma rays from supernova remnants". In: *MNRAS* 475, pp. 5237–5245. DOI: 10.1093/mnras/sty140. arXiv: 1710.05038 [astro-ph.HE].

Ginzburg, V. L. and S. I. Syrovatskii (1964). *The Origin of Cosmic Rays*.

Giordano, F. et al. (Jan. 2012). "Fermi Large Area Telescope Detection of the Young Supernova Remnant Tycho". In: *ApJL* 744, L2, p. L2. DOI: 10.1088/2041-8205/744/1/L2. arXiv: 1108.0265 [astro-ph.HE].

Giuliani, A. et al. (Dec. 2011). "Neutral Pion Emission from Accelerated Protons in the Supernova Remnant W44". In: *ApJL* 742, L30, p. L30. DOI: 10.1088/2041-8205/742/2/L30. arXiv: 1111.4868 [astro-ph.HE].

Gök, F. and A. Sezer (Jan. 2012). "Ejecta detection in the middle-aged Galactic supernova remnant G296.1-0.5 observed with Suzaku". In: *MNRAS* 419, pp. 1603–1609. DOI: 10.1111/j.1365-2966.2011.19822.x. arXiv: 1109.3971 [astro-ph.HE].

Gonzalez, M. and S. Safi-Harb (Feb. 2003). "New Constraints on the Energetics, Progenitor Mass, and Age of the Supernova Remnant G292.0+1.8 Containing PSR J1124-5916". In: *ApJL* 583, pp. L91–L94. DOI: 10.1086/368122. eprint: astro-ph/0301193.

Green, D. A. (June 2017). "VizieR Online Data Catalog: A Catalogue of Galactic Supernova Remnants (Green 2017)". In: *VizieR Online Data Catalog*, VII/278, pp. VII/278.

Gvaramadze, V. V. et al. (Apr. 2017). "IRAS 18153-1651: an H II region with a possible wind bubble blown by a young main-sequence B star". In: *MNRAS* 466.2, pp. 1857–1867. DOI: 10.1093/mnras/stw3257. arXiv: 1612.03916 [astro-ph.SR].

H. E. S. S. Collaboration et al. (Feb. 2015). "H.E.S.S. reveals a lack of TeV emission from the supernova remnant Puppis A". In: *A&A* 575, A81, A81. DOI: 10.1051/0004-6361/201424805. arXiv: 1412.6997 [astro-ph.HE].

H. E. S. S. Collaboration et al. (Apr. 2018). "H.E.S.S. observations of RX J1713.7-3946 with improved angular and spectral resolution: Evidence for gamma-ray emission extending beyond the X-ray emitting shell". In: *A&A* 612, A6, A6. DOI: 10.1051/0004-6361/201629790. arXiv: 1609.08671 [astro-ph.HE].

H. E. S. S. Collaboration et al. (Apr. 2018). "Population study of Galactic supernova remnants at very high γ-ray energies with H.E.S.S." In: *A&A* 612, A3, A3. DOI: 10.1051/0004-6361/201732125. arXiv: 1802.05172 [astro-ph.HE].

Haug, E. (Sept. 1975). "Bremsstrahlung and pair production in the field of free electrons." In: *Zeitschrift Naturforschung Teil A* 30, pp. 1099–1113. DOI: 10.1515/zna-1975-0901.

Helder, E. A. et al. (Oct. 2013). "Proper motions of Hα filaments in the supernova remnant RCW 86". In: *MNRAS* 435, pp. 910–916. DOI: 10.1093/mnras/stt993. arXiv: 1306.3994 [astro-ph.HE].

H.E.S.S. Collaboration et al. (June 2014). "TeV γ-ray observations of the young synchrotron-dominated SNRs G1.9+0.3 and G330.2+1.0 with H.E.S.S." In: *MNRAS* 441, pp. 790–799. DOI: 10.1093/mnras/stu459. arXiv: 1404.1613 [astro-ph.HE].

H.E.S.S. Collaboration et al. (Apr. 2018a). "Deeper H.E.S.S. observations of Vela Junior (RX J0852.0-4622): Morphology studies and resolved spectroscopy". In: *A&A* 612, A7, A7. DOI: 10.1051/0004-6361/201630002. arXiv: 1611.01863 [astro-ph.HE].

H.E.S.S. Collaboration et al. (Apr. 2018b). "Detailed spectral and morphological analysis of the shell type supernova remnant RCW 86". In: *A&A* 612, A4, A4. DOI: 10.1051/0004-6361/201526545. arXiv: 1601.04461 [astro-ph.HE].

Hewitt, J. W. et al. (Nov. 2012). "Fermi-LAT and WMAP Observations of the Puppis A Supernova Remnant". In: *ApJ* 759, 89, p. 89. DOI: 10.1088/0004-637X/759/2/89.

Hui, C. Y. and W. Becker (Feb. 2009). "Exploring the X-ray emission properties of the supernova remnant G67.7+1.8 and its central X-ray sources". In: *A&A* 494, pp. 1005–1012. DOI: 10.1051/0004-6361:200810789. arXiv: 0812.2186.

Iłkiewicz, Krystian et al. (June 2019). "Wind Roche lobe overflow as a way to make Type Ia supernovae from the widest symbiotic systems". In: *MNRAS* 485.4, pp. 5468–5473. DOI: 10.1093/mnras/stz760. arXiv: 1812.02602 [astro-ph.SR].

Jones, Frank C. (Mar. 1968). "Calculated Spectrum of Inverse-Compton-Scattered Photons". In: *Physical Review* 167.5, pp. 1159–1169. DOI: 10.1103/PhysRev.167.1159.

Kafexhiu, Ervin et al. (Dec. 2014). "Parametrization of gamma-ray production cross sections for p p interactions in a broad proton energy range from the kinematic threshold to PeV energies". In: *PhRvD* 90.12, 123014, p. 123014. DOI: 10.1103/PhysRevD.90.123014. arXiv: 1406.7369 [astro-ph.HE].

Kamae, T. et al. (Aug. 2006). "Parameterization of γ, $e^{+/-}$, and Neutrino Spectra Produced by p-p Interaction in Astronomical Environments". In: *ApJ* 647, pp. 692–708. DOI: 10.1086/505189. eprint: astro-ph/0605581.

Kasen, Daniel and S. E. Woosley (Oct. 2009). "Type II Supernovae: Model Light Curves and Standard Candle Relationships". In: *ApJ* 703.2, pp. 2205–2216. DOI: 10.1088/0004-637X/703/2/2205. arXiv: 0910.1590 [astro-ph.CO].

Katsuda, S. et al. (Feb. 2010). "X-ray Measured Dynamics of Tycho's Supernova Remnant". In: *ApJ* 709, pp. 1387–1395. DOI: 10.1088/0004-637X/709/2/1387. arXiv: 1001.2484 [astro-ph.HE].

Katsuda, Satoru et al. (Nov. 2015). "Evidence for Thermal X-Ray Line Emission from the Synchrotron-dominated Supernova Remnant RX J1713.7-3946". In: *ApJ* 814.1, 29, p. 29. DOI: 10.1088/0004-637X/814/1/29. arXiv: 1510.04025 [astro-ph.HE].

Keohane, J. W. et al. (Jan. 2007). "A Near-Infrared and X-Ray Study of W49 B: A Wind Cavity Explosion". In: *ApJ* 654, pp. 938–944. DOI: 10.1086/509311. eprint: astro-ph/0609533.

Koch, H. W. and J. W. Motz (Oct. 1959). "Bremsstrahlung Cross-Section Formulas and Related Data". In: *Reviews of Modern Physics* 31.4, pp. 920–955. DOI: 10.1103/RevModPhys.31.920.

Kothes, R. et al. (Oct. 2006). "A catalogue of Galactic supernova remnants from the Canadian Galactic plane survey. I. Flux densities, spectra, and polarization characteristics". In: *A&A* 457, pp. 1081–1093. DOI: 10.1051/0004-6361:20065062.

Koyama, K. et al. (Nov. 1995). "Evidence for shock acceleration of high-energy electrons in the supernova remnant SN1006". In: *Nature* 378.6554, pp. 255–258. DOI: 10.1038/378255a0.

Krause, Oliver et al. (May 2008). "The Cassiopeia A Supernova Was of Type IIb". In: *Science* 320.5880, p. 1195. DOI: 10.1126/science.1155788. arXiv: 0805.4557 [astro-ph].

Lazendic, J. S. et al. (Feb. 2004). "A High-Resolution Study of Nonthermal Radio and X-Ray Emission from Supernova Remnant G347.3-0.5". In: *ApJ* 602, pp. 271–285. DOI: 10.1086/380956. eprint: astro-ph/0310696.

Lee, S.-H., D. C. Ellison, and S. Nagataki (May 2012a). "A Generalized Model of Nonlinear Diffusive Shock Acceleration Coupled to an Evolving Supernova Remnant". In: *ApJ* 750, 156, p. 156. arXiv: 1203.3614 [astro-ph.HE].

Lee, S.-H. et al. (June 2015). "Modeling Bright γ-Ray and Radio Emission at Fast Cloud Shocks". In: *ApJ* 806, 71, p. 71. DOI: 10.1088/0004-637X/806/1/71. arXiv: 1504.05313 [astro-ph.HE].

Lee, Shiu-Hang, Donald C. Ellison, and Shigehiro Nagataki (May 2012b). "A Generalized Model of Nonlinear Diffusive Shock Acceleration Coupled to an Evolving Supernova Remnant". In: *ApJ* 750.2, 156, p. 156. DOI: 10.1088/0004-637X/750/2/156. arXiv: 1203.3614 [astro-ph.HE].

Li, Weidong et al. (June 2007). "On the Progenitors of Two Type II-P Supernovae in the Virgo Cluster". In: *ApJ* 661.2, pp. 1013–1024. DOI: 10.1086/516747. arXiv: astro-ph/0701049 [astro-ph].

Lovchinsky, I. et al. (Apr. 2011). "A Chandra Observation of Supernova Remnant G350.1-0.3 and Its Central Compact Object". In: *ApJ* 731, 70, p. 70. DOI: 10.1088/0004-637X/731/1/70. arXiv: 1102.5333 [astro-ph.HE].

Mackey, Jonathan et al. (Jan. 2015). "Wind bubbles within H ii regions around slowly moving stars". In: *A&A* 573, A10, A10. DOI: 10.1051/0004-6361/201424716. arXiv: 1410.0019 [astro-ph.GA].

Maeda, K. et al. (July 2015). "Type IIb Supernova 2013df Entering into an Interaction Phase: A Link between the Progenitor and the Mass Loss". In: *ApJ* 807.1, 35, p. 35. DOI: 10.1088/0004-637X/807/1/35. arXiv: 1504.06668 [astro-ph.SR].

Maeda, Y. et al. (Dec. 2009). "Suzaku X-Ray Imaging and Spectroscopy of Cassiopeia A". In: *PASJ* 61, pp. 1217–1228. DOI: 10.1093/pasj/61.6.1217. arXiv: 0912.5020 [astro-ph.HE].

Matsumoto, Yosuke et al. (Sept. 2017). "Electron Surfing and Drift Accelerations in a Weibel-Dominated High-Mach-Number Shock". In: *Phys. Rev. Lett.* 119 (10), p. 105101. DOI: 10.1103/PhysRevLett.119.105101. URL: https://link.aps.org/doi/10.1103/PhysRevLett.119.105101.

Matzner, Christopher D. and Christopher F. McKee (Jan. 1999). "The Expulsion of Stellar Envelopes in Core-Collapse Supernovae". In: *ApJ* 510.1, pp. 379–403. DOI: 10.1086/306571. arXiv: astro-ph/9807046 [astro-ph].

Mohamed, S., J. Mackey, and N. Langer (May 2012). "3D simulations of Betelgeuse's bow shock". In: *A&A* 541, A1, A1. DOI: 10.1051/0004-6361/201118002. arXiv: 1109.1555 [astro-ph.SR].

Mohamed, S. and Ph. Podsiadlowski (Jan. 2012). "Mass Transfer in Mira-type Binaries". In: *Baltic Astronomy* 21, pp. 88–96. DOI: 10.1515/astro-2017-0362.

Nicholl, M. et al. (Oct. 2015). "On the diversity of superluminous supernovae: ejected mass as the dominant factor". In: *MNRAS* 452, pp. 3869–3893. DOI: 10.1093/mnras/stv1522. arXiv: 1503.03310 [astro-ph.SR].

Nikolić, S. et al. (Apr. 2013). "An Integral View of Fast Shocks Around Supernova 1006". In: *Science* 340, pp. 45–48. DOI: 10.1126/science.1228297. arXiv: 1302.4328 [astro-ph.HE].

Ohira, Yutaka and Kunihito Ioka (Mar. 2011). "Cosmic-ray Helium Hardening". In: *ApJL* 729.1, L13, p. L13. DOI: 10.1088/2041-8205/729/1/L13.

Ouchi, Ryoma and Keiichi Maeda (May 2017). "Radii and Mass-loss Rates of Type IIb Supernova Progenitors". In: *ApJ* 840.2, 90, p. 90. DOI: 10.3847/1538-4357/aa6ea9. arXiv: 1705.02430 [astro-ph.HE].

Planck Collaboration et al. (Feb. 2016). "Planck intermediate results. XXXI. Microwave survey of Galactic supernova remnants". In: *A&A* 586, A134, A134. DOI: 10.1051/0004-6361/201425022. arXiv: 1409.5746.

Poveda, A. and L. Woltjer (Mar. 1968). "Supernovae and Supernova Remnants". In: *AJ* 73, p. 65. DOI: 10.1086/110600.

Prinz, T. and W. Becker (Aug. 2012). "Exploring the supernova remnant G308.4-1.4". In: *A&A* 544, A7, A7. DOI: 10.1051/0004-6361/201219086. arXiv: 1202.4677 [astro-ph.HE].

Ptuskin, Vladimir, Vladimir Zirakashvili, and Eun-Suk Seo (July 2010). "Spectrum of Galactic Cosmic Rays Accelerated in Supernova Remnants". In: *ApJ* 718.1, pp. 31–36. DOI: 10.1088/0004-637X/718/1/31. arXiv: 1006.0034 [astro-ph.CO].

Rakowski, C. E., J. P. Hughes, and P. Slane (Feb. 2001). "Two New Ejecta-dominated Galactic Supernova Remnants: G337.2-0.7 and G309.2-0.6". In: *ApJ* 548, pp. 258–268. DOI: 10.1086/318680. eprint: astro-ph/0010091.

Reynolds, M. T. et al. (Apr. 2013). "G306.3-0.9: A Newly Discovered Young Galactic Supernova Remnant". In: *ApJ* 766, 112, p. 112. DOI: 10.1088/0004-637X/766/2/112. arXiv: 1303.3546 [astro-ph.HE].

Reynoso, E. M., S. Cichowolski, and A. J. Walsh (Jan. 2017). "A high-resolution H I study towards the supernova remnant Puppis A and its environments". In: *MNRAS* 464, pp. 3029–3039. DOI: 10.1093/mnras/stw2219. arXiv: 1609.01779.

Roger, R. S. et al. (Apr. 1986). "G291.0-0.1, a centrally bright supernova remnant, in Carina". In: *MNRAS* 219, pp. 815–822. DOI: 10.1093/mnras/219.4.815.

Rybicki, George B. and Alan P. Lightman (1986). *Radiative Processes in Astrophysics*.

Sánchez-Ayaso, E. et al. (Apr. 2013). "XMM-Newton and Chandra observations of G272.2-3.2. Evidence of stellar ejecta in the central region". In: *A&A* 552, A52, A52. DOI: 10.1051/0004-6361/201219709. arXiv: 1301.1507 [astro-ph.HE].

Sasaki, M. et al. (Sept. 2018). "Infrared and X-ray study of the Galactic SNR G15.9+0.2". In: *MNRAS* 479, pp. 3033–3041. DOI: 10.1093/mnras/sty1596. arXiv: 1806.11365 [astro-ph.HE].

Schinnerer, E. et al. (Nov. 2004). "The VLA-COSMOS Survey. I. Radio Identifications from the Pilot Project". In: *AJ* 128.5, pp. 1974–1989. DOI: 10.1086/424860. arXiv: astro-ph/0408149 [astro-ph].

Sedov, L. I. (1959). *Similarity and Dimensional Methods in Mechanics*.

Sezer, A., T. Ergin, and R. Yamazaki (Apr. 2017). "Suzaku analysis of the supernova remnant G306.3-0.9 and the gamma-ray view of its neighbourhood". In: *MNRAS* 466, pp. 3434–3441. DOI: 10.1093/mnras/stw3331. arXiv: 1701.00102 [astro-ph.HE].

Simpson, Chris et al. (Apr. 2012). "Radio imaging of the Subaru/XMM-Newton Deep Field- III. Evolution of the radio luminosity function beyond z= 1". In: *MNRAS* 421.4, pp. 3060–3083. DOI: 10.1111/j.1365-2966.2012.20529.x. arXiv: 1201.3225 [astro-ph.CO].

Sinitsina, V. G. and V. Y. Sinitsina (June 2015). "Results of observations of shell supernova remnants at ultrahigh energies with the SHALON mirror Cherenkov telescopes". In: *Bulletin of the Lebedev Physics Institute* 42, pp. 169–175. DOI: 10.3103/S1068335615060032. arXiv: 1602.01694 [astro-ph.HE].

Slane, P. et al. (Mar. 2014). "A CR-hydro-NEI Model of the Structure and Broadband Emission from Tycho's Supernova Remnant". In: *ApJ* 783, 33, p. 33. DOI: 10.1088/0004-637X/783/1/33. arXiv: 1401.2556 [astro-ph.HE].

Smartt, S. J. (Apr. 2015). "Observational Constraints on the Progenitors of Core-Collapse Supernovae: The Case for Missing High-Mass Stars". In:

PASA 32, e016, e016. DOI: 10.1017/pasa.2015.17. arXiv: 1504.02635 [astro-ph.SR].

Smith, Nathan (2017). "Interacting Supernovae: Types IIn and Ibn". In: *Handbook of Supernovae*. Ed. by Athem W. Alsabti and Paul Murdin, p. 403. DOI: 10.1007/978-3-319-21846-5_38.

Smith, Nathan et al. (Apr. 2011). "Observed fractions of core-collapse supernova types and initial masses of their single and binary progenitor stars". In: *MNRAS* 412.3, pp. 1522–1538. DOI: 10.1111/j.1365-2966.2011.17229.x. arXiv: 1006.3899 [astro-ph.HE].

Spitzer, Lyman (1965). *Physics of fully ionized gases*.

Sturner, S. J. et al. (Dec. 1997). "Temporal Evolution of Nonthermal Spectra from Supernova Remnants". In: *ApJ* 490, pp. 619–632. DOI: 10.1086/304894.

Sukhbold, Tuguldur and S. E. Woosley (Mar. 2014). "The Compactness of Presupernova Stellar Cores". In: *ApJ* 783.1, 10, p. 10. DOI: 10.1088/0004-637X/783/1/10. arXiv: 1311.6546 [astro-ph.SR].

Sukhbold, Tuguldur et al. (Apr. 2016). "Core-collapse Supernovae from 9 to 120 Solar Masses Based on Neutrino-powered Explosions". In: *ApJ* 821.1, 38, p. 38. DOI: 10.3847/0004-637X/821/1/38. arXiv: 1510.04643 [astro-ph.HE].

Sutherland, Ralph S. and M. A. Dopita (Sept. 1993). "Cooling Functions for Low-Density Astrophysical Plasmas". In: *ApJS* 88, p. 253. DOI: 10.1086/191823.

Suzuki, Hiromasa et al. (Oct. 2020). "Study on the escape timescale of high-energy particles from supernova remnants through thermal X-ray properties". In: *PASJ* 72.5, 72, p. 72. DOI: 10.1093/pasj/psaa061. arXiv: 2006.03382 [astro-ph.HE].

Tanaka, T. et al. (Oct. 2008). "Study of Nonthermal Emission from SNR RX J1713.7-3946 with Suzaku". In: *ApJ* 685, pp. 988–1004. DOI: 10.1086/591020. arXiv: 0806.1490.

Tanaka, T. et al. (Oct. 2011). "Gamma-Ray Observations of the Supernova Remnant RX J0852.0-4622 with the Fermi Large Area Telescope". In: *ApJL* 740, L51, p. L51. DOI: 10.1088/2041-8205/740/2/L51. arXiv: 1109.4658 [astro-ph.HE].

Tanaka, Takaaki et al. (Sept. 2020). "Shock-Cloud Interaction in the Southwestern Rim of RX J1713.7-3946 Evidenced by Chandra X-Ray Observations". In: *ApJL* 900.1, L5, p. L5. DOI: 10.3847/2041-8213/abaef0. arXiv: 2008.05581 [astro-ph.HE].

Tang, Z., S. P. Reynolds, and S. M. Ressler (Dec. 2016). "X-Ray and Gamma-Ray Emission from Middle-aged Supernova Remnants In cavities. I. Spherical Symmetry". In: *ApJS* 227, 28, p. 28. DOI: 10.3847/1538-4365/227/2/28. arXiv: 1701.05615 [astro-ph.HE].

Tauris, Thomas M. and Gerrit J. Savonije (Oct. 1999). "Formation of millisecond pulsars. I. Evolution of low-mass X-ray binaries with P_orb> 2 days". In: *A&A* 350, pp. 928–944. arXiv: astro-ph/9909147 [astro-ph].

Tavani, M. et al. (Feb. 2010). "Direct Evidence for Hadronic Cosmic-Ray Acceleration in the Supernova Remnant IC 443". In: *ApJL* 710, pp. L151–L155. DOI: 10.1088/2041-8205/710/2/L151. arXiv: 1001.5150 [astro-ph.HE].

Townsend, R. H. D. (Apr. 2009). "An Exact Integration Scheme for Radiative Cooling in Hydrodynamical Simulations". In: *ApJS* 181.2, pp. 391–397. DOI: 10.1088/0067-0049/181/2/391. arXiv: 0901.3146 [astro-ph.SR].

Troja, E. et al. (Dec. 2014). "Swift/BAT Detection of Hard X-Rays from Tycho's Supernova Remnant: Evidence for Titanium-44". In: *ApJL* 797, L6, p. L6. DOI: 10.1088/2041-8205/797/1/L6. arXiv: 1411.0991 [astro-ph.HE].

Truelove, J. K. and C. F. McKee (Feb. 1999). "Evolution of Nonradiative Supernova Remnants". In: *ApJS* 120, pp. 299–326. DOI: 10.1086/313176.

Tsuji, N. and Y. Uchiyama (Dec. 2016). "Expansion measurements of supernova remnant RX J1713.7-3946". In: *PASJ* 68, 108, p. 108. DOI: 10.1093/pasj/psw102. arXiv: 1609.07886 [astro-ph.HE].

Uchida, H. et al. (Dec. 2012). "Recombining Plasma and Hard X-Ray Filament in the Mixed-Morphology Supernova Remnant W 44". In: *PASJ* 64, 141, p. 141. DOI: 10.1093/pasj/64.6.141. arXiv: 1208.0113 [astro-ph.HE].

van den Heuvel, E. P. J. (Jan. 2009). "The Formation and Evolution of Relativistic Binaries". In: *Physics of Relativistic Objects in Compact Binaries: From Birth to Coalescence*. Ed. by Monica Colpi et al. Vol. 359. Astrophysics and Space Science Library, p. 125. DOI: 10.1007/978-1-4020-9264-0_4.

Vartanyan, David et al. (July 2021). "Binary-stripped Stars as Core-collapse Supernovae Progenitors". In: *ApJL* 916.1, L5, p. L5. DOI: 10.3847/2041-8213/ac0b42. arXiv: 2104.03317 [astro-ph.SR].

Vink, J. (Dec. 2008). "The Kinematics of Kepler's Supernova Remnant as Revealed by Chandra". In: *ApJ* 689, pp. 231–241. DOI: 10.1086/592375. arXiv: 0803.4011.

Wang, Bo et al. (Sept. 2021). "Ultracompact X-ray binaries with He star companions". In: *MNRAS* 506.3, pp. 4654–4666. DOI: 10.1093/mnras/stab2032. arXiv: 2106.01369 [astro-ph.HE].

Wang, C.-Y. and R. A. Chevalier (Mar. 2001). "Instabilities and Clumping in Type IA Supernova Remnants". In: *ApJ* 549, pp. 1119–1134. DOI: 10.1086/319439. eprint: astro-ph/0005105.

Wang, W. and Z. Li (July 2016). "Hard X-Ray Emissions from Cassiopeia A Observed by INTEGRAL". In: *ApJ* 825, 102, p. 102. DOI: 10.3847/0004-637X/825/2/102. arXiv: 1605.00360 [astro-ph.HE].

Warren, D. C. and J. M. Blondin (Mar. 2013). "Three-dimensional numerical investigations of the morphology of Type Ia SNRs". In: *MNRAS* 429, pp. 3099–3113. DOI: 10.1093/mnras/sts566. arXiv: 1210.7790.

Warren, J. S. et al. (Nov. 2005). "Cosmic-Ray Acceleration at the Forward Shock in Tycho's Supernova Remnant: Evidence from Chandra X-Ray Observations". In: *ApJ* 634, pp. 376–389. DOI: 10.1086/496941. eprint: astro-ph/0507478.

Wheeler, J. Craig and Robert P. Harkness (Jan. 1986). "Physical models of supernovae and the distance scale." In: *Galaxy Distances and Deviations from Universal Expansion*. Ed. by Barry F. Madore and R. Brent Tully. Vol. 180. NATO Advanced Study Institute (ASI) Series C, pp. 45–54.

Williams, B. J. et al. (June 2013). "Azimuthal Density Variations around the Rim of Tycho's Supernova Remnant". In: *ApJ* 770, 129, p. 129. DOI: 10.1088/0004-637X/770/2/129. arXiv: 1305.0567 [astro-ph.HE].

Williams, B. J. et al. (Mar. 2018). "A Deep X-Ray View of the Synchrotron-dominated Supernova Remnant G330.2+1.0". In: *ApJ* 855, 118, p. 118. DOI: 10.3847/1538-4357/aaadb6. arXiv: 1802.02804 [astro-ph.HE].

Woosley, S. E. (June 2019). "The Evolution of Massive Helium Stars, Including Mass Loss". In: *ApJ* 878.1, 49, p. 49. DOI: 10.3847/1538-4357/ab1b41. arXiv: 1901.00215 [astro-ph.SR].

Woosley, S. E. and A. Heger (Apr. 2007). "Nucleosynthesis and remnants in massive stars of solar metallicity". In: *PhR* 442.1-6, pp. 269–283. DOI: 10.1016/j.physrep.2007.02.009. arXiv: astro-ph/0702176 [astro-ph].

Woosley, S. E. and Alexander Heger (Sept. 2015). "The Remarkable Deaths of 9-11 Solar Mass Stars". In: *ApJ* 810.1, 34, p. 34. DOI: 10.1088/0004-637X/810/1/34. arXiv: 1505.06712 [astro-ph.SR].

Woosley, S. E., Tuguldur Sukhbold, and H. T. Janka (June 2020). "The Birth Function for Black Holes and Neutron Stars in Close Binaries". In: *ApJ* 896.1, 56, p. 56. DOI: 10.3847/1538-4357/ab8cc1. arXiv: 2001.10492 [astro-ph.HE].

Woosley, S. E., Tuguldur Sukhbold, and D. N. Kasen (June 2021). "Model Light Curves for Type Ib and Ic Supernovae". In: *ApJ* 913.2, 145, p. 145. DOI: 10.3847/1538-4357/abf3be. arXiv: 2009.06868 [astro-ph.HE].

Xin, Y.-L. et al. (July 2017). "Revisiting SNR Puppis A with Seven Years of Fermi Large Area Telescope Observations". In: *ApJ* 843, 90, p. 90. DOI: 10.3847/1538-4357/aa74bb. arXiv: 1703.03911 [astro-ph.HE].

Yasuda, Haruo and Shiu-Hang Lee (May 2019). "Time Evolution of Broadband Nonthermal Emission from Supernova Remnants in Different Circumstellar Environments". In: *ApJ* 876.1, 27, p. 27. DOI: 10.3847/1538-4357/ab13ab. arXiv: 1903.10226 [astro-ph.HE].

Yasuda, Haruo, Shiu-Hang Lee, and Keiichi Maeda (Oct. 2021). "Dark Age of Type II Supernova Remnants". In: *ApJL* 919.2, L16, p. L16. DOI: 10.3847/2041-8213/ac24ac. arXiv: 2109.04032 [astro-ph.HE].

Yoon, Sung-Chul (Oct. 2017). "Towards a better understanding of the evolution of Wolf-Rayet stars and Type Ib/Ic supernova progenitors". In: *MNRAS* 470.4, pp. 3970–3980. DOI: 10.1093/mnras/stx1496. arXiv: 1706.04716 [astro-ph.SR].

Yuan, Q., S. Liu, and X. Bi (Dec. 2012). "An Attempt at a Unified Model for the Gamma-Ray Emission of Supernova Remnants". In: *ApJ* 761, 133, p. 133. DOI: 10.1088/0004-637X/761/2/133. arXiv: 1203.0085 [astro-ph.HE].

Yuan, Yajie et al. (Dec. 2013). "Fermi Large Area Telescope Detection of a Break in the Gamma-Ray Spectrum of the Supernova Remnant Cassiopeia A". In: *ApJ* 779.2, 117, p. 117. DOI: 10.1088/0004-637X/779/2/117. arXiv: 1310.8287 [astro-ph.HE].

Zhu, H., W. W. Tian, and P. Zuo (Oct. 2014). "Supernova Remnant W49B and Its Environment". In: *ApJ* 793, 95, p. 95. DOI: 10.1088/0004-637X/793/2/95. arXiv: 1407.8260 [astro-ph.SR].

Zirakashvili, V. N. and V. S. Ptuskin (Dec. 2012). "Numerical simulations of diffusive shock acceleration in SNRs". In: *Astroparticle Physics* 39, pp. 12–21. DOI: 10.1016/j.astropartphys.2011.09.003. arXiv: 1109.4482 [astro-ph.HE].

Acknowledgements

I would like to express my gratitude to all who leads me during five years of Ph.D. course in Kyoto university. First of all, I am very grateful to my supervisor, Junior Associate Professor Shiu-Hang Lee (wa call him "Herman"), who took me into the world of SNR and CR acceleration. When I became his student, I do not have any knowledge about an astronomy, not to mention SNR, but he always encourages me and kindly gives me many of advice on the execution of the researches. I feel very lucky to become his first student in Kyoto university. This thesis would not have completed without his constant and awesome coaching.

Second, I would like to express my appreciation to Associate Professor Keiichi Maeda, my collaborator of second and third works. Of course, He give us many useful comments about first paper. He help me with my thesis by his outstanding knowledge about SNe and related fields.

Next, I also appreciate for Professor Shin Mineshige, who first accepted me as his student when entering the master course, although I have never studied the astronomy. Surprisingly, I learned how to use NASA/ADS from him and Kawanaka-san. After I left his lab, he has still cared me and given me the important advice at the key points.

My classmates and seniors are very helpful particularly in terms of knowledge and mentality in the executing the research, and especially, my juniors, Mr. Tomoki Matsuoka and Mr. Ryosuke Kobashi went along with the discussions about my research and the others. I am very grateful to get acquired with them.

Finally, I thank my family (Shigeshi, Masami, and Satomi) who raised me so far and received my selfishness to go on to graduate school. Their existence made me who I am now.

I dedicate this thesis to my mother, Masami, in heaven.

Haruo Yasuda